Methods for Improving MRI-Based Conductivity Mapping

by

Kathleen Marie Panagis

A dissertation submitted in partial fulfillment
of the requirements for the degree of
Doctor of Philosophy
(Biomedical Engineering)
in The University of Michigan
2018

Doctoral Committee:

Professor Douglas C. Noll, Chair
Professor Thomas L. Chenevert
Professor Jeffrey A. Fessler
Associate Research Scientist Jon-Fredrik Nielsen

Kathleen Marie Panagis

kropella@umich.edu

ORCID iD: 0000-0002-6284-5776

ACKNOWLEDGEMENTS

This dissertation is five and a half years in the making, and I could not have done it alone. First and foremost, I need to thank Doug Noll, my research advisor and dissertation chair. Doug has taught me so much about MRI and academia in general, and I am incredibly grateful for his support and direction over the years. Doug is one of the most open-minded and optimistic faculty I have met, and I hope I can emulate those qualities in the future.

Thank you to my other committee members: Tom Chenevert, Jeff Fessler, and Jon-Fredrik Nielsen. You have all provided valuable feedback on my research. Dr. Fessler has also been a great professor, and I've learned so much from taking his courses. Jon is always available to answer questions, offer suggestions, or just listen to ideas.

Thank you to the other faculty in the FMRI lab: Luis Hernandez-Garcia and Scott Peltier. You have also been great teachers and given me valuable feedback over the years. All of the faculty in the FMRI lab have been kind and friendly, and I am so glad I was able to have you all as mentors. A special thanks to Scott for helping me with DTI acquisitions for this dissertation.

Thank you to my lab-mates, including those who have already graduated (Feng, Yash, Hao, Angela, Alan, and Matt), those who are still working towards graduation (Sydney, Tianrui, Michelle, Anish, and Shouchang), and the unofficial lab-mates who spend a lot of time around an MRI scanner (Mai, Gopal, Jonas). You have all taught me something new, helped me run experiments, and given me valuable feedback.

Thank you for making our office an enjoyable place to work. I also sincerely hope the strong female presence in the lab will continue for many years to come.

Thank you to the FMRI lab staff: Keith, Ryan, Ruth, and Barb. They have helped me with experiments and make things run smoothly. I would also like to thank Chuck, Maria, and many other students, faculty, and staff in the BME department for helping me with all aspects of my graduate school life.

Thank you to everyone who has helped me become a better teacher: the folks at CRLT-Engin, the faculty for whom I have served as a GSI, the ASEE student chapter, and of course the students who put up with me. While perhaps you haven't directly influenced in this dissertation, our time together was always a refreshing break from research and course work and fueled my passion for teaching.

Thank you to my friends, near and far, for being supportive and helping me stay sane as a graduate student. A special shout out to my cycling buddies - you don't know how many problems I have solved while out on a bike ride.

Thank you to my family, especially my parents and my brothers, for being incredibly supportive on this journey and for always taking an interest in my work.

Finally, thank you to my husband, Tim. You have always been supportive, encouraging, and incredibly helpful in making sure I have some sort of work-life balance.

Kathleen Panagis (Ropella)

Ann Arbor, MI

November 20, 2017

TABLE OF CONTENTS

LIST OF FIGURES

Figure

LIST OF TABLES

Table

ABSTRACT

The electrical properties - permittivity and conductivity - of a material describe how electromagnetic waves behave in that material. Electrical properties are frequency-dependent parameters and, for a liquid sample, are measured with a dielectric probe and a network analyzer. This measurement technique is not feasible in vivo, but methods have been developed to make these measurements using magnetic resonance imaging (MRI). This work focuses on measuring conductivity, or the ability to conduct electric current. Mapping the electrical properties within the human body can provide important information for MRI safety and diagnostic applications. First, the specific absorption rate (SAR) in an MRI scan is proportional to conductivity, and limited to minimize the risk of heating in a subject. Knowledge of subject-specific conductivity maps could lead to better, subject-specific SAR estimation. Second, several small studies in recent years have shown that conductivity is elevated in malignant tumors as compared to healthy tissue. There are open research questions regarding the correlation between conductivity and other diagnostic metrics. Both of these applications benefit from accurate conductivity maps. In this work we describe three different methods for improving the accuracy of conductivity maps. The first is a novel regularized, model-based approach which we refer to as the Inverse Laplacian method. The Inverse Laplacian method resulted in lower reconstruction bias and error due to noise in simulations than the conventional filtering method. The Inverse Laplacian method also produced conductivity maps closer to the measured values in a phantom and with reduced noise in the human brain, as compared to the filtering method. The second is a method for combining multi-coil MRI data for conductiv-

ity mapping, because the use of multi-coil receivers can drastically improve the SNR in conductivity maps. The noise in the combined phase data using the proposed method was slightly elevated as compared to the optimal combination method, but the conductivity uniformity in a uniform gel phantom was greater than that of the optimal combination method. Furthermore, by visual inspection, the human brain conductivity calculated from data combined using the proposed method had minimal bias and noise amplification. Finally, we present a method for mapping conductivity tensors, as opposed to scalar values, which provides an additional layer of information to conductivity maps. Our proposed mathematical framework yields accurate tensor quantities provided the object can rotate 90 degrees in any direction. However, restricting the object rotation to mimic the constraints on a human subject yields slightly inaccurate results. We also present a dictionary-based approach to tensor calculations to try to improve the tensor estimates using restricted rotations.

CHAPTER I

Introduction

The electrical properties of a material, which include permittivity and conductivity, describe how electromagnetic fields propagate throughout the material. Conductivity describes a material's ability to conduct electric current whereas permittivity describes a material's resistance to establish an electric field. Conductive materials include metals and aqueous salt solutions. Non-conductive materials are also referred to as insulators and include air, glass, and plastics. Permittivity and conductivity are frequency-dependent parameters, so the behavior of conductive and dielectric materials can change with the frequency of the application. The primary focus of this work is on mapping conductivity in vivo, where we essentially encounter different salt water solutions.

1.1 Motivation

Electrical properties of various human tissues have been studied ex vivo for a wide range of frequencies (1–3), and these values are commonly used in electromagnetic modeling applications. In the low-frequency range, conductivity depends on the impedance of cell membranes (4). Low-frequency electrical properties measurement techniques may be advantageous for planning therapeutic procedures, where tissue conductivity affects current density. For example, conductivity maps may be

useful or even necessary for planning transcranial magnetic stimulation (5, 6), with frequency content between 0-10 kHz, or transcranial direct current stimulation (7, 8), with frequency content primarily at 0 Hz.

At higher frequencies, above 100 MHz, the impedance of the membrane is negligible and electrical properties are primarily dependent on water and ion concentration. There has been some work in studying the relationships between water and ions and measured conductivity values (9–12). It is likely that the exact relationship between tissue composition and electrical properties is complex in humans, and therefore may be useful as biomarkers. Electrical properties have been shown to increase in tumors in ex vivo experiments (13–16). Some smaller studies have shown that these electrical property changes - primarily conductivity - can be detected using MR-EPT, so there is potential for MR-EPT to provide an additional layer of information to clinicians when examining tumors. A major area of focus of this application is measuring electrical properties in breast cancer (17–21), including studying correlations between conductivity and malignancy (22–24). The brain is the second major area of focus. Brain cancer studies are similar to those in the breast, where the end goal is to differentiate between tumor grades (11, 25–29). There is also active research in conductivity changes after a stroke (30–32). These findings in the breast and brain also align with sodium imaging MRI studies, which have shown that sodium concentration increases in breast cancer, brain cancer, and stroke (33–35). This supports the idea that conductivity at high frequencies depends on ion concentration, and furthermore suggests using MR-EPT as a surrogate for less-readily available sodium imaging.

Other, less common, areas of study for the diagnostic value of electrical properties include the heart, pelvis, and lung (36–40).

There are numerous open research questions as to how conductivity correlates to other tumor metrics, as well as what additional information conductivity will provide to clinicians. Some studies show that electrical properties may be redundant to

diffusion data (41, 42), but Tha et al. have provided evidence that not all diffusion parameters correlate well with conductivity (43).

High-frequency electrical property mapping is also important for MRI safety applications. One risk to subjects during a MRI exam is tissue heating. As a surrogate for temperature increase, the specific absorption rate (SAR) is closely monitored during exams. SAR is proportional to the conductivity of a tissue, but typically this is not measured and large safety factors are built in. Predicting and monitoring SAR is a key safety factor in parallel transmit and high field MRI applications. Doing so on a subject-specific basis requires accurate, subject-specific conductivity maps. Subject-specific SAR predictions may be beneficial for subjects with atypical conductivity, perhaps due to a lesion or implant. It may also be beneficial in designing MRI pulse sequences because a more precise knowledge of conductivity would give more degrees of freedom in the design process. Examples of preliminary work in predicting SAR using conductivity maps can be found in (44, 45).

The common thread among all of these applications is the need for accurate, high resolution, high signal-to noise ratio (SNR) conductivity maps.

1.2 Methods for Mapping Electrical Properties

There are a number of methods available for estimating the electrical properties in vivo, that can generally be separated into low- and high-frequency domains. Due to the frequency-dependent nature of the electrical properties, the best estimation approach will depend on the frequency range of the application.

The low-frequency domain for measuring electrical properties typically covers DC through the kilohertz range. The oldest method in this category is electrical impedance tomography (EIT). An overview of the subject can be found in the textbook by Holder (46). EIT involves attaching several electrodes to a subject and injecting current into the body. Voltages are measured through electrodes as well,

and the impedance distribution of the subject is reconstructed based on the measurements. EIT is low cost, portable, and uses levels of current that are considered safe. However, the EIT inverse problem is difficult to solve. The number of electrodes can be a limiting factor in spatial resolution, but so is the non-local property of impedance; the impedance in a small region of the body can influence the measurements at all electrodes because measurements are only acquired at the boundary. Due to the inherent coupling of electric and magnetic fields, magnetic resonance imaging (MRI) was determined to be a useful tool to improve the spatial resolution of EIT images. Initially, this combination of techniques used DC current injections and is referred to as magnetic resonance current density imaging (MR-CDI) (47). Further work in coupling MRI with EIT resulted in magnetic resonance electrical impedance tomography (MREIT) (48–51). MREIT makes the EIT problem easier to solve because it measures the spatial distribution of the magnetic field inside the subject in addition to measuring voltages at the boundary. Another low-frequency method is magnetic induction tomography (MIT) (52). MIT does not involve direct contact with the subject. Magnetic fields are applied and measured, but not using an MRI scanner. Spatial resolution in these images is also relatively poor.

The high-frequency domain of electrical property measurement primarily consists of magnetic resonance electrical properties tomography (MR-EPT). This method does not involve direct contact with the subject and it is implemented as a typical MRI exam. The electrical properties of the subject distort the magnetic fields within the scanner, which can be measured using common MRI techniques. Due to the magnetic fields used in MR-EPT, the electrical property maps are calculated at the Larmor frequency of the MRI scanner. The electrical properties calculation is straight-forward because we make measurements and calculate electrical properties at each spatial location, but some of the limitations are discussed below in Section 1.7.

1.3 The Homogeneous Helmholtz Equation

The complex permittivity of a material is defined as $\kappa(x, y, z, \omega) := \epsilon(x, y, z, \omega) - i(\frac{\sigma(x,y,z,\omega)}{\omega})$ where ϵ is permittivity, σ is conductivity, and ω is the angular frequency of interest. The electrical properties are not only a function of spatial location, but also the angular frequency of interest. The complex permittivity of an object is related to the magnetic field, $\mathbf{H}$, by the Helmholtz wave equation (53):

$$-\nabla^2\mathbf{H} = \frac{\nabla\kappa}{\kappa} \times [\nabla \times \mathbf{H}] + \omega^2\mu_0\kappa\mathbf{H} \quad [1.1]$$

where ω is the resonant frequency and μ_0 is the permeability of free space.

Under the assumption that the complex permittivity is spatially constant, the term $\frac{\nabla\kappa}{\kappa} \times [\nabla \times \mathbf{H}] = 0$, leading to the homogeneous Helmholtz equation (54):

$$-\nabla^2\mathbf{H} = \omega^2\mu_0\kappa\mathbf{H}. \quad [1.2]$$

Therefore, one can calculate the complex permittivity of a material from the measured complex-valued magnetic field.

1.4 Magnetic Resonance Electrical Property Tomography (MR-EPT)

To measure the complex permittivity of a liquid sample, one would use a dielectric probe and a network analyzer. This provides the complex permittivity values for a wide range of frequencies. However, this method is not feasible in vivo. MRI is naturally a reasonable option as a tool for calculating complex permittivity due to its use of magnetic fields.

First proposed by Haacke et al. (54) and further described by Katscher et al. (55), MR-EPT involves measuring magnetic fields with a MRI scanner to calculate

electrical properties. While [1.2] relates κ to the magnetic field $\mathbf{H}$, the magnetic field and magnetic flux density, $\mathbf{B}$, are related by the constitutive relationship $\mathbf{B} = \mu\mathbf{H}$. Due to the linearity of the terms in [1.2] one can replace $\mathbf{H}$ with $\mathbf{B}$. The term *field* will be used to describe both of these quantities. There are several magnetic fields at play in a MRI scanner, but one of the easiest to measure is the transmit radiofrequency (RF) field, $\mathbf{B}_1^+$. More details about the MRI data acquisition is discussed in the next section. Rearranging the terms in [1.2] yields the governing equation for MR-EPT:

$$\kappa = \frac{-\nabla^2 \mathbf{B}_1^+}{\omega^2 \mu_0 \mathbf{B}_1^+}. \qquad [1.3]$$

The right hand side of this equation is complex-valued. The real part of κ is the relative permittivity and the imaginary part is multiplied by ω to calculate conductivity.

1.5 Magnetic Resonance Imaging Considerations

The primary magnetic fields in a MRI experiment are the static field $\mathbf{B}_0$, and the RF field, $\mathbf{B}_1$. We also use gradient fields to provide spatial variation in the strength of the magnetic field. The Helmholtz wave equation holds for any time harmonic magnetic field. Thus, the static $\mathbf{B}_0$ field will not be useful for MR-EPT. There has been some exploration into the feasibility of using eddy currents induced by switching gradients for conductivity imaging, which would result in MR-EPT at much lower frequencies than the typical MHz range (56–58). The general conclusion is that the signal contributions from the fields induced by the eddy currents fall below the noise floor in a typical MRI scan, making this approach impractical. This leaves us with the field $\mathbf{B}_1$, which has two components: $\mathbf{B}_1^+$, the transmit RF field, and $\mathbf{B}_1^-$, the receive RF field or the sensitivity to relaxing spins of the receive coil (59). There exist methods for measuring $\mathbf{B}_1^+$, but not $\mathbf{B}_1^-$, which is why we use the transmit RF field for MR-EPT.

Methods for measuring the $\mathbf{B}_1^+$ field typically measure magnitude or phase, but not both. The accuracy of MR-EPT relies on the accuracy of these measurements, but there are tradeoffs between accuracy and feasibility. There are several methods for measuring the magnitude of $\mathbf{B}_1^+$, including the double angle method (60), actual flip-angle imaging (61), and the Bloch-Siegert method (62). Measuring the exact phase of $\mathbf{B}_1^+$ is more challenging than measuring the exact magnitude because the phase of an MR image, often called the transceive phase, is the superposition of the transmit and receive phases. For a coil operating in quadrature, Wen observed that, if only considering the near field, the transmit and receive phases are approximately equal (63). This gives rise to the transceive phase assumption, which states that the transmit phase can be approximated as half of the phase of an MR image. However, to use this approximation, MR phase data must be free from contributions due to off-resonance effects, eddy currents, motion, and flow. This can be achieved with a spin echo sequence or a balanced steady state free precession scan (64). A spin echo sequence is free from off-resonance effects due to the 180° pulse. However, to minimize the eddy current effects, the spin echo sequence must be acquired twice with opposite slice-select gradient polarities. Ideally, the eddy currents induced by the slice select gradient will be equal and opposite, so if the two resultant phase images are averaged the phase contributions due to eddy currents will cancel out. Contributions from motion can be mitigated with instructions to the subject and providing padding or restraints to prevent movement. Contributions due to flow can be minimized by prescribing saturation bands (65). An additional strategy for minimizing flow artifacts in large vessels is described in Chapter II. A single steady-state free-precession (SSFP) sequence has similar properties to the spin echo sequence with respect to off-resonance and eddy currents, so it is also a viable candidate for measuring the transceive phase.

1.6 Phase-Based Conductivity Mapping

Two MRI scans are typically required to acquire the complex-valued $\mathbf{B}_1^+$ field - one for the magnitude and one for the phase. An important observation by Wen (63) noted that, to the leading order, the conductivity of a material primarily affects the phase of the magnetic field and the permittivity primarily affects the magnitude of the magnetic field. Let us write the magnetic field quantity as a product of the magnitude and phase components,

$$\mathbf{B}_1^+ = |\mathbf{B}_1^+| exp(i\phi^+) \quad [1.4]$$

where $|\mathbf{B}_1^+|$ is the magnitude of the transmit RF field and ϕ^+ is the phase of the transmit RF field. Expanding the real and imaginary parts of Equation 1.3 gives the following expressions:

$$\epsilon = \frac{1}{\omega^2 \mu_0} \left[|\nabla \phi^+|^2 - \frac{-\nabla^2 |\mathbf{B}_1^+|}{|\mathbf{B}_1^+|} \right] \quad [1.5]$$

and

$$\sigma = \frac{1}{\omega \mu_0} \left[\nabla \phi^+ \cdot \nabla \ln |\mathbf{B}_1^+| + \nabla^2 \phi^+ \right]. \quad [1.6]$$

With some assumptions, we can write two simplified approximations for calculating electrical properties, which are described in detail by Voigt et al. (66). The first is the magnitude-based permittivity approximation:

$$\epsilon \approx \frac{-\nabla^2 |\mathbf{B}_1^+|}{\omega^2 \mu_0 |\mathbf{B}_1^+|}. \quad [1.7]$$

Simplifying Equation 1.5 to Equation 1.7 requires the assumption that $\frac{-\nabla^2 |\mathbf{B}_1^+|}{|\mathbf{B}_1^+|} \gg |\nabla \phi^+|^2$, or that the gradient of the phase is much less than the curvature of the magnitude.

The second is the phase-based conductivity approximation:

$$\sigma \approx \frac{\nabla^2 \phi^+}{\omega \mu_0}. \qquad [1.8]$$

where ϕ^+ is the phase of the transmit RF field, or the transmit phase. It is crucial that the phase maps used in this calculation have been unwrapped because the Laplacian calculation requires a small neighborhood of pixels. To simplify Equation 1.6 to Equation 1.8, we must assume that $\nabla^2 \phi^+ \gg \nabla \phi^+ \cdot \nabla \ln|\mathbf{B}_1^+|$, or that the gradient of the magnitude is much less than the curvature of the phase. This is often simplified to the assumption that the magnitude of the transmit RF field is relatively constant. As the static magnetic field strength increases, the $\mathbf{B}_1^+$ magnitude becomes less uniform and phase-based conductivity mapping is more biased (67). The phase-based conductivity approximation is generally acceptable for 1.5T and 3.0T MRI scanners. The assumptions for magnitude-based permittivity mapping and phase-based conductivity mapping are somewhat contradictory. According to (67), the magnitude-based permittivity mapping approximation is better for higher field strengths, opposite of the phase-based conductivity approximation.

The linearity of the phase-based conductivity approximation supersedes the transceive phase assumption discussed in the previous section, allowing for any coil to be used for phase-based conductivity mapping. The theory is as follows.

One can measure conductivity from either the transmit or receive phase, both giving the same value of σ. The transceive phase contains both of those phase quantities even if they are unequal. Thus, the conductivity is

$$\sigma = \frac{\nabla^2 \frac{(\phi^+ + \phi^-)}{2}}{\omega \mu_0} = \frac{1}{2}\left(\frac{\nabla^2 \phi^+}{\omega \mu_0} + \frac{\nabla^2 \phi^-}{\omega \mu_0}\right) = \frac{2\sigma}{2}. \qquad [1.9]$$

Due to the linearity of the phase-based approximation, we can simply divide the transceive phase by two to calculate conductivity. Alternatively, the resultant con-

ductivity calculation based on the transceive phase could be divided by two.

Figure 1.1 shows an example of the transceive phase measured in the brain of a human subject. The phase map is relatively smooth and has an overall quadratic shape, colloquially known as bowl-shaped. Equation 1.8 tells us that the conductivity of a material is proportional to the curvature of the phase map, or the curvature of this bowl. While the curvature appears to be constant, there are subtle variations that will lead to spatially varying conductivity maps.

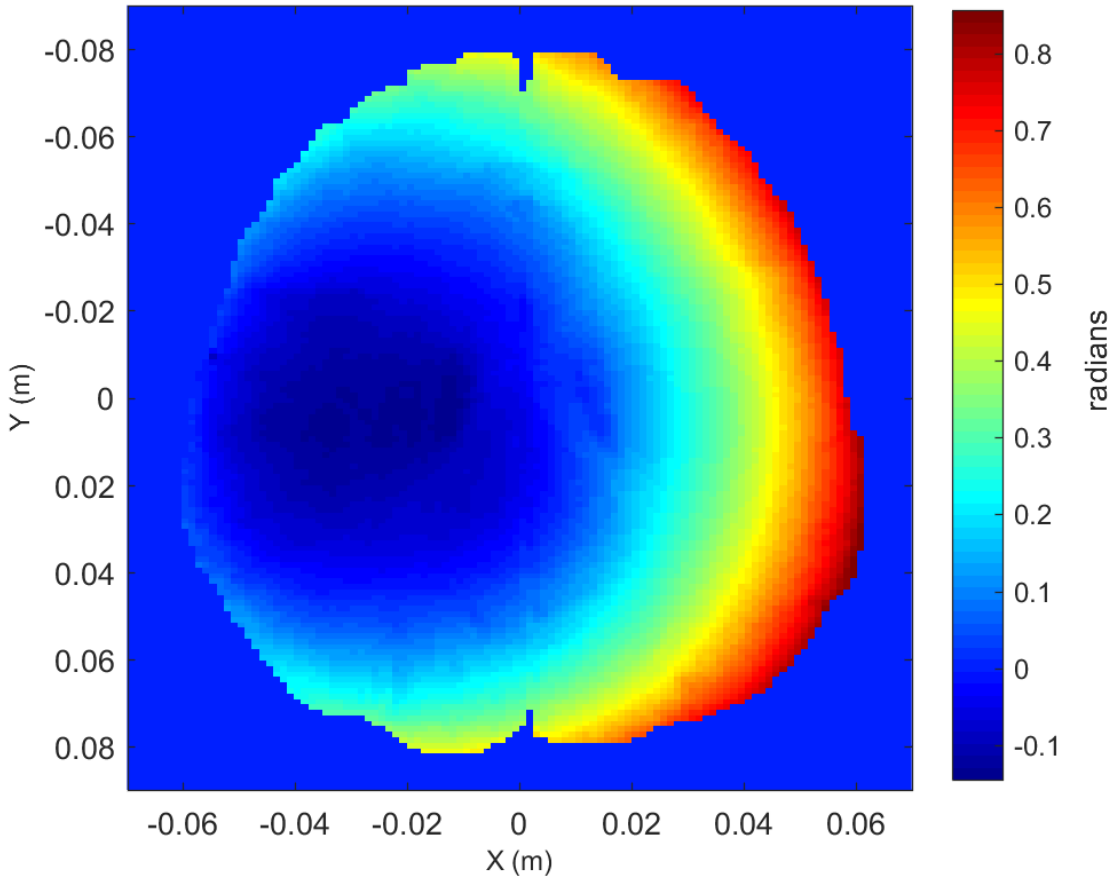

Figure 1.1: Representative transmit RF phase map from a human subject's brain.

In summary, the phase-based conductivity approximation simplifies both the acquisition and calculation for conductivity mapping. Only the phase of the transmit field is required, halving the data acquisition requirements. Additionally, any coil

can be used for conductivity mapping because the linearity of the approximation supersedes the transceive phase assumption.

1.7 Limitations and Current Approaches

The primary limitation of MR-EPT and other conductivity mapping approaches is the lack of a gold standard in vivo. For phantoms, one can measure a sample of the liquid or gel using a dielectric probe attachment on a network analyzer. However, this cannot be used in vivo. Reported textbook values on the conductivity of human tissues have been measured on excised samples, potentially introducing error. Therefore, much of the quantitative analysis on conductivity mapping approaches must be done in simulation or phantoms.

In terms of calculating conductivity, SNR and boundary artifacts often obscure the accuracy of the estimates. The low SNR comes from the Laplacian operator, which amplifies noise in measured magnetic field data. The boundary artifacts arise from using the homogeneous Helmholtz equation, which is not valid at the boundary of materials with two different conductivities. More details about these issues will be described in Chapter II.

A common approach to conductivity or complex permittivity mapping is to apply the MR-EPT equations to measured $\mathbf{B}_1^+$ data and apply some variety of a spatial filter to either the $\mathbf{B}_1^+$ images, the conductivity images, or both. A number of filters have been used in the literature, but they all have a trade-off between filtering out noise and smoothing over fine details in the image. There has been work on the utility of magnitude images in the filtering process to help preserve small details (17, 68), studying boundary artifacts (68, 69), exploring the assumption that conductivity must be homogeneous (70, 71), improving SNR issues (17, 72–76), and other artifacts in MR-EPT (69, 77). There has also been work on improving conductivity mapping with alternative problem formulations to MR-EPT. Some present alternative forms

of the forward problem, calculating conductivity from measured magnetic fields (78–81). Other formulate the reconstruction as an inverse problem (82–88). Katscher et al. (89) have also proposed a dictionary-based EPT algorithm. In most of these formulations, the experiments are limited to simulations and experimental phantoms, due to the complexities involved in implementing these advanced techniques in vivo.

1.8 Dissertation Structure

This dissertation is comprised of three main chapters of research. Chapter II is a novel regularized, model-based approach to phase-based conductivity mapping. This method provides a full three-dimensional conductivity map and can be implemented on a desktop computer. Chapter III focuses on combining multi-channel data for MR-EPT. This is a novel method that does not require a reference scan or reference coil, but yields combined phase data that contains the low and high spatial frequency content required for MR-EPT. Chapter IV describes a proof of concept for measuring conductivity tensors in the MRI scanner. This is the first demonstration of measuring the full tensor in practice.

CHAPTER II

Model-Based Conductivity Mapping with Regularization

2.1 Introduction

The primary issues in MR-EPT are boundary errors and low SNR. The boundary errors arise from the assumption that the electrical properties are spatially constant. The violation of this assumption is most prominent at material boundaries, but can also be problematic in inhomogeneous materials. Seo et al. (70) provided a mathematical analysis of this error and Duan et al. (71) investigated the error magnitude at various tissue interfaces. Boundary errors are evident in the phase-based conductivity approximation as well. According to Equation 1.8, if a material has a spatially constant conductivity it will have a parabolic phase profile. At the boundary of two materials, there is a transition region between two parabolas. Naturally this would form a cusp, but phase maps are inherently smooth and, instead, an apparent inflection in the curvature is observed. This can lead to negative calculated conductivity values. Low SNR results from calculations that rely on the Laplacian operator. Electrical properties are proportional to the Laplacian of the measured magnetic fields, so their calculation amplifies any noise incurred during the MRI scan. Several methods have been proposed to minimize one or both of these issues, such as gradient-based

approaches (78–80, 90), magnitude image-based filter kernels (17, 68), and inverse approaches.

There have been a few proposed MR-EPT methods focused on solving the inverse problem as opposed to the forward problem. Balidemaj et al. developed the Contrast Source Inversion approach (CSI-EPT) (82), which is based on global integral representations for the electromagnetic field quantities. CSI-EPT includes a Total Variation regularization term to reduce noise and does not rely on the assumption that conductivity is constant. Resultant conductivity maps for numerical phantoms show excellent recovery of small details and tissue boundaries. However, CSI-EPT requires knowledge of the background field, which is the field present in the scanner in the absence of a dielectric object. To the best of our knowledge, this method has not been extended to three-dimensions and also has only been used in numerical experiments. Borsic et al. (84) proposed an Inverse Problems approach more similar to the method we present in this paper. Their Inverse Problems Approach also updates the conductivity maps based on the difference between the forward problem formulation and the measured data. They have tested both quadratic and Total Variation regularization schemes. The Total Variation formulation results in excellent recovery of boundaries in numeric and experimental phantoms, but the method has not been tested in vivo. Furthermore, this method presents a computational burden, which the authors have mitigated by subdividing the problem, but there exist some discontinuities at the boundary between subdivisions.

As an alternative to MR-EPT, Local Maxwell Tomography (LMT) (91, 92) and Global Maxwell Tomography (GMT) (88, 93) have been proposed in recent years, and are also formulated as inverse problems. LMT does not require assumptions about RF phase or the coil structure and was generalized to solve for tensors and rapidly varying electrical properties. However, the approach requires multi-channel transceivers. GMT is based on volume integral equations and, as such, requires

appropriate solvers. GMT uses only the magnitude of the RF field, so it does not rely on phase assumptions. To the best of our knowledge, LMT and GMT have only been demonstrated in numerical phantoms.

We use magnitude information from the MRI images as *a priori* information in our proposed reconstruction process, specifically to identify a region of support and identify tissue boundaries. Magnitude information has previously been used to adapt the filter kernel shape and size to the anatomy in both Gaussian filtered Laplacian (68) and parabolic fitting (17) approaches. Both methods have reduced the size of boundary artifacts.

In this chapter we propose a novel method for phase-based conductivity mapping that includes a model-based approach with regularization. The aim of this approach is to produce conductivity maps with higher accuracy by reducing noise amplification and boundary artifacts. This is a 3D method that uses magnitude information as *a priori* information to improve the phase-based conductivity reconstruction. Furthermore, we explore the benefits of including a non-negativity constraint to reduce boundary artifacts. We demonstrate this method in numerical simulations, a saline phantom, and human subjects. [1]

2.2 Theory

We propose an estimator for penalized weighted least-squares reconstruction of a conductivity map as

$$\hat{\boldsymbol{\sigma}} = \arg\min_{\sigma} \frac{1}{2}\left|\left|\frac{\boldsymbol{\phi}^{+}}{\omega\mu_0} - \mathbf{L}\boldsymbol{\sigma}\right|\right|^2_{\mathbf{W}_1} + \beta R(\boldsymbol{\sigma}, \mathbf{W}_2), \qquad [2.1]$$

[1] Parts of this chapter have been published in: K.M. Ropella and D.C. Noll, A Regularized, Model-Based Approach to Phase-Based Conductivity Mapping Using MRI, Magnetic Resonance in Medicine, 2017;78:2011-2021.

where $\hat{\boldsymbol{\sigma}}$ is the optimal conductivity estimate, ω is the Larmor frequency of the MRI scanner, μ_0 is the permittivity of free space - a constant, $\boldsymbol{\phi}^+$ is the unwrapped measured transmit phase data, $\mathbf{L}$ is a system model relating the two, R is a regularization function, and β is the regularization parameter. The weighting matrix $\mathbf{W}_1$ incorporates *a priori* information into the problem by determining the region of support. The first term on the right hand side of the Eq. [2.1] is the data fit term, which enforces the relationship between tissue conductivity and $\boldsymbol{\phi}^+$ described in Eq. [1.8]. The second term is a penalty, or regularization, term which incorporates some previous knowledge of the object to improve the fidelity of the reconstruction.

In this problem, the system model $\mathbf{L}$ can be described as a filter representing an approximate inverse of the discrete Laplacian operator, ∇^2, where:

$$\nabla^2 = \frac{\partial^2}{\partial x^2} + \frac{\partial^2}{\partial y^2} + \frac{\partial^2}{\partial z^2} \tag{2.2a}$$

$$\frac{\partial^2}{\partial x^2} f(x,y,z) = \frac{f(x-1,y,z) - 2f(x,y,z) + f(x+1,y,z)}{h_x^2} \tag{2.2b}$$

$$\frac{\partial^2}{\partial y^2} f(x,y,z) = \frac{f(x,y-1,z) - 2f(x,y,z) + f(x,y+1,z)}{h_y^2} \tag{2.2c}$$

$$\frac{\partial^2}{\partial z^2} f(x,y,z) = \frac{f(x,y,z-1) - 2f(x,y,z) + f(x,y,z+1)}{h_z^2} \tag{2.2d}$$

where h_x, h_y, h_z are the voxel dimensions. For isotropic unit voxels, this equates to the $3 \times 3 \times 3$ matrix ∇^2, where at the center point ∇^2 is -6 and at the six adjacent neighbors to the center ∇^2 is 1. In other words, $\nabla^2(0,0,0) = -6$ and $\nabla^2(\pm 1,0,0) = \nabla^2(0,\pm 1,0) = \nabla^2(0,0,\pm 1) = 1$. For anisotropic voxels, Eqs. 2.2b-2.2d are scaled by the appropriate voxel dimensions, and the ones in ∇^2 will vary with the voxel size.

The inverse of this operator is calculated by zero-padding this kernel to the size of the data, taking the 3D fast Fourier transform (FFT), and inverting the FFT coefficients. Since the FFT of the Laplacian operator is zero-valued at DC, inverting

that coefficient is ill-conditioned. To mitigate this problem, we added a small offset, δ, to the DC coefficient of the Laplacian. Taking the inverse FFT of the inverted coefficients results in the Inverse Laplacian (IL) filter $\mathbf{L}$.

Similar to calculating the Laplacian of phase data, the IL calculation requires the convolution of $\boldsymbol{\sigma}$ with the IL filter. To keep consistent with least-squares notation, we represent the IL filter as a matrix, but in actuality this filter is an operator, where

$$\mathbf{L}\boldsymbol{\sigma} := \mathcal{F}^{-1}\{\mathcal{F}\{\boldsymbol{\sigma}\} \cdot \mathcal{F}\{\mathbf{L}\}\}.$$

The $\mathcal{F}$ operator is the FFT.

The regularizer for this problem, $R(\boldsymbol{\sigma}, \mathbf{W}_2)$, uses a three-dimensional roughness penalty, which can be written as:

$$R(\boldsymbol{\sigma}, \mathbf{W}_2) = \sum_{j=1}^{J} \sum_{k=1}^{K} \mathbf{W}_2(k, j)\psi([\mathbf{C}_j\boldsymbol{\sigma}]_k). \quad [2.3]$$

This regularization term encourages a smooth conductivity map because the matrix $\mathbf{C}$ is the first order finite difference operator with size K voxels by K voxels by J pairs of differences. For a three-dimensional data set with size $M \times N \times P$, $K = NMP$. This regularizer calculates a weighted sum of the differences between the voxel of interest and its nearest adjacent neighbor in all 3 dimensions, so $J = 3$ and there is one $\mathbf{C}_j$ for each dimension. In this formulation, $\boldsymbol{\sigma}$ is a vectorized version of the conductivity map with length K voxels. The function $\psi(t)$ is a potential function that operates on each element of $[\mathbf{C}_j\boldsymbol{\sigma}]$. In this work we use a hyperbola potential function (94, 95). This allows us to penalize any roughness in $\boldsymbol{\sigma}$ in a non-linear fashion, with larger penalties associated with larger values of $[\mathbf{C}_j\boldsymbol{\sigma}]$. The values of the hyperbola form of $\psi(t)$ grow in a quadratic fashion for small values of t and in a linear fashion for large values of t, which gives the hyperbola potential function edge-preserving qualities. This is favorable for conductivity mapping because we have already neglected object edges

in the system matrix by using the homogeneous Helmholtz equation. The weighting matrix $\mathbf{W}_2$ is a binary mask of size K voxels by J pairs of differences.

The matrices $\mathbf{W}_1$ and $\mathbf{W}_2$ are used to mask out certain parts of the image based on *a priori* information. While this work focuses on phase-based conductivity mapping, the scan protocol used to acquire the phase image also provides a magnitude image at no extra cost. In addition, we acquire an MR angiogram because vessels can cause spurious phase information. The mask $\mathbf{W}_1$ dictates the region of support for the problem, which excludes any vessels from the angiogram as well as regions of the magnitude image with very low signal. The mask $\mathbf{W}_2$ determines the regions on which regularization should be applied. The finite differences matrix $\mathbf{C}$ is applied to the magnitude image and the result is thresholded to determine the important edges in the object. These large edges are excluded from regularization under the assumption that edges in the conductivity maps will coincide with edges in the anatomical images, and we do not wish to regularize across these boundaries. Because we want to regularize in each of the three dimensions, $\mathbf{W}_2$ is a matrix of size K voxels times J pairs of differences so that we can weight the regularization directions independently. Masks $\mathbf{W}_1$ and $\mathbf{W}_2$ are valued 0 for voxels to be excluded from the calculation and 1 elsewhere. When a voxel in a given mask is zero-valued, that voxel becomes a 'don't care' voxel for the data fit term, regularization term, or both. An example of the masks is shown in Figure 2.6. We solve this optimization problem using the conjugate gradient method, implemented using tools from Michigan's Image Reconstruction Toolbox (96).

The regularization parameter β determines the balance between accurate modeling of the data and smoothing the results with regularization. While methods exist to optimally select the regularization parameter β, we selected the parameter value to approximately match the spatial resolution of the traditional filtering methods. In this work we chose a restricted Gaussian filter for comparison. When employing Gaussian

smoothing in the conductivity calculations, the two main reconstruction steps are to 1) calculate the Laplacian and 2) apply the filter. In the IL approach the data fit term includes the Laplacian operator and the regularization term enforces some level of smoothness. Since the data fit term is derived from the Laplacian operator, we can show that, in the absence of noise, the IL method with no regularization will produce highly accurate conductivity maps, as will the Laplacian operator. Therefore, we directly compare the spatial resolution properties of the Gaussian filter with those of the regularization term. Some EPT literature (68, 70, 97) uses filter widths of 5 voxels, so we compare the point spread function (PSF) full-width-at-half-maximum (FWHM) values for 5x5 Gaussian filters with a range of different standard deviation values to those of the finite differences regularizer with a hyperbola potential function for a range of β values. We did not include the edge mask $\mathbf{W}_2$ in the regularization term, as this would certainly exclude the point object from regularization and thus prevent the calculation of the PSF. Results from this experiment are shown in Figure 2.1. We selected a filter standard deviation of 1 voxel to match the filters used in (68, 70, 97), and a corresponding β value of 1. It is worth noting that this matching procedure equates the spatial resolution properties for these two methods for a given impulse amplitude. Due to the nonlinear nature of the regularizer, its smoothing properties will vary depending on the amplitude of the differences. We selected a point object amplitude of 0.3 to represent the approximate conductivity difference between white and gray matter. We are less concerned about larger amplitude point objects because of the edge-preserving nature of the regularizer and possible assistance from the edge mask.

A flowchart describing the workflow is given in Figure 2.2.

A non-negativity constraint is also explored as an optional feature of the proposed conductivity mapping method. The non-negativity constraint is based on the fact that only non-negative conductivity values are feasible solutions. This is implemented in

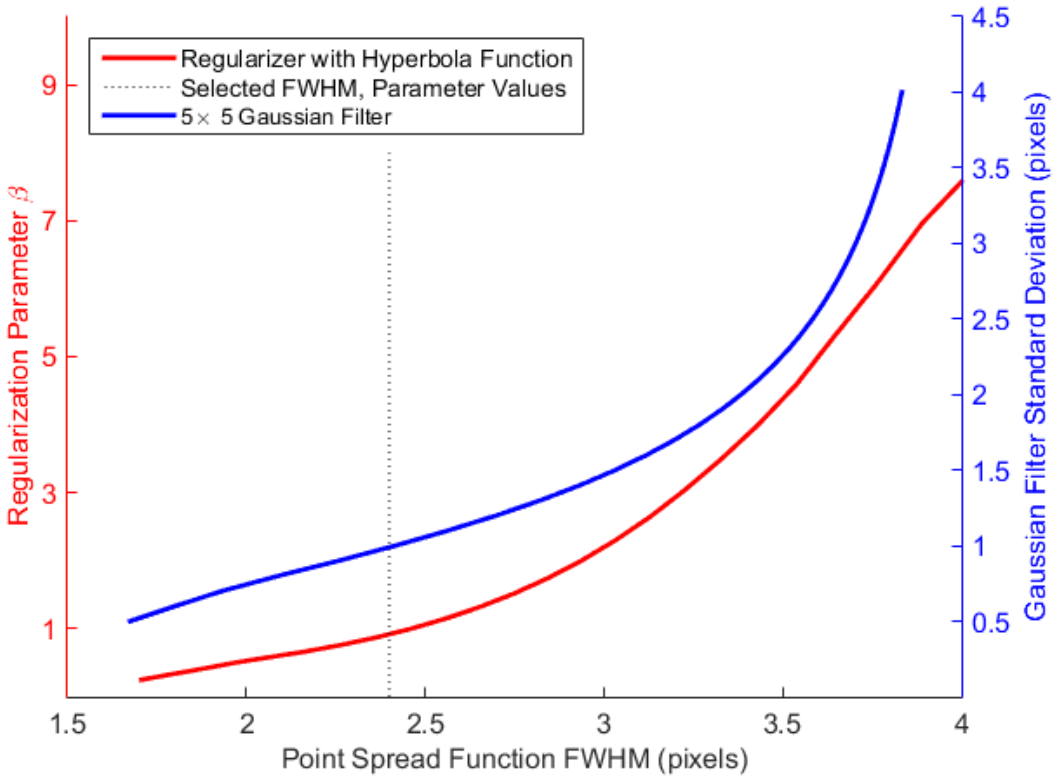

Figure 2.1: Comparison of spatial resolution for each reconstruction method. For a given PSF width we are able to select corresponding regularization parameter and filter standard deviation. Selected parameters are denoted by the dotted line.

the optimization algorithm and does not require any additional data or masks. We used the conjugate gradient algorithm in both the unconstrained and unconstrained cases. By applying the non-negativity constraint in this manner, the conjugate gradient algorithm is not guaranteed to converge. This is a heuristic extension of the conductivity algorithm.

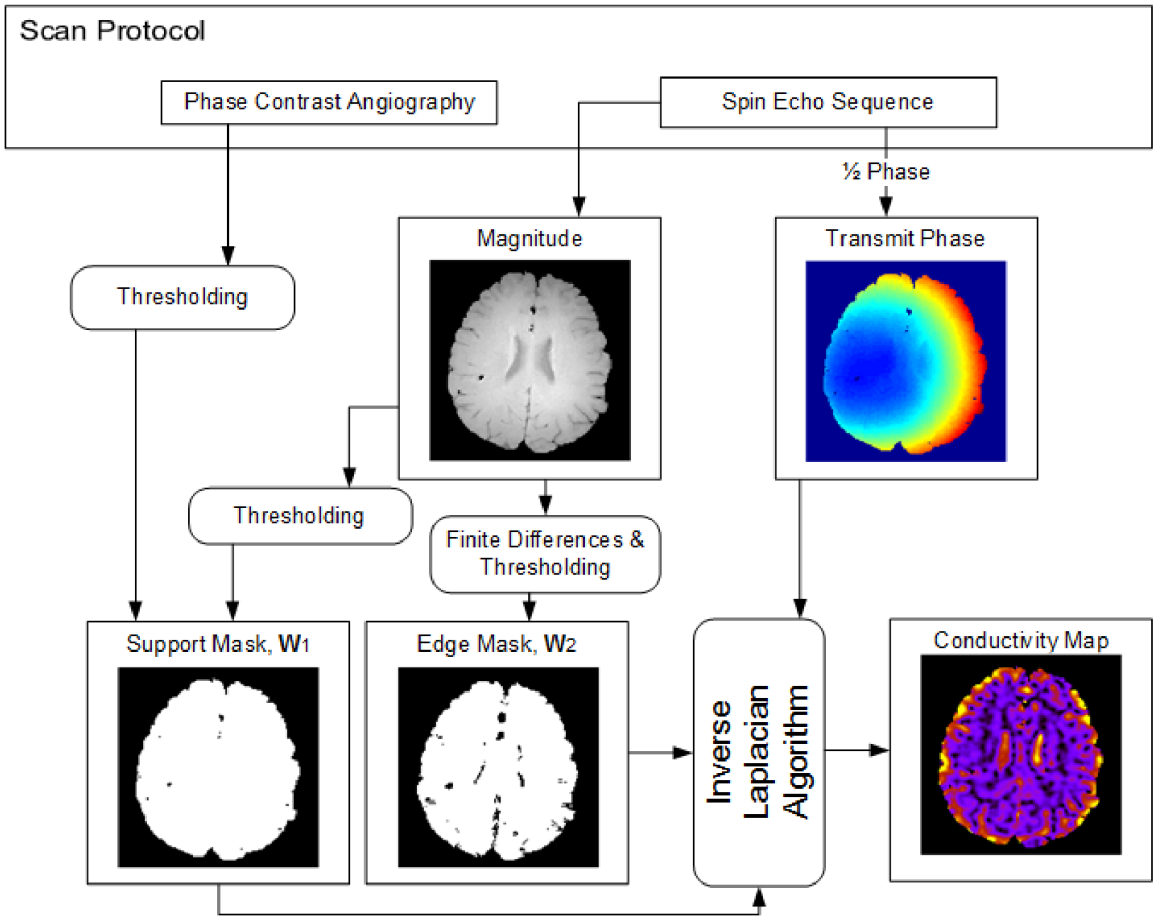

Figure 2.2: Workflow for the data acquisition and processing associated with the proposed Inverse Laplacian algorithm. The data required are the intensity projections from a phase-contrast angiogram and the complex image data from a spin echo sequence. The inputs to the Inverse Laplacian algorithm are the support mask, $\mathbf{W}_1$, an edge mask, $\mathbf{W}_2$, and the transmit phase, calculated from spin echo data using the transceive phase assumption.

2.3 Methods

2.3.1 EPT Reconstruction

Phase data was unwrapped prior to reconstruction using the method in (98). The conductivity map reconstructions were first performed using the proposed IL method with $\beta = 1$. To determine the appropriate DC offset value, δ, for the IL filter, the value of δ was varied between 10^{-2} and 10^{-7}. No noise was added to the simulation

data for the δ experiments.

The proposed IL method also relies on circulant operations in calculating the inverse of the Laplacian and the regularization term. The images have plenty of zero-padding in the x- and y-directions, but a slice of zeros was added to both the top and bottom of the volume.

The proposed method was compared against a restricted Gaussian filter. This method also requires both the magnitude and the phase of the spin echo (SE) image. First the conductivity was calculated according to Eq. [1.8] using the discrete Laplacian kernel ∇^2. Zero-padding in the z-direction was also used in the Gaussian filter method because circulant end conditions were used to calulate the Laplacian. The Gaussian filter was a $5 \times 5 \times 5$ kernel with a standard deviation of 1 voxel, applied to the raw conductivity images. The filter was restricted to include voxels within the kernel that had a magnitude intensity within 20% of the center voxel, as described in (17). For both the Gaussian filter method and IL method without non-negativity constraint, to reflect the fact that conductivity must be non-negative, any resultant negative conductivity values were set to zero.

The proposed IL method was also adapted to include a non-negativity constraint, implemented by projecting the conductivity estimate at each iteration of the optimization problem onto the set of non-negative values.

2.3.2 Numerical Simulations

Numerical simulations were performed using SEMCAD X (SPEAG, Switzerland). The model consisted of a birdcage coil and a cylindrical, two compartment phantom. The outer compartment was assigned the material properties of gray matter (σ_{GM} = 0.59 S/m) and the inner compartment was assigned the material properties of cerebrospinal fluid (CSF) (σ_{CSF} = 2.14 S/m). Simulations were performed at 128 MHz with $0.4 \times 0.4 \times 0.4$ mm^3 voxels. Since $\mathbf{B}_1^+$ is a direct product of the simulation,

it was used in the reconstruction.

Zero-mean additive white Gaussian noise (AWGN) was added independently to the real and imaginary parts of the data. The standard deviation of the noise was varied from $10^{-3.8}$ to $10^{-2.5}$ to achieve a range of SNR values of 50 - 76 dB. Conductivity maps were reconstructed using the proposed IL method and the restricted Gaussian filter method. Furthermore, no angiogram information was included. At each noise standard deviation level, both reconstruction methods were repeated for 100 noise realizations. In both Gaussian filtering and the IL method, there exists a trade-off between accuracy of the conductivity maps (e.g. bias) and noise. Bias will be evident in the conductivity maps regardless of the SNR of the input data and, in our experience, dominates the root-mean-square error (RMSE) calculation. Therefore, to measure the amount of bias we averaged the conductivity maps over all realizations for each noise level. To give a more representative measure of the effective conductivity map SNR, we subtracted this mean error at the respective noise level from each realization before calculating the standard deviation of the conductivity values across all 100 realizations.

Conductivity values were calculated using the IL method, with and without the non-negativity constraint, and the restricted Gaussian filter method after AWGN with a standard deviation of 5×10^{-4} was added to the simulation data. The experimental mean and standard deviation values were calculated under two conditions. First, using all voxels for a given material and, second, after eroding each material region using a 9×9 square element. The erosion was performed to calculate the error without the edge artifacts, a means of separating bias from noise.

The IL method was also used to calculate conductivity values with and without the edge mask, $\mathbf{W}_2$, after AWGN with a standard deviation of 10^{-4} was added to the simulation data.

2.3.3 Dielectric Phantom

An aqueous phantom was constructed using two cylindrical plastic containers to provide conductivity contrast. The outer container contained a solution of 7.5 g/L NaCl, to increase the conductivity, and 1 g/L copper sulfate, to reduce the relaxation constants. The inner container, allowed to move freely within the larger vessel, was filled with only deionized water. We measured the conductivity of the outer container to be 1.38 S/m using a dielectric probe. We used 0 S/m as the true conductivity value of the inner container. Conductivity maps were reconstructed using the proposed IL method, with and without the non-negativity constraint, and the restricted Gaussian filter method. Angiogram information was not used for the dielectric phantom. The same region erosion procedure used for the simulation data was used for the phantom data.

2.3.4 In Vivo Experiment

Four healthy volunteers were scanned under approval by the Institutional Review Board at the University of Michigan. Conductivity maps were reconstructed using the proposed IL method, with and without the non-negativity constraint, and the restricted Gaussian filter method.

2.3.5 Scan Protocols

All experiments were performed on a GE Discovery MR750 3.0T MRI scanner (GE Healthcare, Waukesha, WI) using a birdcage head coil. Data was acquired using a 2D SE sequence with TE/TR = 16/1200 ms, FOV = $24 \times 24 \times 2.1$ cm, with $1.25 \times 1.25 \times 3$ mm^3 voxels. Data was acquired twice using the SE sequence with opposite slice select gradient polarity and averaged to mitigate the effect of eddy currents. The transmit phase, ϕ^+, was calculated by dividing the unwrapped transceive phase of the SE image by two.

A phase contrast angiogram was acquired for each human subject with the same slice prescription as the SE scan. The peak encoded velocity was set to 15 cm/s.

For the human subjects, a T1-weighted image was acquired using a 2D spoiled gradient echo sequence with the same slice prescription as the SE sequence. This image was used for segmentation with SPM8 (99). Each voxel was classified as either gray matter, white matter, or CSF with probability greater than 95%. Voxels not meeting this criteria for any tissue type were left unassigned. The segmented images were used to calculate mean and standard deviation of the conductivity values for each tissue type. Mean tissue values across all subjects were calculated as the mean of individual subject means, weighted by the number of voxels in the tissue segment. The standard deviations across all subjects were calculated as the square root of the mean of the subject variances, also weighted by segment size.

All conductivity calculations were performed in 3D, but results are displayed for representative slices from the reconstructed volumes. Mean and standard deviation values reported in tables were calculated over the volume, excluding the top and bottom slices to exclude artifacts in the Gaussian filter reconstruction due to applying the Laplacian kernel at the edge of the volume.

2.4 Results

2.4.1 Simulation Data

Figure 2.3 shows the conductivity maps for noise standard deviation $= 5 \times 10^{-4}$, reconstructed using the Gaussian filter and both IL methods. Mean and standard deviations for each region and reconstruction method are reported in Table 2.1. The eroded regions used to calculate the mean and standard deviations are shown in Figure 2.4.

Figure 2.5 shows the resultant conductivity maps for varying values of δ. For

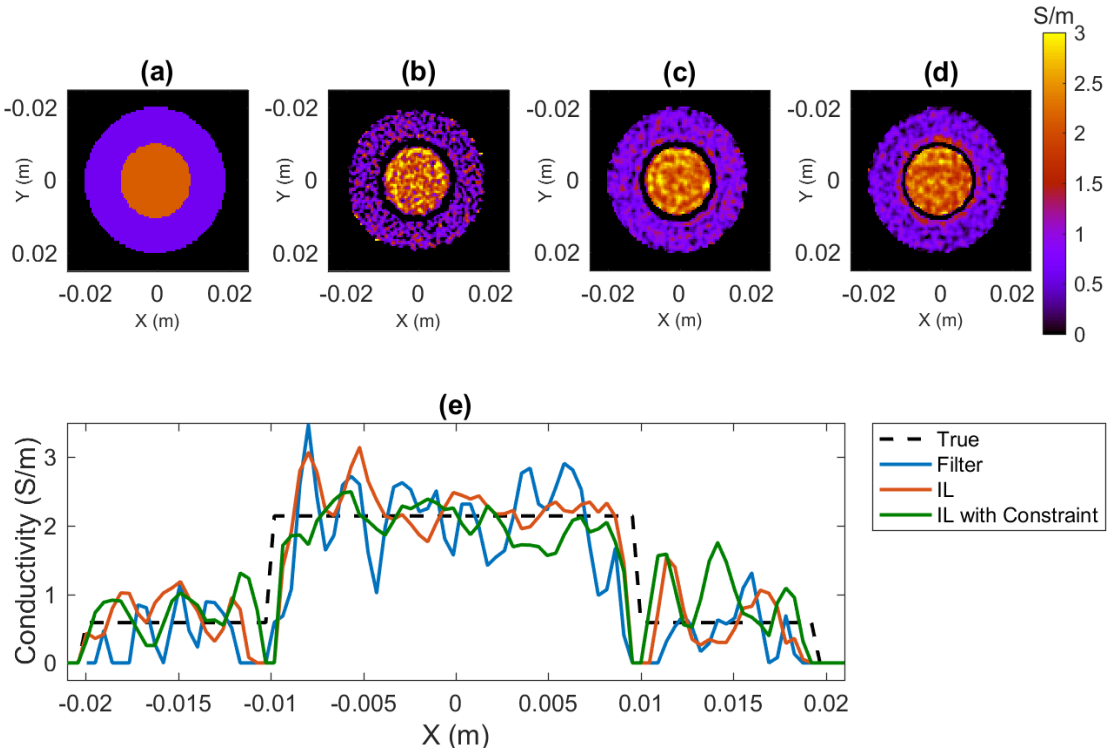

Figure 2.3: Conductivity maps for the simulation experiments. AWGN was added to the complex data with standard deviation = 5×10^{-4}. (a) True conductivity (b) Restricted Gaussian filter reconstruction (c) Inverse Laplacian reconstruction (d) Inverse Laplacian reconstruction with non-negativity constraint (e) Profiles through y=0.

values of $\delta = [10^{-2}, 10^{-3}, 10^{-4}]$ the conductivity maps are nearly identical. Some cross-hatching is visible, but we believe this is simulation artifact. Conductivity maps calculated with values of δ closer to zero result in more ringing and a loss of the sharp transition between compartments. For all experiments, we used $\delta = 10^{-3}$ to minimize the bias due to the DC offset.

The effects of the masks used in the IL approach are shown in Figure 2.6. The method does not yield accurate conductivity maps when no region of support is specified. This is primarily due to the lack of data in the background region. Without the support mask, $\mathbf{W}_1$, the model attempts to fit the sharp edge in the phase at the object border resulting in spurious conductivity values. The edge mask, $\mathbf{W}_2$, helps

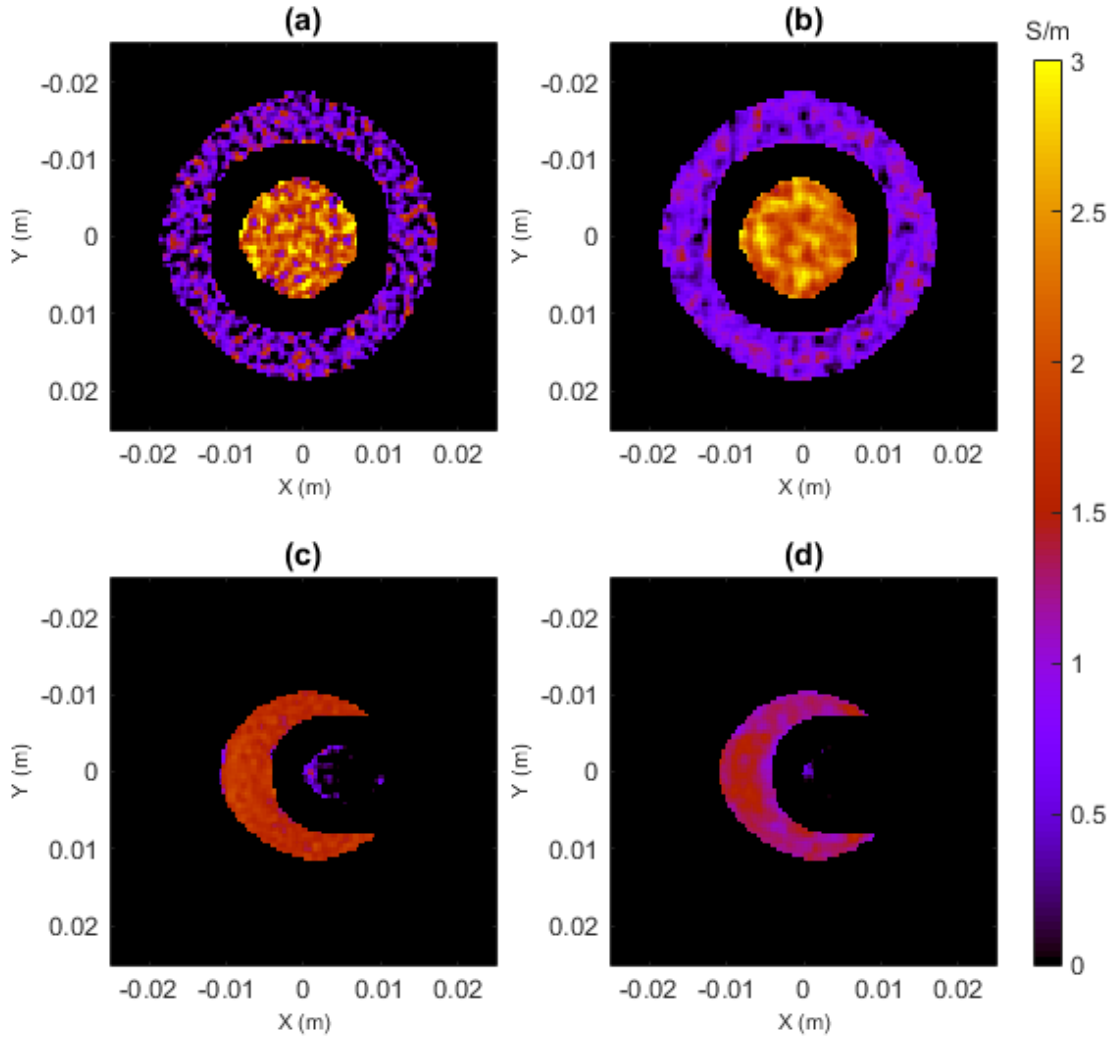

Figure 2.4: Fraction of conductivity images used to calculate mean values after dilating the compartment masks with a 9x9 pixel square. Simulation reconstructed with (a) restricted Gaussian filter and (b) Inverse Laplacian method. Phantom reconstructed with (c) restricted Gaussian filter and (d) Inverse Laplacian method.

to retain information close to material boundaries where large jumps in conductivity occur. It is clear from Figure 2.6 that the edge artifact at the boundary between the two materials is reduced in width by using the edge mask. Excluding the edge pixels from regularization also allows for more accurate conductivity calculations adjacent to these pixels because the transition between compartments is not regularized and

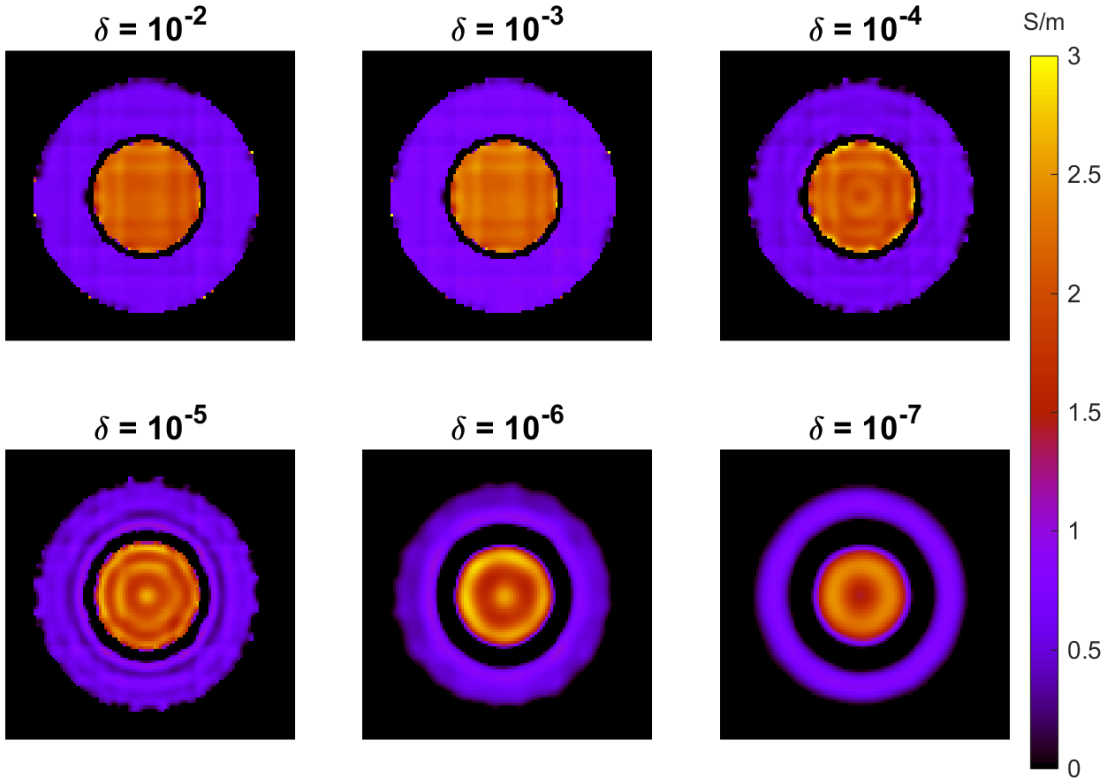

Figure 2.5: Conductivity maps reconstructed with the Inverse Laplacian method for the simulation data with varying values for the offset added to the DC coefficient. No noise was added to the simulation data. The DC offset was varied between 10^{-2} and 10^{-7}.

therefore not encouraged to be smooth.

We assess the accuracy of each reconstruction method based on the RMSE of the conductivity maps. Figure 2.7 (a) shows the effect of noise in the $\mathbf{B}_1^+$ data on the standard deviation of the reconstructed conductivity map. These standard deviation values were calculated after subtracting out the mean error for the given noise level, so they provide a more accurate description of the effective conductivity map noise, removing bias due to spatially varying conductivity. The IL method produces lower conductivity standard deviations than the restricted Gaussian filter across all input noise levels. Figures 2.7 (b-e) allow visualization of the bias associated with each reconstruction method at the lowest and highest noise levels. These are the mean

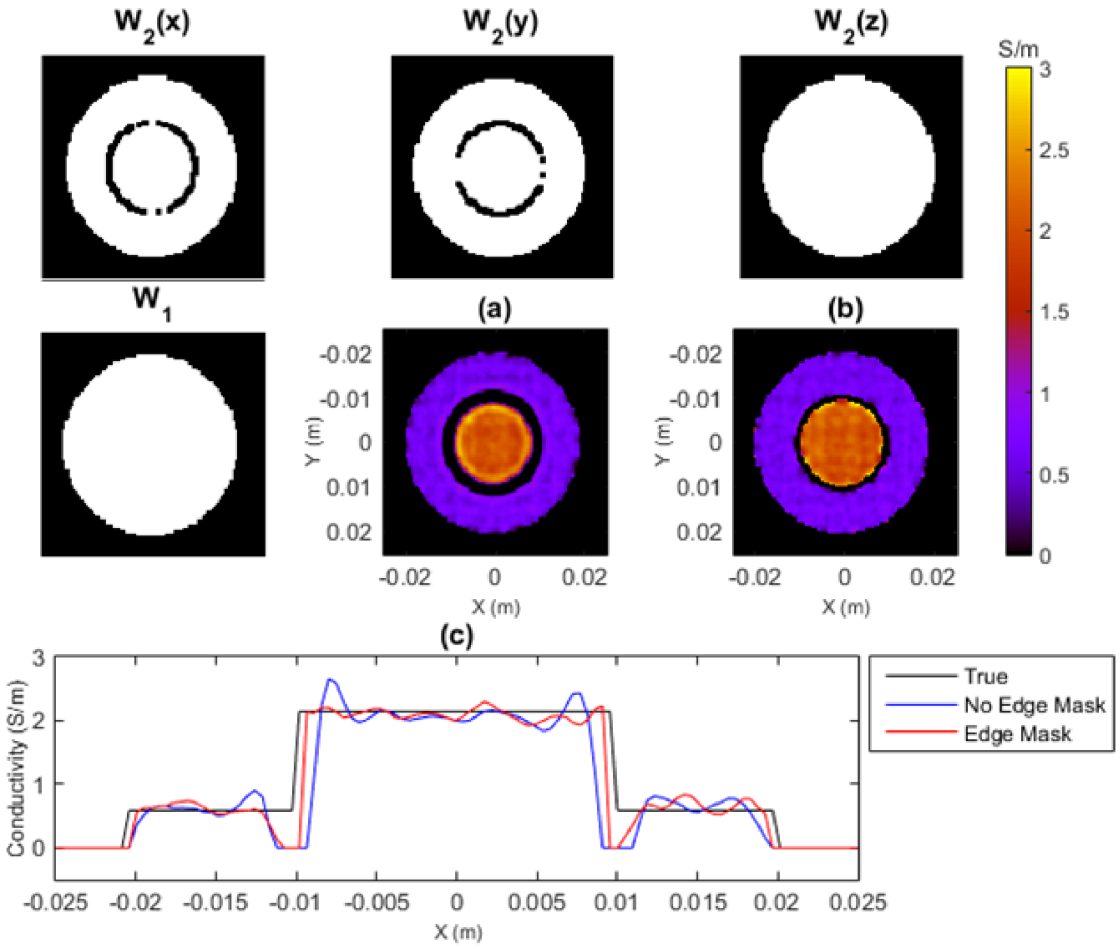

Figure 2.6: Conductivity maps reconstructed with the Inverse Laplacian method for the simulation experiments. AWGN was added to the complex data with standard deviation = 10^{-4}. Masks $\mathbf{W}_1$ and $\mathbf{W}_2$ are shown, where $\mathbf{W}_2$ provides weightings for regularization in three dimensions independently. (a) Only support mask, $\mathbf{W}_1$, used in the reconstruction. (b) Both masks, $\mathbf{W}_1$ and $\mathbf{W}_2$, used in the reconstruction. (c) Profiles through y=0.

error values for their respective input noise levels. The restricted Gaussian filter yields conductivity maps with larger error near the outer edge of the object and less uniformity at higher noise levels. Figures 2.7 (d-e) suggest that the IL method introduces a slight ringing across the object. There is a cross-hatching artifact that is visible, particularly in Figures 2.7 (b),(d), due to simulation artifacts.

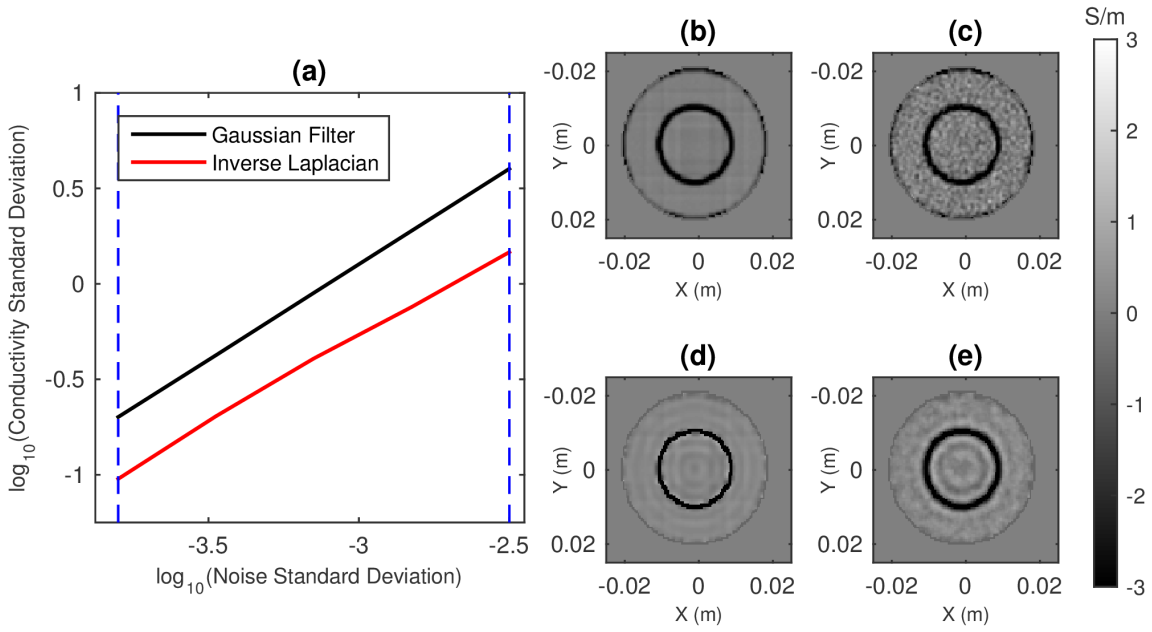

Figure 2.7: Measures of error due to noise and bias in both reconstruction methods. (a) Standard deviation of conductivity map error as a function of the standard deviation of the AWGN added to the complex simulated $\mathbf{B}_1^+$ fields. (b)-(e) Mean conductivity map error over all realizations for two noise standard deviation levels to show the bias of the Gaussian filter, (b) and (c), and Inverse Laplacian method, (d) and (e). Mean values are calculated for the lowest, (b) and (d), and highest, (c) and (e), noise levels as denoted by blue dashed lines in (a).

2.4.2 Phantom Data

Figure 2.8 shows the calculated conductivity maps for the phantom. Mean and standard deviations for each region are reported in Table 2.1. As in the simulations, the IL method produces conductivity maps with lower conductivity standard deviations. For the phantom data, the inner compartment values are largely impacted by setting negative values to zero, driving the mean and standard deviation values closer to zero. For the outer compartment, the IL method calculated conductivity values much closer to the measured value, especially after mask erosion. Adding the non-negativity constraint to the IL method resulted in a notable bias in the conductivity maps, confirmed by the values in Table 2.1.

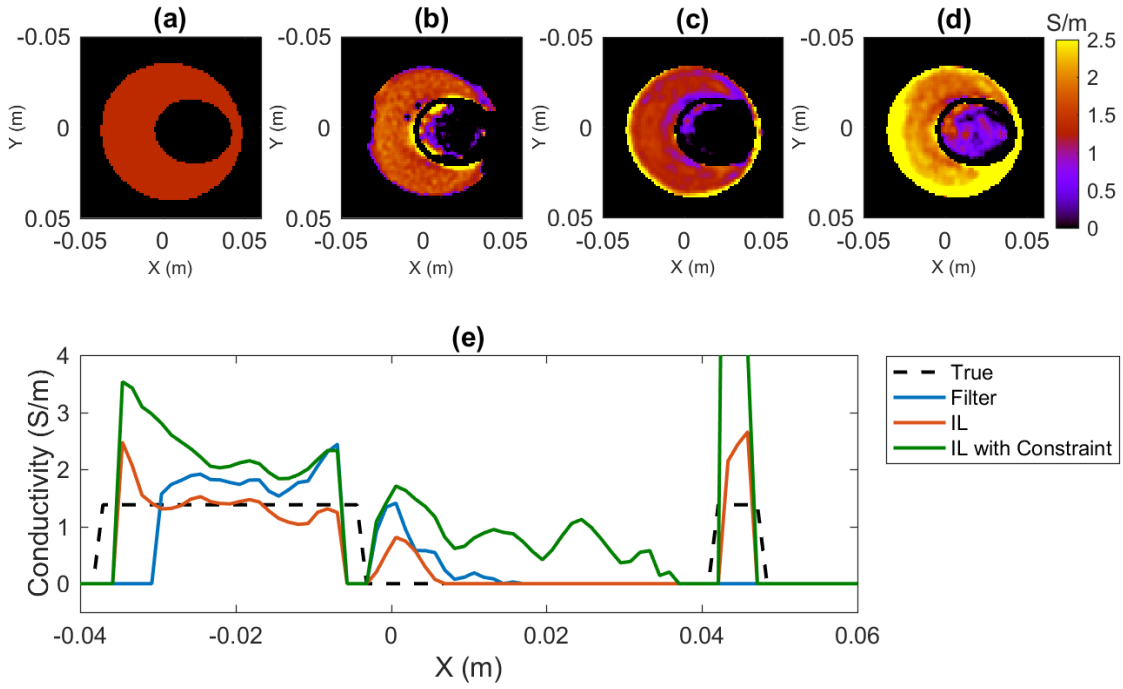

Figure 2.8: Conductivity maps for the experimental phantom. (a) True conductivity (b) Restricted Gaussian filter reconstruction (c) Inverse Laplacian reconstruction (d) Inverse Laplacian reconstruction with non-negativity constraint (e) Profiles through y=0.

2.4.3 In Vivo Data

Figure 2.9 shows the conductivity maps for a representative healthy volunteer subject calculated with the Gaussian filter and the IL method without a non-negativity constraint. Mean and standard deviations for each tissue type in all four subjects, as well as across all subjects, are reported in Table 2.2. The ventricles are well-defined as is gray matter surrounding the sulci. The IL method resulted in lower values of the standard deviation within a tissue type for most subjects, particularly the white matter values. The IL method produced higher standard deviations for the gray matter and CSF in two of the four subjects, which may be a result of a mismatch in effective resolution between the conductivity maps and the tissue segmentation.

Figure 2.10 shows a comparison of conductivity maps in a representative slice,

calculated with the Gaussian filter, the IL method, and the IL method with the non-negativity constraint. Adding the non-negativity constraint reduces the size of the zero-valued regions surrounding the ventricles, yielding more reasonable conductivity values in the CSF. Table 2.3 lists the mean and standard deviation of the conductivity for each tissue type the subject shown in Figure 2.10.

Table 2.1: Nominal and measured conductivity values for simulation and phantom experiments

		Simulation†		Phantom	
Compartment		Inner (S/m)	Outer (S/m)	Inner (S/m)	Outer (S/m)
Nominal Value		2.14	0.59	0.00	1.38
No Erosion	Filter	1.68 ± 0.88	0.47 ± 0.50	0.34 ± 0.78	1.20 ± 0.83
	IL	1.93 ± 0.83	0.65 ± 0.36	0.08 ± 0.27	1.21 ± 0.84
	non-neg. IL	1.88 ± 0.74	0.61 ± 0.38	0.77 ± 0.55	2.61 ± 0.99
Mask Erosion	Filter	2.03 ± 0.56	0.62 ± 0.49	0.10 ± 0.25	1.65 ± 0.21
	IL	2.22 ± 0.33	0.74 ± 0.29	0.01 ± 0.07	1.31 ± 0.30
	non-neg. IL	2.11 ± 0.30	0.63 ± 0.27	0.77 ± 0.41	2.17 ± 0.39

†Reconstructed with added noise standard deviation = 5×10^{-4}.

Table 2.2: Nominal and measured conductivity values for four volunteer subjects

	Tissue	Nominal Value (S/m)	Measured Value Gaussian Mean ± S.D. (S/m)	Measured Value IL Mean ± S.D. (S/m)
Subject 1	Gray Matter	0.59	2.47 ± 4.25	2.29 ± 2.30
	White Matter	0.34	0.78 ± 0.75	0.78 ± 0.69
	CSF	2.14	13.56 ± 45.76	3.08 ± 2.47
Subject 2	Gray Matter	0.59	1.40 ± 1.58	0.96 ± 1.82
	White Matter	0.34	0.81 ± 0.64	0.24 ± 0.37
	CSF	2.14	1.52 ± 2.61	2.28 ± 4.60
Subject 3	Gray Matter	0.59	1.42 ± 1.52	1.09 ± 1.33
	White Matter	0.34	0.64 ± 0.58	0.26 ± 0.37
	CSF	2.14	1.32 ± 2.10	1.13 ± 1.85
Subject 4	Gray Matter	0.59	1.22 ± 1.18	1.31 ± 1.26
	White Matter	0.34	0.58 ± 0.54	0.33 ± 0.46
	CSF	2.14	1.39 ± 2.40	1.66 ± 2.47
All Subjects	Gray Matter	0.59	1.62 ± 2.41	1.38 ± 1.70
	White Matter	0.34	0.71 ± 0.66	0.45 ± 0.52
	CSF	2.14	1.97 ± 10.22	1.65 ± 2.87

Nominal values from (100).

Table 2.3: Nominal and measured conductivity values for a representative subject

Tissue	Nominal Value (S/m)	Measured Value Gaussian Mean ± S.D. (S/m)	Measured Value IL Mean ± S.D. (S/m)	Measured Value IL + Constraint Mean ± S.D. (S/m)
Gray Matter	0.59	1.13 ± 1.26	1.48 ± 1.35	1.88 ± 1.26
White Matter	0.34	0.65 ± 0.54	0.54 ± 0.42	0.76 ± 0.41
CSF	2.14	1.13 ± 2.22	1.46 ± 2.25	2.54 ± 2.08

Nominal values from (100).

2.5 Discussion

Conductivity mapping suffers from poor SNR because conductivity is proportional to the noise-amplifying Laplacian of the phase. In addition, phase-based conductivity mapping generally assumes that the conductivity is spatially constant, an assumption that is not valid at or near tissue boundaries or in other regions of inhomogeneous conductivity. In a complex structure such as the brain, these boundary errors can greatly impact the accuracy of the results. For a simple filtering method, there exists a trade-off between SNR and edge artifacts and one must select a filter size that adequately balances the two. In our proposed Inverse Laplacian method, we have selected a regularization parameter that matches the spatial resolution properties of our method to those of a Gaussian filter for comparison. However, we have reduced the standard deviation of the conductivity values while retaining conductivity information very close to boundaries. The use of *a priori* structural information plays an important role in this reconstruction method. Furthermore, implementing a non-negativity constraint in the optimization problem eliminates the negative values associated with boundary errors with more reasonable conductivity values.

Our method differs from previously proposed inverse approaches in that it is a fully 3D formulation that can be solved as a single problem. The CSI-EPT approach (82) has only been demonstrated in 2D and the inverse approach published by Borsic et al. (84) was formulated in 3D, but computational load required subdivision of the

problem. Our calculation of the IL filter provides a manageable problem size for the inverse approach, even for 3D volumes.

One might consider framing this as an image denoising problem by replacing $\frac{\phi^+}{\omega\mu_0}$ with $\boldsymbol{\sigma}_{\boldsymbol{calculated}}$ and system matrix $\mathbf{L}$ with the identity matrix. This would likely achieve similar noise reduction as the proposed problem, but any bias and artifacts in the image would depend on how the conductivity map was calculated in the first place. As discussed in the introduction, there has been work in improving the filter and Laplacian kernels used in conductivity mapping to reduce artifacts. However, using those techniques as well as the denoising approach would result in a multi-stage conductivity mapping process. We believe it is simpler to use the proposed IL method to combine these approaches into a single problem.

An important parameter in the IL filter calculation is selecting a small DC offset, δ, so that the discrete Laplacian operator is invertible. As shown in Figure 2.5, we have selected a value from a wide range of possibilities that will minimize error due to this DC offset.

Based on Figure 2.6, the edge mask, $\mathbf{W}_2$, improves the accuracy of conductivity maps near material boundaries. Without this mask we observe a roll-off near compartment boundaries where the conductivity is not locally constant, yet the regularizer enforces a smooth transition. This effect is more pronounced in regions where conductivity variation with space is large, such as the compartment boundary in the simulations or at the boundary of CSF in the brain. These regions also provide good contrast in the MRI magnitude images, making it easy to detect the edges. Other regions of spatially varying conductivity may be more difficult to identify, but they cause smaller errors so it is not as important to capture those areas in the edge mask.

Boundary errors can have a large impact in comparing reconstruction methods. The conductivity values reported in Table 2.1 for the simulation data show that the IL method mean values changed less with the mask erosion, supporting the idea that

the IL method can better recover conductivity information near boundaries. The boundary errors in the Gaussian filter reconstruction are primarily due to applying the Laplacian operator across boundaries and are propagated by filtering. One might consider excluding these regions from the Laplacian calculation, but this would still result in inaccurate conductivity values at those spatial locations. Figure 2.3 also shows that adding the non-negativity constraint to the IL method reduces the width of the zero-valued boundary artifact.

The phantom results show that the regularization parameters translated well from simulation to phantom data, which is an encouraging result for a method that could potentially be highly dependent on parameter tuning. The phantom benefits from having a physical layer of separation between the two compartments, aiding in the detection of edges for mask $\mathbf{W}_2$. There is a conductivity spike near the compartment boundaries present in both methods, shown in Figure 2.8. The inner compartment is deionized water, so the SNR for the $\mathbf{B}_1^+$ data is lower than in the outer compartment. Coupled with the lower conductivity, this makes it more challenging to tease out the underlying phase curvature from the noisy data. While much of the inner compartment was set to zero in post-processing, the IL algorithm produced fewer high conductivity values in the inner compartment. When the non-negativity constraint was included in the IL method, the conductivity results were biased. This constrained version of the IL method does not perform well in non-conductive materials, which shouldn't be an issue in vivo. The bias in the conductive region, however, may be an issue with algorithm accuracy. We implemented the constraint using the conjugate gradient method, but this may ruin the conjugacy of the search directions. We implemented the constraint using gradient descent on one of the human subject data sets. This appeared to converge to the same solution as the conjugate gradient method, albeit at a much slower rate. Further studies should focus on alternative methods for implementing the non-negativity constraint to ensure reliable solutions.

For the human brain experiments, we present representative conductivity maps in Figure 2.9. The ventricles are well-defined along with many of the sulci. Similar to previous results, the Gaussian filter produced higher variation in conductivity values as compared to the IL method. A combination of filters on the phase data as well as the conductivity maps would be necessary to achieve better results, but when cascading filters one also risks loss of spatial resolution. The mean and standard deviation of each tissue type for all four subjects are presented in Table 2.2. Mean tissue conductivity varied between subjects, but were generally close to reported values. Marked differences between mean tissue values for the Gaussian filter versus the IL method might be explained by large positive values near edges. Definition between tissue types might be improved with high resolution $\mathbf{B}_1^+$ maps. Since our proposed method provides reduced noise amplification while maintaining spatial resolution properties, we can expect the IL method would be able to reconstruct accurate conductivity maps from high resolution, lower SNR $\mathbf{B}_1^+$ data. Visual inspection of Figure 2.10 indicates the non-negativity constraint further improved the IL method conductivity maps by reducing the size of the zero-valued regions and reducing the standard deviation within tissue types. This is supported by the quantitative results presented in Table 2.3, which shows that adding the non-negativity constraint generally reduces the standard deviation within a tissue type. Additionally, the mean values increase by adding the constraint, but this is likely due to replacing zero-valued pixels with non-zero values.

2.6 Conclusions

We have developed a novel 3D regularized, model-based algorithm for phase-based conductivity mapping that uses *a priori* structural information to increase the accuracy of the maps. The Inverse Laplacian method exhibits less noise amplification and better edge responses than filtering methods and has proven successful in simulation,

phantom, and the human brain. Furthermore, including a non-negativity constraint in the IL method yields conductivity maps that, in vivo, appear to be more accurate due to the reduction of zero-valued regions. The accuracy of the non-zero values is unknown.

Accurate conductivity maps are essential for clinical or safety applications. To improve the accuracy of our method, we plan to investigate the incorporation of non-constant electrical properties into the system model. This would be equivalent to deriving a system model from the Helmholtz equation as opposed to the homogeneous version. We believe this would result in more accurate values in regions with spatially varying electrical properties, specifically at the locations we have excluded from regularization in the current methodology.

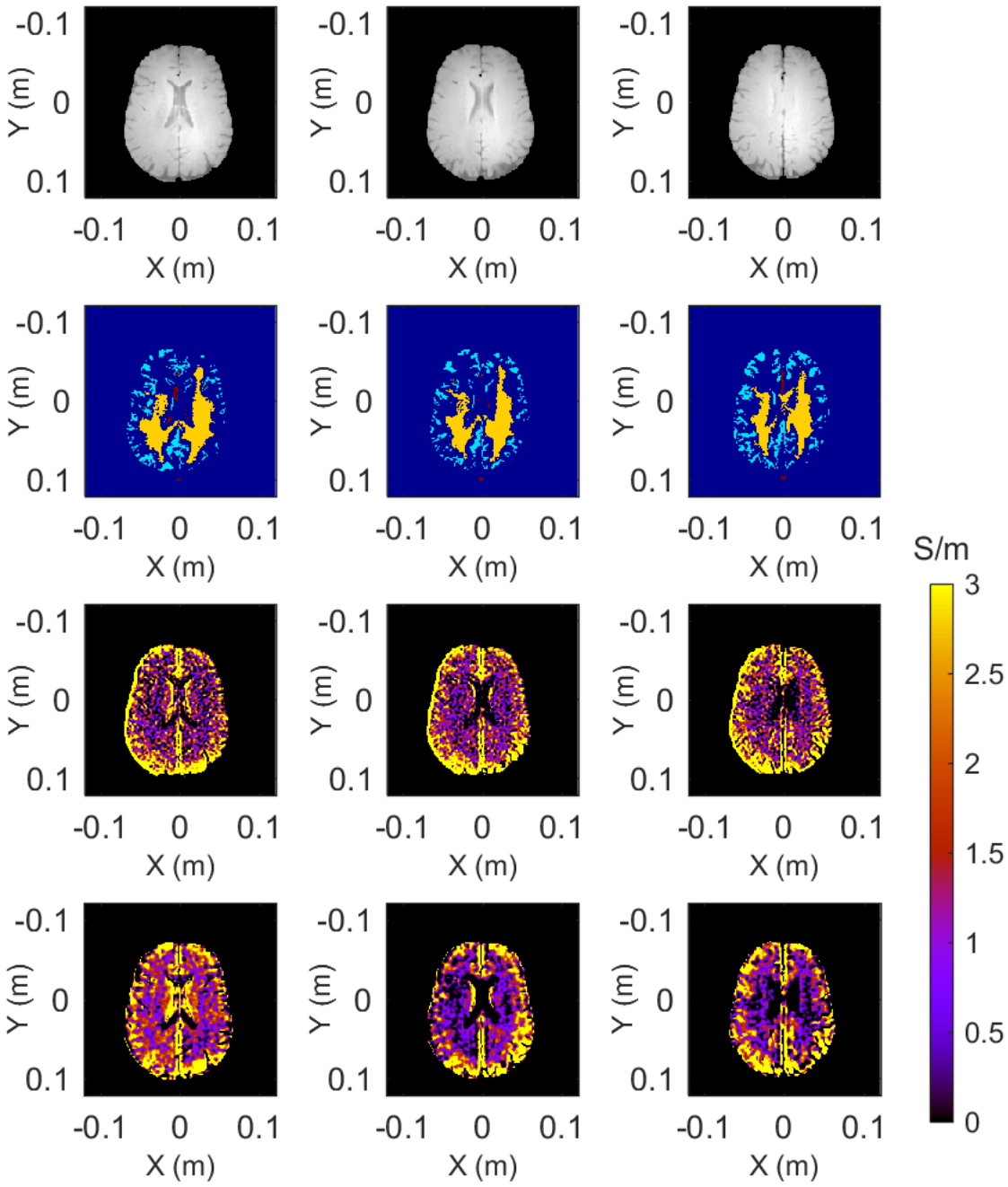

Figure 2.9: Spin Echo magnitude image (Row 1); tissue segmentation (Row 2) showing CSF [red], white matter [yellow], and gray matter [blue]; and conductivity maps reconstructed using the restricted Gaussian filter (Row 3) and the Inverse Laplacian method (Row 4) for a representative healthy volunteer subject. Each column corresponds to a different slice in the acquired volume.

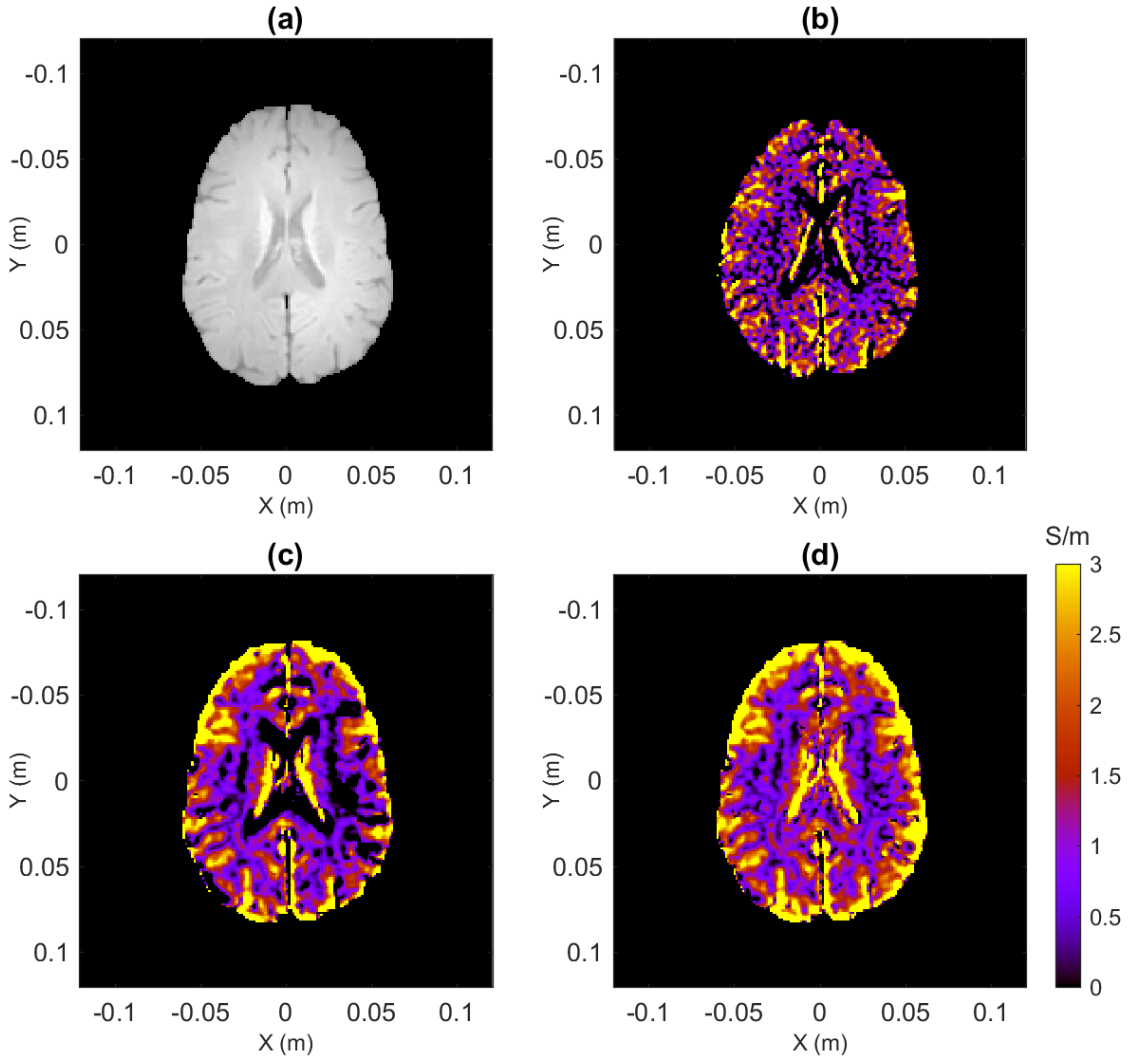

Figure 2.10: Conductivity maps for a representative slice from one subject. (a) Anatomical Image (b) Restricted Gaussian filter reconstruction (c) Inverse Laplacian reconstruction (d) Inverse Laplacian reconstruction with non-negativity constraint

CHAPTER III

Reference-less Method for Combining Multi-Coil Receiver Data for MR-EPT

3.1 Introduction

Electrical conductivity is proportional to the Laplacian of the RF transmit phase. The Laplacian operator drastically amplifies any noise in the acquired field map, so acquiring data with high SNR is essential.

SNR can be improved by using multi-channel receive coils. Each receive coil is highly sensitive in the near field, so with adequate coil coverage and data combination the overall SNR of the combined image is increased. Vegh et al. (101) stated that averaging signal phase in areas of sufficiently high SNR is appropriate because the phase distribution is approximately Gaussian. Therefore, the idea of combining channels based on the local sensitivity properties in each coil is logical to avoid averaging coils with low SNR in certain spatial regions. Combination of complex-valued data for MR-EPT is further complicated by the additional phase components present in individual coil data, which are not accounted for in averaging. Furthermore, open-ended phase wraps, or open-ended fringe lines, exist in phase maps in regions of very low signal. These signal null points occur where the flux lines in the coil sensitivity are parallel to the coil plane. Open-ended phase wraps cause errors in phase unwrapping

algorithms because, as shown in Figure 3.1, there is not an enclosed region that can be described by a 2π jump.

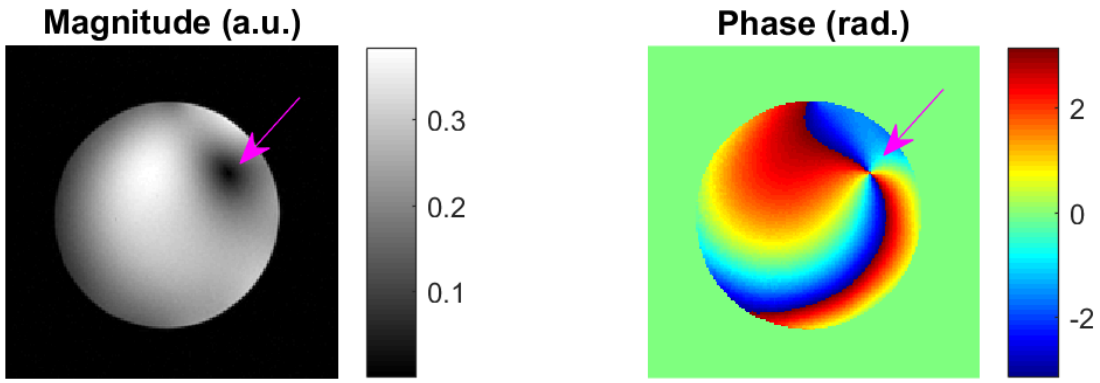

Figure 3.1: Example of an open-ended phase wrap in one channel of a multi-channel array. Magnitude image (Left) and Phase image (Right) with magenta arrows indicating the location of the artifact.

The transceive phase assumption, which states that the transmit phase is approximately half of the measured transceive phase, is necessary for MR-EPT because it is not possible to separate the transmit and receive phase. The transceive phase assumption is valid for a coil operating in quadrature, but not necessarily for multi-channel receivers. Therefore, we aim to develop a combination method to mimic the behavior of a quadrature coil. As discussed in Chapter I, the transceive phase assumption is not required for phase-based conductivity mapping due to the linearity of the approximation. We will also discuss the application of coil combination methods for phase-based conductivity mapping, which, in theory, does not require a quadrature coil.

Roemer et al. (102) described an optimal coil combination for phased array coils using complex-valued coil sensitivity maps. Typically an extra scan is required to measure these sensitivity maps, and additional smoothing is necessary to produce high SNR combined images. Walsh et al. (103) proposed a combination method based on the spatial matched filter, which does not require sensitivity map measurements.

In (103), Walsh suggests applying this method in smaller regions to reduce noise in dark areas of the image. This is feasible for magnitude images, but the resultant phase images are not guaranteed to be smooth. By applying alignment techniques provided by Zhang et al. (104), which ensure smooth combined phase images, complex data can be combined on a pixel-wise basis for optimal SNR across the image while maintaining smooth phase images (105). Lee et al. (106) have recently proposed a coil combination method formulated as a magnitude least squares problem, which was intended specifically for phase-based conductivity mapping.

In this work we present a method, which we refer to as Local Compression with Background Phase Correction (LC-BC), for combining complex data from multi-channel receivers without a reference scan or a reference coil. We use the methods for aligning combination weight vectors described in (105), with an additional background phase correction step to reduce phase bias due to high-signal coils. We show that by estimating common phase components from acquired images and combining data pixel-wise, one can exploit the full benefits of the spatially varying coil sensitivities for a high SNR image with minimal phase bias. We compare this method to Roemer's optimal combination (102) and Walsh's adaptive combination (103). We also provide results without the background correction to show its utility. Each method is evaluated in phantoms and a human subject.

The goal of this work is to enable the use of multi-channel receiver coils for MR-EPT to improve conductivity map SNR while maintaining the accuracy of a quadrature coil. We focus on applying this method to MR-EPT because, theoretically, the phase-based conductivity approximation does not require a quadrature coil. However, we discuss the proposed method's application to phase-based conductivity mapping as a means of increasing conductivity map SNR. [1]

[1]Parts of this chapter have been submitted as: K.M. Ropella and D.C. Noll, Data-driven background phase correction and combination to improve the accuracy of MR-EPT with multi-channel receivers, In proceedings of the 25th ISMRM, 2017:3646.
K.M. Ropella and D.C. Noll, Data Driven Coil Combination Method for Phase-Based Conductivity

3.2 Theory

MR-EPT assumes that the data is acquired using a quadrature coil. This work focuses on combining multi-channel data to determine $\mathbf{B}^+$ to mimic that of a quadrature birdcage coil, with an emphasis on the phase fidelity. The following methods are applied to unprocessed image data, $\mathbf{C}$, from a receiver array with N coils and $P = n_x \times n_y \times n_z$ voxels.

The components of the phase data acquired by coil n, ϕ_n, can be divided into those that are coil-specific and those that are coil independent:

$$\phi_n = \phi_{n,\text{coil}} + \phi_{common}. \quad [3.1]$$

Contributions to the coil-specific component, $\phi_{n,\text{coil}}$, may be due to the receive phase of the coil and the constant offset between coils. The common phase component, ϕ_{common}, may have contributions from the transmit phase, object phase, field inhomogeneity, and eddy currents. In MR-EPT we are interested in the common transmit RF phase and object phase, so it is desirable to minimize phase contributions from other sources. The spin echo sequence used to acquire MR-EPT data accounts for most other common phase components, but the coil-specific phase component must be measured or estimated in some way to minimize bias.

3.2.1 Optimal Combination

The optimal combination (OC) of multi-channel data , $\mathbf{x}_\text{O}(\mathbf{r})$, is (102):

$$\mathbf{x}_\text{O}(\mathbf{r}) = \lambda(\boldsymbol{r})\ \text{C}(\mathbf{r})^H\ \mathbf{R}_n^{-1}\ \mathbf{S}(\mathbf{r}) \quad [3.2]$$

Mapping, submitted to Magnetic Resonance in Medicine.

where the individual channel data at a single spatial location $\mathrm{C}(\mathbf{r})$ has size $N \times 1$, $\mathbf{R}_n$ is the noise correlation matrix for the coil array with size $N \times N$, and $\mathrm{S}(\mathbf{r})$ is the complex-valued coil sensitivity information at a single spatial location with size $N \times 1$. The noise correlation matrix describes coupling between individual coils in a receiver array. The conjugate transpose is represented as $(\cdot)^H$. The parameter $\lambda(\boldsymbol{r})$ affects scaling in the final image and, with spatially varying values, can be used to reconstruct uniform magnitude or uniform noise images. In this work the parameter λ is spatially constant, with its absolute value affecting the scaling of the final image but not the relative weights used to combine the individual channels. Adaptations involving a non-constant λ can be found in (102).

This combination procedure requires measurement of coil sensitivity maps, $\mathbf{S}$, and the noise correlation matrix in addition to the experimental data of interest. It can be reasonably assumed that noise correlation matrices are relatively constant across subjects and therefore only need to be measured once. Sensitivity maps, on the other hand, should be measured for every object or subject. This increases the scan time for an experiment and is susceptible to motion. Sensitivity maps account for the undesirable coil-specific phase components for MR-EPT.

3.2.2 Adaptive Combination

To eliminate the need to measure sensitivity maps, one can treat both signal and noise as stochastic processes, $s(\boldsymbol{r})$ and $n(\boldsymbol{r})$ with correlation matrices $\mathbf{R}_s$ and $\mathbf{R}_n$, respectively. Walsh et al. (103) describe the adaptive combination (AC) process as

$$\mathbf{x}_{\mathrm{A}} = \boldsymbol{m}_{\mathrm{A}}^H \, \mathbf{C}. \qquad [3.3]$$

The vector of combination weights for the entire image, $\boldsymbol{m}_{\mathrm{A}}$, is the eigenvector corresponding to the largest eigenvalue of $\mathbf{R} = \mathbf{R}_n^{-1} \, \mathbf{R}_s$. The size of $\boldsymbol{m}_{\mathrm{A}}$ is $N \times 1$.

We follow (103) to calculate the correlation matrices. The signal correlation matrix

is the correlation between coils, calculated from image data at all spatial locations for each coil:

$$\mathbf{R}_{s,jk} = \mathrm{E}[C_j(\boldsymbol{r})C_k^*(\boldsymbol{r})] \quad [3.4]$$

where $j = 1, ..., N;\ k = 1, ..., N$. Only signal-producing voxels are used in this calculation.

The noise correlation is calculated between coils over time:

$$\mathbf{R}_{n,ij} = \mathrm{E}[n_j(t)n_k^*(t)] \quad [3.5]$$

where $n(t)$ is the noise signal in the receiver channels. One can also approximate the noise correlation matrix with the identity matrix, as in (103).

3.2.3 Local Compression

The AC method calculates combination weights to be used at every spatial location of the object. To account for spatially varying coil sensitivities, as in the OC method, we aim to calculate the combination weights voxel-wise. We modify the AC method to calculate spatially varying vectors of combination weights and use Zhang's alignment procedure (104) to ensure smooth phase. First, coil combination weight vectors are calculated for each pixel using the AC method in a square neighborhood of width w. Next each vector, $\boldsymbol{m}_i$, is aligned with its neighbor, $\boldsymbol{m}_{i-1}$, by the rotation matrix $\boldsymbol{\rho}$, which minimizes the Euclidean distance between the vectors. We use the following procedure:

$$\mathbf{P} = \mathbf{m}_i^H \mathbf{m}_{i-1} \quad [3.6]$$

$$\mathbf{P} = \mathbf{U}_\mathrm{P} \Sigma_\mathrm{P} \mathbf{V}_\mathrm{P}^H \quad [3.7]$$

$$\boldsymbol{\rho} = \mathbf{V}_\mathrm{P} \mathbf{U}_\mathrm{P}^H \quad [3.8]$$

$$\tilde{\boldsymbol{m}}_i = \boldsymbol{m}_i \boldsymbol{\rho}^H. \quad [3.9]$$

The Local Compression (LC) vector of combination weights is

$$\boldsymbol{m}_{\mathrm{L}}(\boldsymbol{r}) = \tilde{\boldsymbol{m}}_i \qquad [3.10]$$

and the combined image is

$$\mathrm{x}_{\mathrm{L}}(\boldsymbol{r}) = \boldsymbol{m}_{\mathrm{L}}^{H}(\boldsymbol{r})\, C(\boldsymbol{r}). \qquad [3.11]$$

We use a region-growing algorithm to align the filter vectors in an outwardly-growing fashion. Because we calculate a different filter vector for each pixel and one can only minimize the Euclidean distance between the vector of interest and one neighbor, two-dimensional and three-dimensional alignment are performed in a similar manner.

3.2.4 Local Compression with Background Phase Correction

The LC method is susceptible to bias in the phase images from individual coil phase profiles. To minimize the contributions due to individual coil phases, we propose a data-driven phase correction step to be applied before the LC procedure.

Given the raw multi-coil image data, $\mathbf{C}$, applying a low pass filter to each coil of data yields $\tilde{\mathbf{C}} = \mathbf{C} * H_{lpf}$. First we use an approach inspired by Cao et al. (107) for estimating the common object phase for all channels from the product of the

smoothed individual coil data:

$$\begin{aligned}\Theta &= arg\left(\frac{\prod\limits_{k\in K}\tilde{\mathbf{C}}_k}{\prod\limits_{k\in K}|\tilde{\mathbf{C}}_k|}\right)\\ &= arg\left(\frac{\prod\limits_{k}|\tilde{\mathbf{C}}_k|\exp\Big(i\big(\sum\limits_{k}\phi_{k,coil}+K\phi_{common}\big)\Big)}{\prod\limits_{k}|\tilde{\mathbf{C}}_k|}\right)\\ &= \sum_{k}\phi_{k,coil}+K\phi_{common}\end{aligned} \quad [3.12]$$

where only K of the N coils are used in the approximation. This is the subset of coils that do not contain open-ended phase wraps. The coil-specific phase contribution from each coil are assumed to not be highly correlated due to the physical distribution of the individual coils. Thus, the common phase term is the dominant term in Θ. Unwrapping Θ and dividing by K yields negligible phase contributions due to individual coils, giving an approximation of the common object phase. Using this approximation of the common phase we calculate the image data with only the coil-specific phase for all N coils:

$$\mathbf{C}_{n,\text{coil}} = \frac{\tilde{\mathbf{C}}_n}{\exp\big(i\Theta/K\big)} \quad [3.13]$$

Finally, we estimate the image data with only the common phase for all N coils by subtracting this individual coil phase from the unfiltered data:

$$\mathbf{C}_{n,common} = \frac{\mathbf{C}_n}{\mathbf{C}_{n,\text{coil}}} = |\mathbf{C}_n|\exp(i\phi_{common}) \quad [3.14]$$

This new, phase-corrected multi-channel data contains the original magnitude information and can be used as an input to the local compression method. It is important to note that the low pass filtered data is only used to estimate the coil-specific phase contributions and the filtered data is not used in the compression

step. The goal is to estimate a smooth coil-specific phase as to not change the noise properties in the original data. This is analogous to estimating smooth sensitivity maps for OC.

3.2.5 Phase-Based Conductivity Mapping with Multi-channel Receivers

As mentioned in Chapter I, the linearity of the phase-based conductivity approximation supersedes the transceive phase assumption associated with a quadrature coil. Multi-channel receivers are not operating in quadrature, so the phase-based conductivity approximation is a logical choice for that situation. The linearity of the approximation assumes that the transceive phase contains all components of the transmit and receive phase quantities. Therefore, averaging the phase-based conductivity for each of the individual receiver channels will yield the correct conductivity measurement, as all transmit and receive phase quantities have been accounted for. In the interest of improving SNR, we compare the averaged conductivity maps to the previously discussed combination methods to phase data only for phase-based conductivity mapping. In addition, we implement the method proposed by Lee et al. (106) for phase-based conductivity mapping, which we will refer to as the Magnitude Least Squares (MLS) Combination method.

The MLS method can also be written in terms of a vector of combination weights:

$$\mathbf{x}_M = \boldsymbol{m}_M^T \, \mathbf{C}. \qquad [3.15]$$

We follow the approach in (106) to calculate $\boldsymbol{m}_M$:

$$\boldsymbol{m}_M = \arg\min_{\boldsymbol{m}} \left|\left|\left|\boldsymbol{m}^T\mathbf{C}\right| - 1\right|\right|_2^2 + \beta\left|\boldsymbol{m}\right|^2 \qquad [3.16]$$

where β is the regularization parameter, determining the trade-off between magnitude uniformity and SNR. The vector $\boldsymbol{m}_M$ is calculated using a subset of the image data

with approximately uniform magnitude, identified by thresholding the magnitude of the acquired image data. We solved the optimization problem using the variable exchange method suggested in (106). This approach is common in RF pulse design problems, so we followed the variable exchange methods in (108) and (109).

3.3 Methods

3.3.1 Image Acquisition

All experiments were performed on a GE Discovery MR750 3.0T MRI scanner (GE Healthcare, Waukesha, WI). Human experiments were approved by the Institutional Review Board at the University of Michigan. Two phantoms and one healthy volunteer were scanned. The first phantom was a spherical gel phantom (diameter = 17 cm) with a conductivity of 0.586 S/m. The second was a cylindrical liquid phantom (diameter = 9 cm, length = 16 cm) with a conductivity of 2.11 S/m, positioned parallel to the bore but very close to the inner edge of the coil. The measured conductivity value for the spherical phantom, which is sealed, is the average value over the volume measured using a quadrature birdcage coil. The conductivity for the cylindrical phantom was measured using a dielectric probe.

The magnitude and phase images for MR-EPT were acquired separately. Two-dimensional fast gradient echo scans with flip angles of 30 and 60 degrees were acquired to calculate the magnitude of $\mathbf{B}_1^+$ using the double angle method. The acquisition parameters were TE/TR = 3.1/150 ms, FOV = 24 × 24 × 6 cm, with $1.25 \times 1.25 \times 3$ mm^3 voxels. Two averages were used for a scan time of 59 seconds. Two two-dimensional spin echo images with opposite slice-select gradient polarities were acquired, averaged, and divided by two to calculate the phase of $\mathbf{B}_1^+$. For the phantoms, the sequence parameters were TE/TR = 11/1200 ms, FOV = $24 \times 24 \times 6$ cm, with $1.25 \times 1.25 \times 3$ mm^3 voxels. Two averages were acquired with a bandwidth

of 15.63 kHz. The sequence parameters for the human brain images were identical with the exception of TE/TR = 18/1200 ms and FOV = 24 × 24 × 2.1 cm. Scan times were 7 minutes and 46 seconds. All four data sets were acquired using both the body transmit/receive coil and the 32-channel receiver array.

The noise correlation matrix for the 32-channel coil was determined by calculating the correlation coefficients between noise signals on each channel while the coil was loaded with the spherical phantom.

3.3.2 Phase Processing

The 32-channel array data for the phantoms and the volunteer subject were combined using the OC, AC, LC, and LC-BC methods described above. The phase alone was also combined using the MLS method. All phase unwrapping was performed using a quality-guided approach (110).

For the OC method, sensitivity maps for the 32-channel array coil were calculated dividing the individual coil data by the body coil data and using a regularized method (111). The AC method was implemented with a constant λ value of 1. The MLS method used a regularization parameter of $\beta = 1000$. In the LC method, a window width of 11 pixels was used to calculate the combination weight vectors.

The low pass filter used in the LC-BC method was a Gaussian filter with a filter parameter of 3 pixels and a width of 13 pixels. The filter parameter is the standard deviation of the Gaussian distribution. To show the influence of this filter on the resultant conductivity, we varied the filter parameter from 0.5 to 7.

The subset of K coils for the background phase correction was selected based on the variance of the phase partial derivatives, which is the quality calculation in the quality-guided phase unwrapping approach in (110). If the maximum variance for a channel in a given slice exceeded a pre-set threshold, the channel contained an open-ended phase wrap. The mean value of K per slice is reported in the Results section.

As an example, we performed the LC-BC combination with all 32 coils, regardless of whether they had open-ended phase wraps. Dividing K by Θ in Equation 3.13 assumes that the coil-specific components are not highly correlated. As a test of worst-case scenarios, we select K from only the bottom hemisphere of the coil and only those coils without open-ended phase wraps.

The four data sets (two gradient echo for magnitude and two spin echo for phase calculations) were combined separately before calculating the full complex-valued $\mathbf{B}_1^+$ field. The two combined gradient echo images were used in the double angle method to calculate the magnitude of $\mathbf{B}_1^+$. The two combined spin echo images were averaged to calculate the phase of $\mathbf{B}_1^+$.

3.3.3 Phase Standard Deviation Calculations

To the leading order, conductivity primarily depends on the phase of the $\mathbf{B}_1^+$ field (63, 66), so this analysis will focus on the phase of the combined data.

To assess relative SNR levels between the five methods, the standard deviation of the phase images was calculated in the image domain. The standard deviation was calculated for each pixel using its 7x7 pixel neighborhood. In each neighborhood, a second order polynomial surface was fit to the data and the standard deviation of the residuals was taken to be the standard deviation of the phase data. The standard deviation was also calculated for a single channel of the receiver array for comparison in the phase-based conductivity analysis.

3.3.4 Conductivity Calculations

The combined data was used for conductivity mapping via MR-EPT in the phantoms and human subject. Conductivity was calculated as the imaginary part of [1.3], using the discrete Laplacian operator, and then applying a Gaussian filter with standard deviation = 2 pixels and width = 9 pixels.

The uniformity of the phantom conductivity images was calculated based on the UN2 method in (112), which quantifies how close the conductivity values are to the mean value. Larger UN values denote a more uniform image.

3.3.5 Phase-Based Conductivity Mapping

The conductivity calculations in the previous section were repeated in the phantoms and human subject using the phase-based conductivity calculation in 1.8. The same spatial filter was applied afterwards. Additionally, two conductivity averaging techniques were used to compare methods that combine the phase data to methods that combine conductivity maps. The first method, coil averaging, divides the average spin echo phase by two, calculates the phase-based conductivity in each of the 32 channels, and then calculates a weighted average of the channels based on the spin echo image magnitude. After combining the 32 conductivity maps, the same filter as above was applied - a Gaussian filter with standard deviation = 2 pixels and width = 9 pixels. The second method, selective coil averaging, was nearly identical to the first, but involved cropping out regions near open-ended phase wraps in the individual coil images after calculating conductivity but prior to the weighted average. These open-ended phase wraps were identified using the same quality metric as in the background correction process, and the excluded regions were all the pixels within 11 pixels of the phase wrap. Finally, the mean and standard deviation of the resultant conductivity maps were calculated.

3.4 Results

The resultant images from all five combination methods in a central slice of each of the two phantoms are shown in Figure 3.2. We have combined the methods used for MR-EPT and the phase-based combination into one figure because the same set of combined data is used for both. For the LC-BC method, $K_{mean} = 18.1$ and 28.1 coils

for the spherical and cylindrical phantoms, respectively. The OC method is used as a basis of comparison for the other phase images. In the spherical phantom, AC and LC show the largest difference in phase from OC. Of particular concern is the open-ended phase wrap in the AC result. The LC-BC method shows lower error, which can be described by lower order polynomials than the others. In the cylindrical phantom the phase difference is much lower. There is a dominant linear phase difference between OC and the LC-BC, which does not affect conductivity calculations, but the AC and LC methods have higher order differences. The MLS data also has a linear phase difference with respect to OC, with some additional artifact in the spherical phantom near the outer edge.

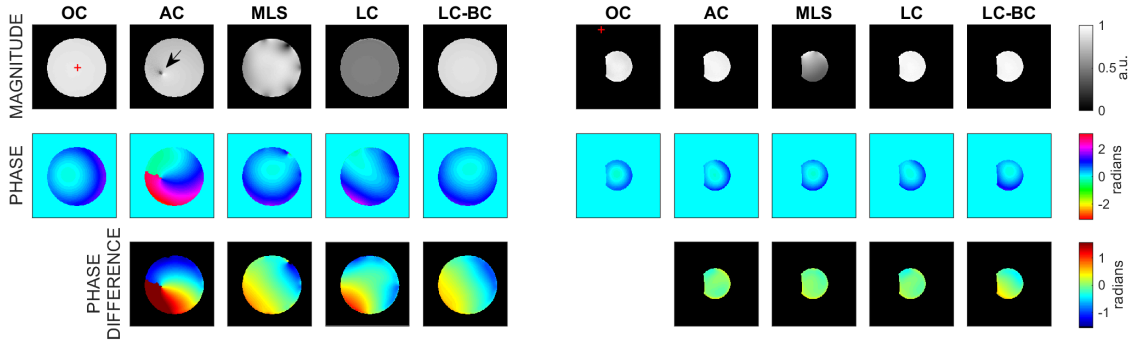

Figure 3.2: Coil-combined image data for the spherical phantom (left) and cylindrical phantom (right). Magnitude (top row) and phase (middle row) for combined images using Optimal Combination (OC), Adaptive Combination (AC), Magnitude Least Squares (MLS), Local Compression (LC), and Local Compression with Background Phase Correction (LC-BC). The bottom row shows the difference in the combined phase between each combination method and Optimal Combination. Red crosses denote the location of the center of the coil. Arrow shows the location of an open-ended phase wrap.

Figure 3.3 shows the standard deviation of the combined phase images for both phantoms, as well as for the phase from a single coil of the receiver array. Note there is an order of magnitude increase in the single channel standard deviation image. OC, LC, and LC-BC methods show higher variances in the center of the image due

to low coil sensitivities in that region. The LC variance levels are very similar to the OC method, with the LC-BC method slightly higher. The MLS has higher standard deviation than those methods in the spherical phantom, but more uniform across the slice. The MLS method yields values very close to those calculated using a quadrature birdcage coil. AC has high variance near the left side of the object due to averaging low signal regions with global coil combination weights. The high variance ring on the OC figure for the cylindrical phantom is likely due to errors in calculating sensitivity maps near the object edge.

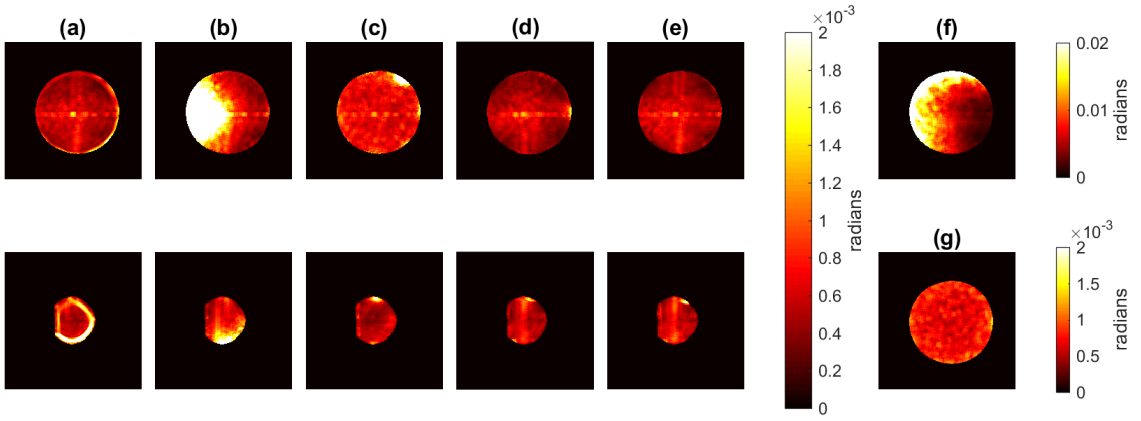

Figure 3.3: Phase standard deviation maps for combined images using (a) Optimal Combination, (b) Adaptive Combination, (c) Magnitude Least Squares, (d) Local Compression, and (e) Local Compression with Background Phase Correction. Representative slices are shown for the spherical phantom (top) and the cylindrical phantom (bottom). Figure (f) shows the phase standard deviation for a single channel of the receiver array.Figure (g) shows the phase standard deviation for the quadrature birdcage coil.

Resultant conductivity maps using MR-EPT on the coil-combined data from the two phantoms are presented in Figure 3.4, with column (e) showing the conductivity calculated from quadrature birdcage data. The non-uniformity in the conductivity maps reflect bias in the combined phase. The uniformity was quantified and is reported below each image along with the average conductivity value for the slice. The regions used for those calculations are shown in Figure 3.5.

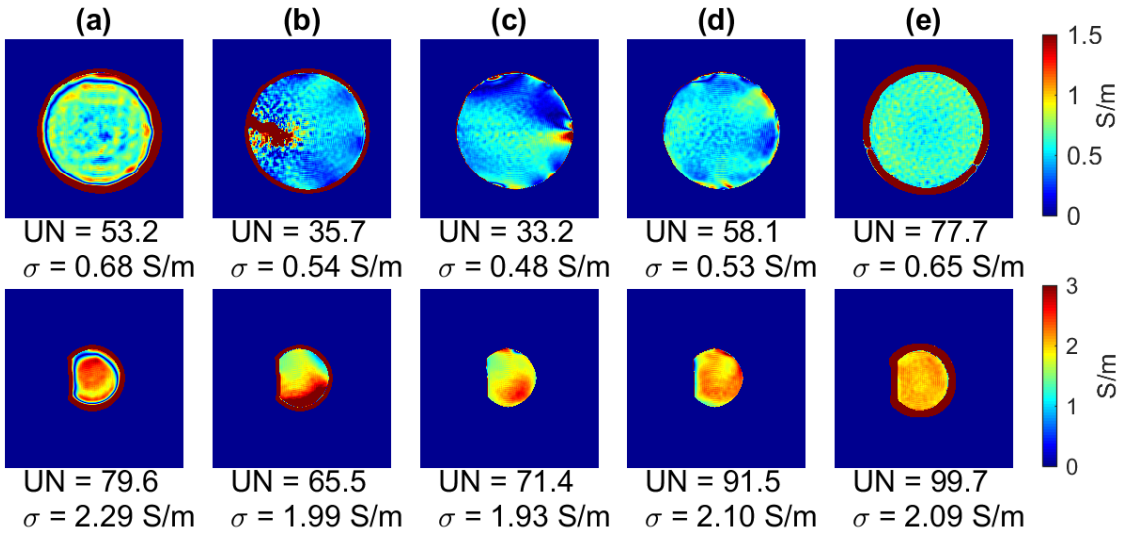

Figure 3.4: Conductivity maps calculated with MR-EPT for the spherical phantom (top) and the cylindrical phantom (bottom). Results from multi-coil phase data combined using (a) Optimal Combination, (b) Adaptive Combination, (c) Local Compression, and (d) Local Compression with Background Phase Correction. (e) Quadrature Birdcage Coil results. Uniformity (UN) and average conductivity (σ) for each image is listed. The regions used for those calculations are shown in Figure 3.5.

Conductivity maps calculated using the phase-based approximation are shown in Figure 3.6, with column (f) showing the conductivity calculated from quadrature birdcage data. The uniformity and the average conductivity value for the slice are provided below each image.

Conductivity maps from a human subject are shown in Figure 3.7 and 3.8, calculated using MR-EPT and the phase-based approximation, respectively. For the LC-BC method, $K_{mean} = 20.5$ coils across all slices. The phase bias in the AC and LC methods are reflected with higher and lower conductivity values, indicated by red and green arrows.

Figure 3.9 shows the effect of the filter size used to smooth the data in the background correction step on conductivity maps.

Figure 3.10 shows the effect of including open-ended phase wraps in the LC-BC

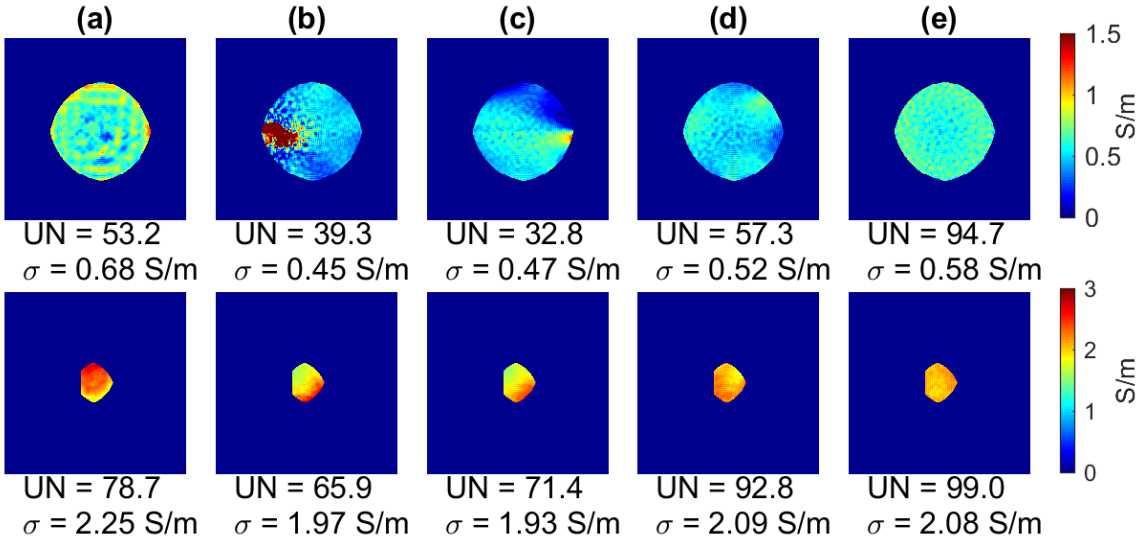

Figure 3.5: Regions of the conductivity maps from Figure 3.4 used in the calculations of mean conductivity and uniformity. Shown are the spherical phantom (top) and the cylindrical phantom (bottom). Results from multi-coil data combined using (a) Optimal Combination, (b) Adaptive Combination, (c) Local Compression, and (d) Local Compression with Background Phase Correction. (e) Quadrature Birdcage Coil results. Uniformity (UN) and average conductivity (σ) for each image is listed.

method and Figure 3.11 shows the effect of selecting K from different physical sections of the coil. In Figure 3.11, the left column shows the results presented in the main text, where coils are spatially distributed around the entire phantom. The average value of K over all the slices was 18.1 coils. The right column shows results using coils that lie only on the bottom hemisphere of the coil, giving suboptimal separation of the coil-specific components. The average value of K for the lower hemisphere was 7.5 coils.

Figure 3.12 shows the comparison of the conductivity maps and standard deviation values for three phase-based calculations. Errors due to open-ended phase wraps are apparent in the coil averaging conductivity map. The LC-BC methods yields a mean closer to that of the birdcage coil as well as a lower standard deviation than the other two methods.

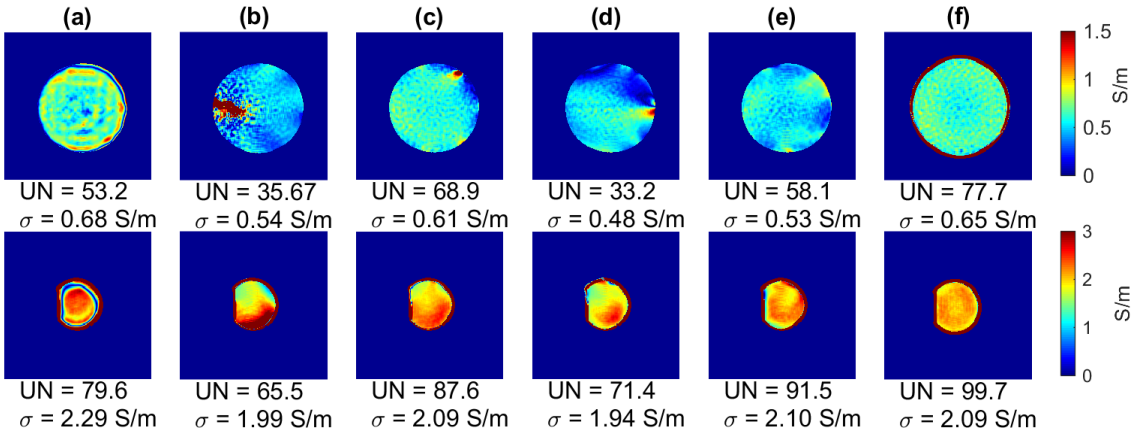

Figure 3.6: Phase-based conductivity maps for the spherical phantom (top) and the cylindrical phantom (bottom). Results from multi-coil phase data combined using (a) Optimal Combination, (b) Adaptive Combination, (c) Magnitude Least Squares, (d) Local Compression, and (e) Local Compression with Background Phase Correction. (e) Quadrature Birdcage Coil results. Uniformity (UN) and average conductivity (σ) for each image is listed.

3.5 Discussion and Conclusions

MR-EPT involves calculating the Laplacian of the transmit RF field, which amplifies noise in the acquired data. Beginning with the highest SNR possible is desirable for these calculations. SNR can easily be improved using multi-coil receivers, provided the data can be accurately combined. Here we propose a reference-less approach to coil combination to eliminate artifact from motion between the acquisition of sensitivity maps and reduce scan time.

Since conductivity is proportional to the curvature of the $\mathbf{B}_1^+$ field, and depending primarily on the phase, zero- and first-order polynomial terms in the phase will not affect the conductivity calculation. As seen in Figure 3.2, none of the combination methods exactly reproduce the OC data, but the AC and LC data have notably different curvature. These methods do not account for spatially varying coil-specific phase contributions, only the constant offset between coils. The phase difference in

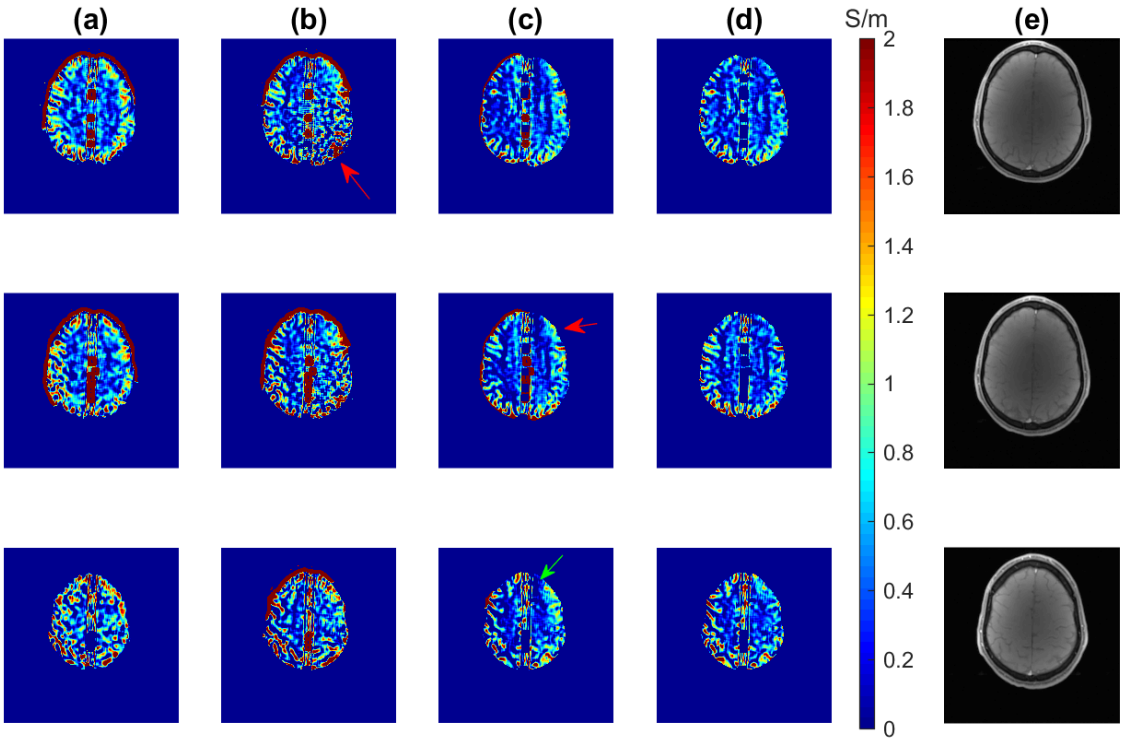

Figure 3.7: Conductivity maps calculated with MR-EPT for three slices of a human subject brain based on combined phase images using (a) Optimal Combination, (b) Adaptive Combination, (c) Local Compression, and (d) Local Compression with Background Phase Correction. (e) Magnitude image for reference. Green arrow indicates a region of reduced conductivity and red arrows indicate regions of elevated conductivity, both due to bias in the phase data.

the LC-BC method can be described by a lower order polynomial function, indicating there will be minimal effect on the conductivity maps. This method better estimates the coil-specific phase components and removes them from the combined image. This is confirmed by the conductivity maps for both the phantom and the human brain. The phantom conductivity images are more uniform for the LC-BC method and the human brain conductivity shows fewer regions of over- or underestimation. One notable difference between the two phantoms is the varying uniformity of the conductivity map. We believe the spherical phantom has a lower uniformity because more of the individual channels are important in the combination procedure.

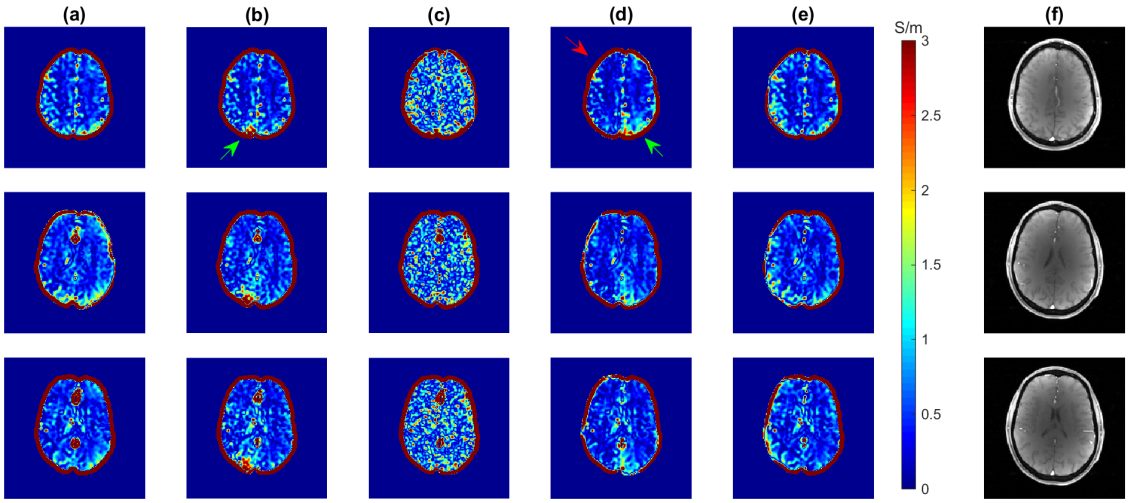

Figure 3.8: Phase-based conductivity maps for three slices of a human subject brain based on combined phase images using (a) Optimal Combination, (b) Adaptive Combination, (c) Magnitude Least Squares, (d) Local Compression, and (e) Local Compression with Background Phase Correction. (f) Magnitude image for reference. Red arrow indicates a region of reduced conductivity and green arrows indicate regions of elevated conductivity, both due to bias in the phase data.

The cylindrical phantom has a higher percentage of the volume in close proximity to the coil, but fewer channels are sensitive to the phantom, reducing the bias due to errors in estimating coil-specific contributions.

The goal of using a multi-coil receiver is to improve the SNR of the unprocessed images. The coil compression techniques used in LC and LC-BC yield optimal SNR in the phase data, similar to OC. In the background correction process we use a spatial filter for estimating the coil-specific phase contributions. However, we remove this smooth phase component from the original, unfiltered data so the degree of smoothing due to that filter affects only the phase SNR and not the spatial resolution of the resultant phase images.

While the conductivity maps from the coil-combined data do not exactly match those from quadrature birdcage coil data, the LC-BC minimizes the conductivity variation in the uniform phantoms without requiring a reference scan. Furthermore,

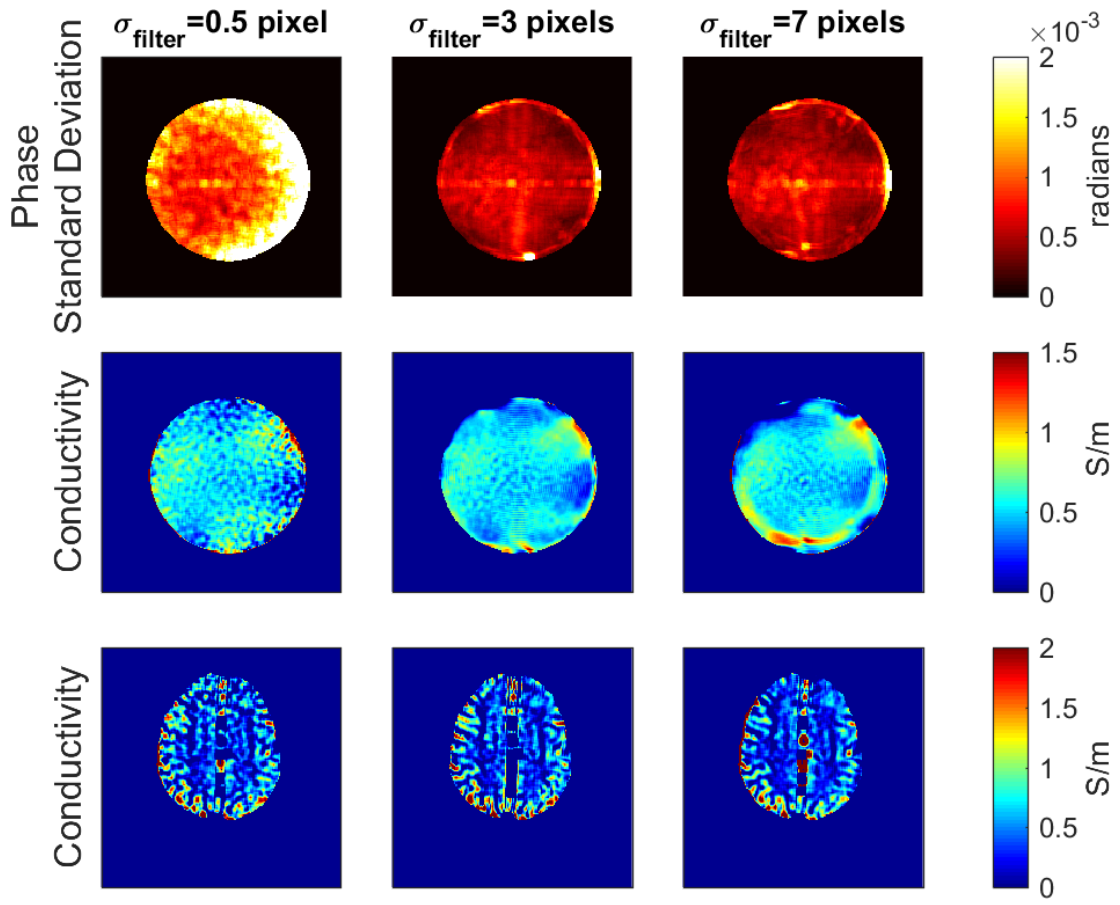

Figure 3.9: Comparison of Gaussian filter standard deviation size on LC-BC (Top) Phase Variance in the combined phantom image. (Middle) Phantom conductivity. (Bottom) Conductivity for a human subject. The Gaussian filter standard deviations are (Left to Right) 0.5, 3, and 7 pixels. The filter widths are $(4\sigma_{filter} + 1)$ pixels.

LC-BC yields very similar conductivity maps to OC in the human brain. In Figure 3.7, we believe the OC conductivity maps are sub-optimal due to additional noise in the magnitude data, which affects the conductivity calculation. Thus, we observe regions with elevated or highly variable conductivity, similar to the AC method. In the brain, the arrow in Figure 3.7 on the AC method shows notable noise amplification. Arrows on the LC method show over- and underestimation of conductivity due to bias in the phase data. The results in Figure 3.8 are from a different subject from Figure 3.7, but

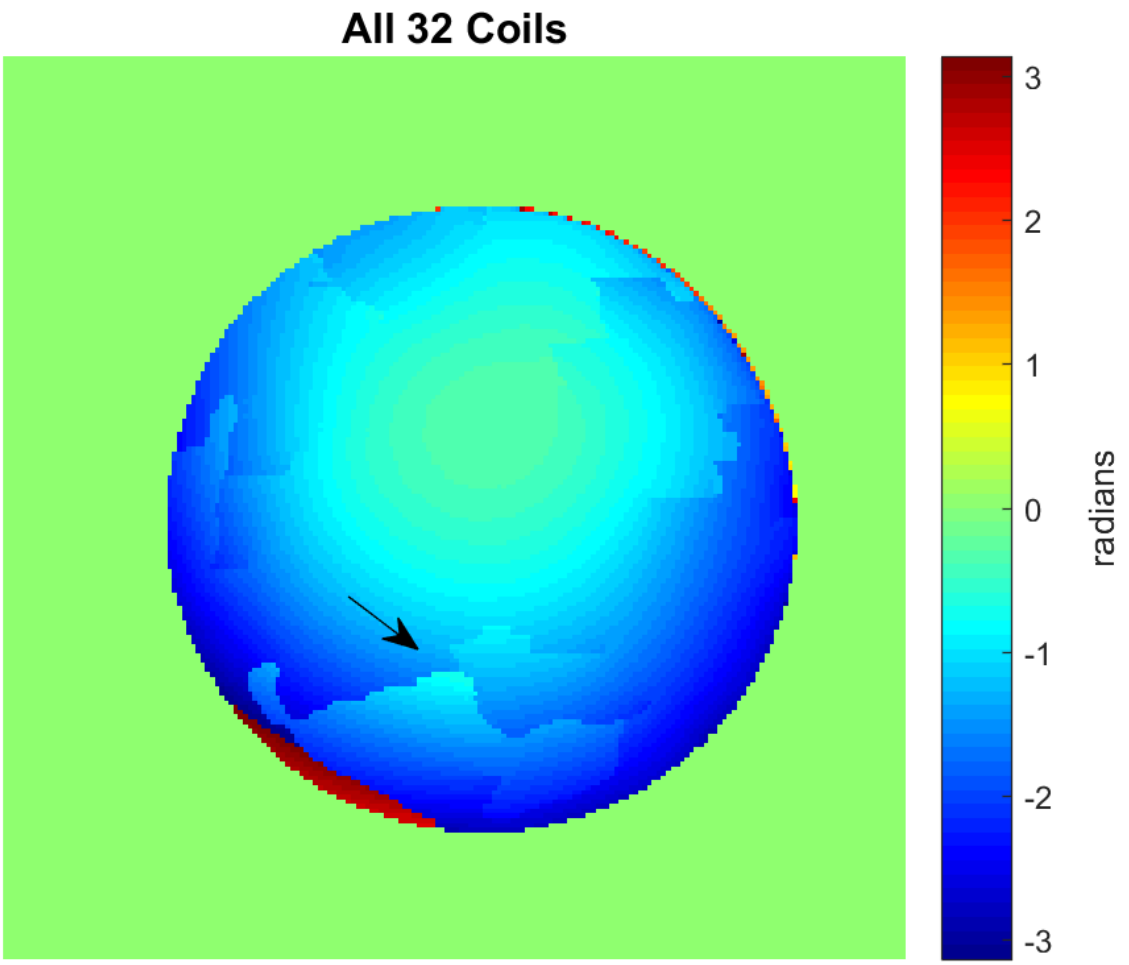

Figure 3.10: Combined phase using the LC-BC method with all 32 coils, regardless of whether they had open-ended phase wraps. The black arrow denotes an artifact that results from the open-ended phase wraps propagating through the combination process.

we see similar results. The AC and LC methods show over- and under-estimations of conductivity due to phase bias. Furthermore, it is clear that the regularization parameter for the MLS method is too low in the brain because the conductivity map is very noisy. This parameter would need to be re-tuned, which is a downfall of the MLS method.

Figure 3.9 shows the phase standard deviation and conductivity results for different values of the filter parameter, which is the standard deviation of the Gaussian

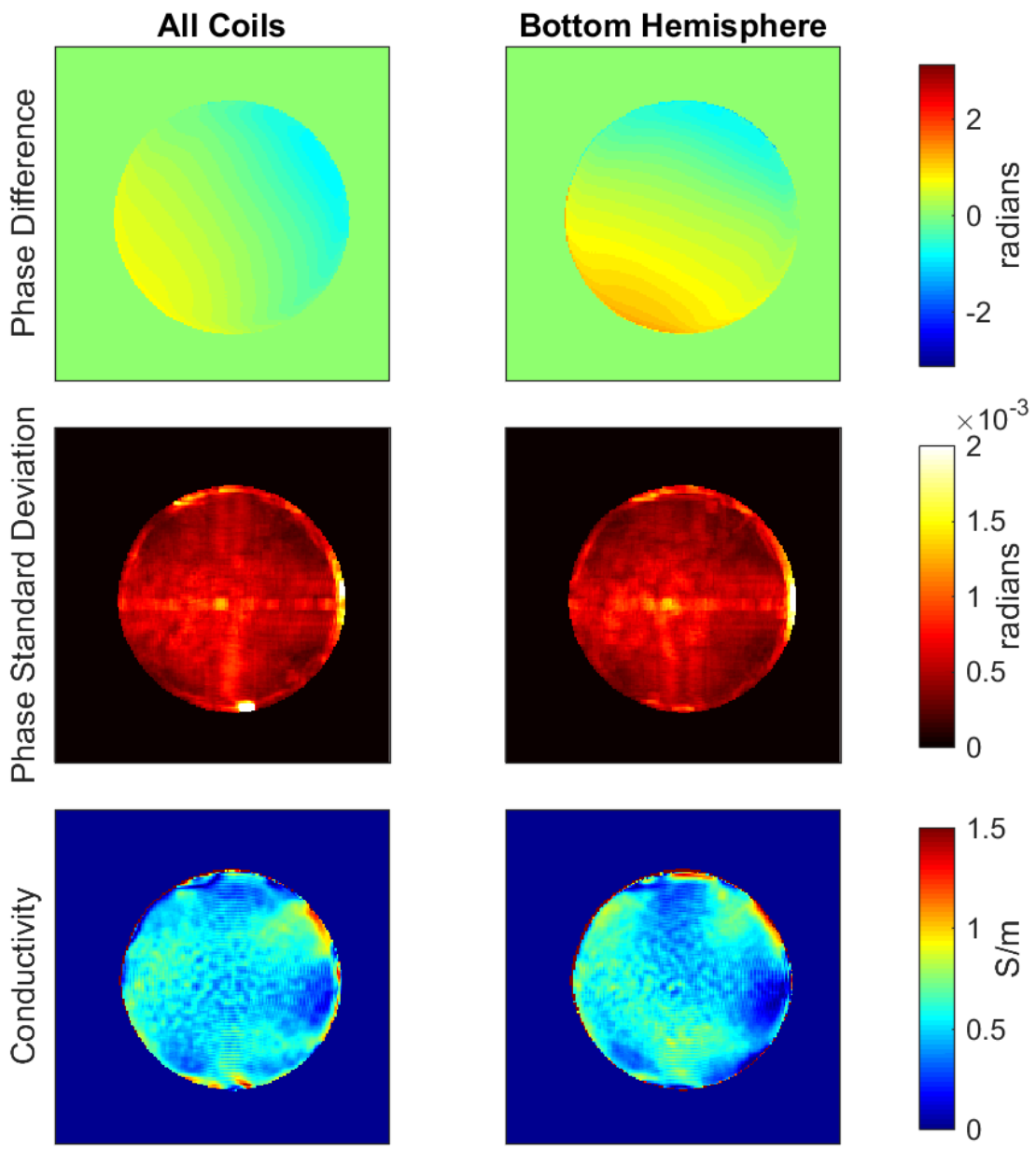

Figure 3.11: Comparison of combination using all coils without open-ended phase wraps (Left) and only coils in the bottom hemisphere of the coil without open-ended phase wraps (Right) in the background correction step of LC-BC. (Top) Phase difference with respect to the Optimal Combination. (Middle) Standard deviation of the combined phase data. (Bottom) Resultant conductivity maps.

distribution. The phase standard deviation is much higher for a parameter of 0.5 pixels, but does not improve noticeably from 3 to 7 pixels. A filter with too low standard

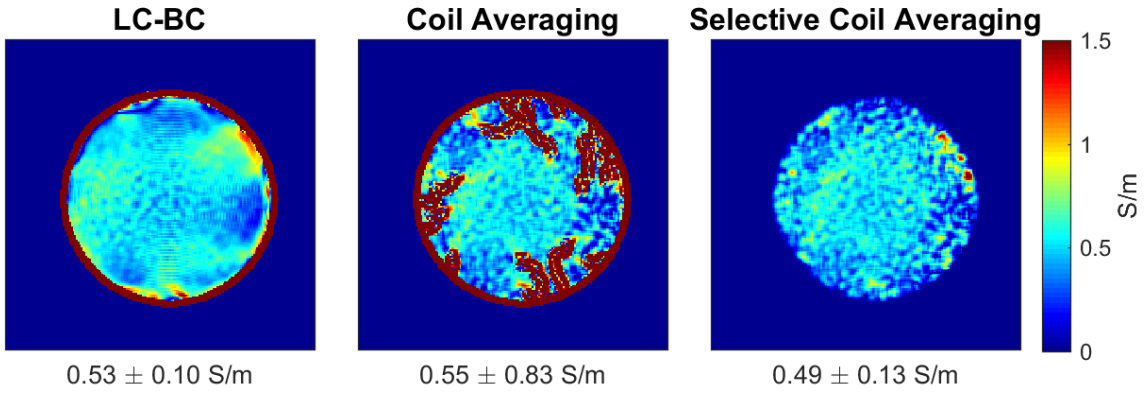

Figure 3.12: Comparison of phase-based conductivity calculations from multi-coil data. The mean and standard deviation are given below the figures. (Left) Phase data combined using the proposed LC-BC method and conductivity calculated using the combined data. (Middle) Conductivity calculated for each receive coil independently, then combined using a weighted average. (Right) Conductivity calculated for each receive coil independently, regions near open-ended phase wraps removed, and then combined using a weighted average.

deviation will cause noise amplification because the coil-specific phase is removed by dividing the original unfiltered data by the background phase estimate with a uniform magnitude. The conductivity images are relatively similar for the three filter standard deviations, with the higher noise clearly visible in the images corresponding to a filter parameter of 0.5 pixels. We observe slightly more conductivity bias in the spherical phantom for a parameter value of 7 pixels, indicating that too large of a filter may smooth out some of the high spatial frequency content in the phase data. Therefore, we conclude that a higher standard deviation will improve the phase SNR, but has an upper bound due to phase bias. As a result we used a parameter value of 3 pixels for all other experiments, but believe any parameter value between 1 and 5 pixels will produce similar results.

The result of using all 32 coils in the LC-BC method is shown in Figure 3.10, where the arrow denotes one of several open-ended phase wraps that propagated through the combination process. We use a quality-guided phase unwrapping procedure , which

allows us to unwrap most of the image, but there exist discontinuities that would certainly present a problem in the conductivity calculations. Figure 3.11 shows the effect of the physical locations of the individual coils on the LC-BC combination. The slice shown was a combination of 7 coils. We observe a larger difference from the optimally combined phase when only half of the coils are available, which leads to elevated conductivity regions near the edges of the phantom. Overall, the conductivity values are very similar, so we believe our method is not strongly dependent on the spatial locations of the subset of coils used in the background correction phase.

Although combining multi-channel data for phase-based conductivity mapping is not necessary, we believe it is beneficial. As seen in Figure 3.12, simply averaging the individual channel conductivities is not always possible due to open-ended phase wraps in the individual channel phase data. Cropping out regions affected by these phase wraps is primarily a heuristic method, as the extent of the error depends on the method used for conductivity mapping, which includes but is not limited to filter selections. In addition, excluding these regions means that not all of the transmit and receive phase quantities are accounted for and the resultant conductivity may be inaccurate. Even when selectively averaging coils, the standard deviation of the conductivity is higher than when using the proposed LC-BC method. This is because the conductivity calculation amplifies noise in the phase data to an extent that would require more low pass filtering. It is more beneficial to combine the phase data first so that there is lower noise content for the conductivity calculation.

Furthermore, we have shown a comparison between the proposed LC-BC method and the MLS method, which is also intended for phase-based conductivity mapping. The MLS method performed poorly in the brain, most likely due to too low of a regularization parameter. Tuning a parameter is undesirable, especially when it must be tuned for different objects or body parts. Furthermore, we believe that while a larger regularization parameter in the MLS method would increase the SNR in

the phase, it would likely lead to some undesirable smoothing of fine details in the anatomy.

In summary, we propose a data-driven multi-coil data combination method for MR-EPT. The proposed LC-BC method first implements a background phase correction to reduce bias due to high sensitivity coils. Second, the data is combined pixel-wise to optimize SNR in the combined data. This method preserves both high- and low-frequency phase components and produces similar conductivity maps to the Optimal Combination procedure in both uniform phantoms and the human brain. In comparison to the conductivity maps calculated from a single birdcage coil, the multi-coil conductivity maps show more variation due to bias in the combination. While the multi-coil data provides gains in SNR, there are certainly applications where the bias in the multi-coil data is far less desirable than noise in the image. We believe the trade-off between SNR and bias is application- and object-dependent, and using a birdcage coil may be a better option in some applications.

CHAPTER IV

Conductivity Tensor Mapping

4.1 Introduction

Conductivity mapping has applications in clinical diagnostics as well as RF safety. For applications such as SAR prediction where it is important to know how electromagnetic fields behave in the body, current practices typically use isotropic, or scalar-valued, conductivity values. If conductivity is anisotropic, meaning that it has some directionality, it can be represented by a tensor. Measuring conductivity as a tensor provides additional information as to how tissues conduct electric current, which could improve models used in SAR prediction and other applications.

The most common way to estimate the conductivity tensor is by scaling the diffusion tensor. The model presented by Tuch et al. (113) is for low-frequency conductivity tensors, derived from a two compartment model. This assumes electric current is spatially restricted in the same manner as diffusion, which may not be true. At low frequencies, the conductivity of a tissue primarily depends on the cell membrane impedance. Tissues with anisotropic diffusion typically have one long dimension, determined by the structure of the tissue, restricting the travel of water. The model in (113) assumes that conductivity is also restricted by tissue structure, presumably because the molecules that determine the tissue structure are insulating. While the low-frequency conductivity tensor is desirable for some applications, many of the MR-

EPT applications require the high-frequency conductivity estimate. Furthermore, in the high-frequency domain we believe that the two compartment model is not valid due to the negligible impedance of the cell membrane, as discussed in Chapter I.

There have been attempts at measuring the degree of anisotropy of electrical properties using MR-EPT, but, to the best of our knowledge, no full tensor measurements. Katscher et al. (114) proposed a method of estimating anisotropy of electrical conductivity based on the MR-EPT equations presented in (55). In this formulation, instead of taking the curl of Ampere's law, we solve for the complex permittivity by calculating the line integral of Ampere's law around some area, A, and dividing by the integral form of Faraday's law. For an object with anisotropic conductivity, the selection of the integration area A is important, as the calculated conductivity value will change depending on the orientation of A with respect to the eigenvectors of the tensor. The benefit of this approach is the ability to calculate conductivity for multiple integration areas with a single acquisition. The limitations are the complexity of integration and the necessity to use a large number of integration planes in trying to determine the primary eigenvector of an unknown tensor. The work by Lee et al. (115) builds upon the theory in (114), and proposes a method for calculating the tensor given the eigenvalues. This would require prior knowledge of the structure of the object or, as the authors suggest, diffusion tensor data. The authors also propose a qualitative metric for determining anisotropy which, in practice, requires rotation of the object to capture the anisotropic behavior.

To measure the full tensor one must change the orientation of the object within the main magnetic field. This is challenging due to bore size, coil size, and limited subject mobility. The brain is one region of the body where conductivity tensor measurements would not only be feasible, but also useful. The brain contains large white matter tracts, which have an insulating outer layer composed of myelin and a highly conductive inner layer for rapid communication between different regions

of the brain. Isotropic estimates of white matter are typically low due to the large fraction of myelin. However, it is reasonable to believe that electromagnetic fields would propagate differently if applied along the length of the tract as opposed to across its width. In this work we present a mathematical framework for calculating the conductivity tensor. We also propose two methods for calculating the tensor - a direct calculation and a dictionary-based approach - to explore the feasibility of calculating the tensor with small degrees of rotation of the object within the bore.[1]

4.2 Theory

4.2.1 The Conductivity Tensor

Consider an object in an MRI scanner, allowed to freely rotate. Let the object have a coordinate system, (x, y, z), separate from the scanner coordinate system, (x', y', z'). In some initial orientation the coordinate systems are the same, but as we rotate the object, the object coordinates are considered stationary while the scanner coordinates rotate with respect to the object. The following derivations assume that, because we can only measure the transverse component of the magnetic field in an MRI scanner, only the longitudinal component of the corresponding electric field is relevant to the problem. Thus, to describe these fields, we must define the unit vector in the longitudinal direction of the scanner, or the $\mathbf{B}_0$ direction. We define $\hat{z} = [z_x, z_y, z_z]$ as the unit vector in the direction of $\mathbf{B_0}$, or z', with its components defined in terms of the object coordinate system, as shown in Figure 4.1.

In deriving the equations for this approach to conductivity tensor mapping, we will show, first, how the electromagnetic fields change with object orientation and, second, how calculated conductivity changes with those fields. To begin, MR-EPT is

[1]Parts of this chapter have been submitted as: K.M. Ropella, S. J. Peltier, and D.C. Noll, A Dictionary-Based Method for Conductivity Tensor Mapping, Submitted to the 26th annual meeting of the ISMRM.

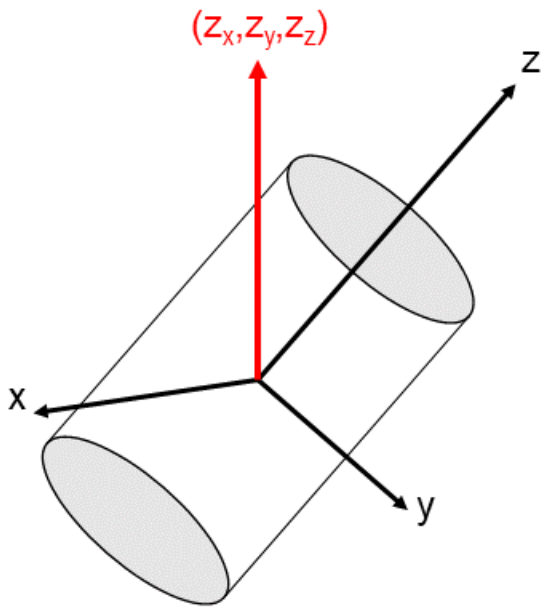

Figure 4.1: Representation of the $\hat{z}$ vector coordinates, defined with respect to the object.

derived from the homogeneous Helmholtz equation:

$$-\nabla^2\mathbf{H} = \nabla \times j\omega\kappa\mathbf{E} \qquad [4.1]$$

where $\mathbf{H}$ is the magnetic field, $\mathbf{E}$ is the electric field, ω is the MRI resonant frequency, and $\kappa = \epsilon - j\frac{\sigma}{\omega}$ is the complex permittivity, with ϵ the permittivity and σ the conductivity. If κ is isotropic it can be written as a scalar value, and pulled out of the curl operator. Applying Faraday's law,

$$\nabla \times \mathbf{E} = -j\omega\mathbf{H}, \qquad [4.2]$$

and rearranging terms gives the isotropic complex permittivity:

$$\kappa = \frac{-\nabla^2\mathbf{H}}{\omega^2\mu_0\mathbf{H}}. \qquad [4.3]$$

For an object with isotropic electrical properties, the calculated value of κ will be independent of the object's orientation within the MRI scanner. However, if κ is anisotropic, the apparent measured value will depend on the orientation of the object. Anisotropic complex permittivity is written as a tensor, $\underline{\underline{\kappa}}$, which is symmetric and therefore can be written in two forms:

$$\underline{\underline{\kappa}} = \begin{bmatrix} \kappa_1 & \kappa_4 & \kappa_6 \\ \kappa_4 & \kappa_2 & \kappa_5 \\ \kappa_6 & \kappa_5 & \kappa_3 \end{bmatrix} \quad [4.4]$$

$$\underline{\kappa} = \begin{bmatrix} \kappa_1 & \kappa_2 & \kappa_3 & \kappa_4 & \kappa_5 & \kappa_6 \end{bmatrix}. \quad [4.5]$$

Although $\underline{\underline{\kappa}}$ is a tensor, at a given orientation we measure an apparent scalar value of $\tilde{\kappa}$. With conductivity measurements at six non-collinear orientations, we hypothesize that we can estimate the full tensor. First we show how the electric and magnetic fields change with orientation, followed by a discussion of how the calculated conductivity changes with respect to the magnetic field measurement.

At a given orientation we measure the magnetic field, $\tilde{\mathbf{H}}$, and calculate the apparent value $\tilde{\kappa}$. Applying Faraday's law is essential in deriving Equation 4.3 from Equation 4.1, so we will first examine the electric fields, followed by the magnetic fields, in this problem. We define the orientation-dependent electric field in terms of the incident field $\mathbf{E} = [E_{x'}, E_{y'}, E_{z'}]$, whose components are in scanner coordinates,

$$\tilde{\mathbf{E}} = \underline{\underline{\kappa}}\mathbf{E}^T = \underline{\underline{\kappa}}[E_{x'}, E_{y'}, E_{z'}]^T \quad [4.6]$$

and assume $\mathbf{E}$ and $\underline{\underline{\kappa}}$ are constant. The quantity $\kappa\mathbf{E}$ is technically defined as the field $\mathbf{D}$. Because we are focusing on the orientation dependency of the electrical property calculations, we have chosen to call this quantity $\tilde{\mathbf{E}}$ to emphasize this is the observed electric field in a given orientation. This is the electric field that is the result of the

incident field $\mathbf{E}$ interacting with the object with dielectric properties $\underline{\underline{\kappa}}$.

By Faraday's law, $\tilde{\mathbf{H}}$ is proportional to the curl of $\tilde{\mathbf{E}}$, but only the longitudinal component of $\tilde{\mathbf{E}}$, $\tilde{E}_{z'}$, is relevant:

$$\begin{aligned}\tilde{\mathbf{E}} \cdot \hat{z} =& \kappa_1 E_{x'} z_x + \kappa_2 E_{y'} z_y + \kappa_3 E_{z'} z_z + \kappa_4 E_{y'} z_x + \kappa_4 E_{x'} z_y + \\ & \kappa_5 E_{z'} z_y + \kappa_5 E_{y'} z_z + \kappa_6 E_{z'} z_x + \kappa_6 E_{x'} z_z. \end{aligned} \quad [4.7]$$

As discussed earlier, we assume that the only non-zero component of the incident electric field $\mathbf{E}$ is the longitudinal component, $E_{z'}$. This is the longitudinal component with respect to the scanner, but again we must write it in the object components. Therefore, the observed field is a scalar times $\hat{z}$:

$$\tilde{\mathbf{E}} \cdot \hat{z} \propto \begin{bmatrix} \kappa_1 z_x z_x & \kappa_2 z_y z_y & \kappa_3 z_z z_z & 2\kappa_4 z_x z_y & 2\kappa_5 z_y z_z & 2\kappa_6 z_x z_z \end{bmatrix}. \quad [4.8]$$

We define the vector

$$\mathbf{z} = \begin{bmatrix} z_x z_x & z_y z_y & z_z z_z & 2z_x z_y & 2z_y z_z & 2z_x z_z \end{bmatrix} \quad [4.9]$$

to write these relationships more succinctly. As discussed at the beginning of the section, we measure the transverse component of the magnetic field which corresponds to the longitudinal component of the electric field. The magnetic field is proportional to the curl of the electric field. The curl operator is a linear operator. We have just shown how the electric fields change with position in Equation 4.8, and therefore the magnetic field changes in the same manner:

$$\tilde{\mathbf{H}} \propto \underline{\kappa} \cdot \mathbf{z} = \begin{bmatrix} \kappa_1 & \kappa_2 & \kappa_3 & \kappa_4 & \kappa_5 & \kappa_6 \end{bmatrix} \cdot \begin{bmatrix} z_x z_x & z_y z_y & z_z z_z & 2z_x z_y & 2z_y z_z & 2z_x z_z \end{bmatrix}. \quad [4.10]$$

This means that the tensor $\underline{\underline{\kappa}}$ acts upon the field $\mathbf{E}$, which has a non-zero z'-component,

to produce $\tilde{\mathbf{E}}$. We are interested in how much of $\tilde{\mathbf{E}}$ remains in the z'-component to estimate the tensor. The measured magnetic field is therefore proportional to the dot product of the complex permittivity tensor and the vector $\mathbf{z}$. For instance, the apparent conductivity will be at a maximum when the primary eigenvector of the tensor is aligned with $\hat{z}$ and at a minimum when the primary eigenvector is perpendicular to $\hat{z}$.

We have shown how the electric fields are altered by a medium with anisotropic conductivity and how the measured magnetic fields change with the electric fields. Next we examine how the measured conductivity changes with respect to the measured magnetic field. To the leading order, the conductivity of a material primarily affects the phase of the magnetic field (63). The phase-based conductivity approximation is

$$\sigma \approx \frac{\nabla^2 \phi^+}{\omega \mu_0} \qquad [4.11]$$

where ϕ^+ is the phase of the transmit RF magnetic field, $\mathbf{B}_1^+$. This approximation is linear and phase enters the receive coils linearly. Let us define the conductivity tensor in a similar manner as the complex permittivity tensor, as a symmetric 3×3 matrix that can also be written as a vector of six elements:

$$\underline{\Sigma} = \begin{bmatrix} \Sigma_1 & \Sigma_2 & \Sigma_3 & \Sigma_4 & \Sigma_5 & \Sigma_6 \end{bmatrix}. \qquad [4.12]$$

Phase enters the MRI receiver coils in a linear fashion and Equation 4.11 is linear with respect to the transmit phase. Given the linearity of the system for measuring and calculating conductivity from the transmit RF field, we can assume that

$$\phi^+ \propto \underline{\Sigma} \cdot \mathbf{z}. \qquad [4.13]$$

Therefore, we can estimate the conductivity tensor from the phase-based conductivity

measurements in six different orientations. The measured conductivity values are concatenated into a vector

$$\mathbf{s} = \begin{bmatrix} \sigma_1 & \sigma_2 & \sigma_3 & \sigma_4 & \sigma_5 & \sigma_6 \end{bmatrix} \quad [4.14]$$

and we can solve for $\underline{\underline{\Sigma}}$ by a simple calculation:

$$\hat{\underline{\underline{\Sigma}}} = \mathbf{Z}^{-1}\mathbf{s}. \quad [4.15]$$

Here, $\mathbf{Z}$ is size 6×6, where each column is the vector $\mathbf{z}$ corresponding to one orientation. We refer to this as the direct calculation of the tensor.

Given more than six orientations, one can also solve for $\underline{\underline{\Sigma}}$ using the pseudo-inverse or truncating the singular value decomposition (SVD) of the matrix $\mathbf{Z}$. After calculating $\underline{\Sigma}$, it is reshaped into $\underline{\underline{\Sigma}} = \begin{bmatrix} \Sigma_1 & \Sigma_4 & \Sigma_6 \\ \Sigma_4 & \Sigma_2 & \Sigma_5 \\ \Sigma_6 & \Sigma_5 & \Sigma_3 \end{bmatrix}$. The eigen-decomposition

$$\underline{\underline{\Sigma}} = \begin{bmatrix} \mathbf{v}_1 & \mathbf{v}_2 & \mathbf{v}_3 \end{bmatrix} \begin{bmatrix} \lambda_1 & 0 & 0 \\ 0 & \lambda_2 & 0 \\ 0 & 0 & \lambda_3 \end{bmatrix} \begin{bmatrix} \mathbf{v}_1 & \mathbf{v}_2 & \mathbf{v}_3 \end{bmatrix}^H \quad [4.16]$$

is useful in determining the directionality of the conductivity tensor.

4.2.2 Dictionary-Based Tensor Calculation

We also propose a dictionary-based method to calculate $\underline{\Sigma}$. We created a dictionary of tensors by incrementally changing the eigenvalues and direction of the eigenvectors. The eigenvalues were constrained to be non-negative and the direction of the eigenvectors covered one hemisphere of three-space, due to the symmetry of tensors. For every atom, $\underline{\Sigma}_i$, we calculate the conductivity for each of the acquisition

orientations,

$$\mathbf{s}_i = \underline{\Sigma}_i \mathbf{Z}. \quad [4.17]$$

The error between the calculated and measured conductivity is

$$error_i = ||\mathbf{s}_i - s||_2 \quad [4.18]$$

and the optimal tensor from the dictionary is that with the lowest error. One could also use the ℓ_1-norm as an error metric.

4.3 Methods

4.3.1 Materials

Experiments were performed on a liquid phantom and a piece of beef shoulder. The liquid phantom was a cylinder with a diameter of 9.5 cm and height of 14.6 cm. The phantom was filled with a solution of copper sulfate and sodium chloride, which has a conductivity of 2.11 S/m, measured with a dielectric probe. The top half of the phantom was filled with densely packed drinking straws, parallel to the long axis of the cylinder. The beef shoulder had visible striations and dimensions of $15.2 \times 11.4 \times 3.8$ cm.

4.3.2 MRI Data Acquisition

Data was acquired on a 3.0T GE MR750 MRI scanner using a quadrature birdcage head coil. Sequence parameters were: TE/TR = 10/1000 ms, 128×128 matrix size, 5 mm slice thickness, and two averages. The field of view was 21 cm for the straw phantom and 24 cm for the beef. Diffusion tensor data was also acquired for the beef shoulder using an 8-channel head coil and a 32 direction blip-up/blip-down sequence with b=1000. The nominal orientations for data acquisition are listed in

Table 4.1. The optimal orientations are the best choice for accurately calculating the conductivity tensor because they include acquisitions with the object rotated toward each of the cartesian axes. The practical orientations are within the range of motion of a subject's head.

As a general exploration of how apparent conductivity in the straw phantom changes with orientation, conductivity data was acquired at four different angles of rotation about the x-axis of the scanner between 0 and 90°. Then four experiments for calculating the full tensor were performed. First, conductivity data was acquired for the straw phantom and the optimal orientations listed in Table 4.1, where the straws were aligned with $\mathbf{B}_0$ in the initial position. Next, conductivity data was acquired for the straw phantom using the practical orientations, but the same initial position. The third experiment also used the optimal orientations, but the straws were aligned with the x-axis of the scanner in the initial position. The final straw phantom experiment used the optimal orientations with the straws positioned at an oblique angle, $\approx -50°$ about the y-axis, in the initial position. The third and fourth experiments were designed to test the feasibility of this approach when the initial $\hat{z}$ vector was not aligned with the straws, which is the hypothesized primary eigenvector of the tensor. Despite the straw position in these two experiments, the $\hat{z}$ vectors listed under Optimal Orientations in Table 4.1 are used so that the resultant tensors will be with respect to the scanner coordinates, as the object and scanner coordinates are collinear in the initial position.

For the beef shoulder, conductivity data was acquired using both the optimal and practical orientations where the striations were approximately parallel to $\mathbf{B}_0$ in the initial position. Diffusion tensor data was also acquired in the initial position.

Table 4.1: Coordinates of the $\hat{z}$ vector for two acquisition schemes. Optimal Orientations allows for the direct tensor calculation. Practical Orientations is based on the angles achievable by a human brain.

Optimal Orientations						
Orientation No.	1	2	3	4	5	6
$\mathbf{z}_x$	0	0	1	0	0.707	0.707
$\mathbf{z}_y$	0	1	0	0.707	0	0.707
$\mathbf{z}_z$	1	0	0	0.707	0.707	0
Practical Orientations						
Orientation No.	1	2	3	4	5	6
$\mathbf{z}_x$	0	0.259	0.5	0	0	0.433
$\mathbf{z}_y$	0	0	0	0.259	0.5	0.25
$\mathbf{z}_z$	1	0.966	0.866	0.966	0.866	0.866

4.3.3 Tensor Calculations

Due to the artifacts from the straws themselves, the straw phantom data was down-sampled by a factor of 4 in-plane to yield smooth phase images. The beef was not down-sampled. The conductivity for each orientation was calculated using the phase-based approximation in Equation 4.11 with a 9×9 Gaussian filter applied to the transmit phase prior to calculating conductivity. The actual angle of rotation of the object with respect to the first orientation was calculated using SPM8 (99). The actual rotations were used to determine $\mathbf{Z}$. In the straw phantom, the mean conductivity in each compartment at each orientation was used to compute a mean conductivity tensor and the tensor at each pixel. In the beef, the conductivity tensor was calculated pixel-wise after realignment based on the SPM rotation parameters. In addition, the mean conductivity tensor over the entire piece of beef was calculated. Conductivity tensors were calculated directly, as in Equation 4.15, and with the dictionary-based approach. The dictionary was constructed by defining the eigenvectors and eigenvalues first. The eigenvalues were varied between 0 and 2 in increments of 0.1. The eigenvectors were the unit vectors in the x-, y-, and z-directions rotated by an azimuthal and a polar angle, each incrementing by 10° from 0 to 180°. This dictionary is overcomplete for symmetric tensors.

The resultant conductivity tensors are given for the object in its initial orientation, from which all rotations are calculated. In the initial position the scanner and object coordinate systems are the same, so the tensor can be described in the scanner coordinates for ease of display. Diffusion tensors were calculated in the beef only using FSL(116, 117). Diffusion tensors are not shown for the straw phantom due to the mismatch in pixel size between the down-sampled conductivity images and the diffusion tensor images.

4.4 Results

In the straw phantom we see anisotropic behavior in both compartments, but the straws have a much higher degree of anisotropy. Figures 4.2 and 4.3 that conductivity in both compartments is at a maximum when the long axis of the cylinder is parallel to $\mathbf{B}_0$.

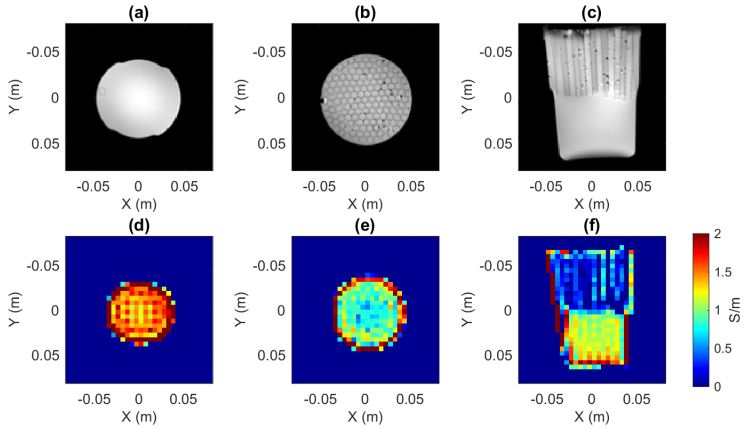

Figure 4.2: (a) Axial slice through open compartment in the zero degree of rotation position. (b) Axial slice through straw compartment in the zero degree of rotation position. (c) Axial slice through both compartments in the ninety degree of rotation position. (d) Calculated conductivity in the open compartment in the zero degree of rotation position. (e) Calculated conductivity in the straw compartment in the zero degree of rotation position. (f) Calculated conductivity in both compartments in the ninety degree of rotation position.

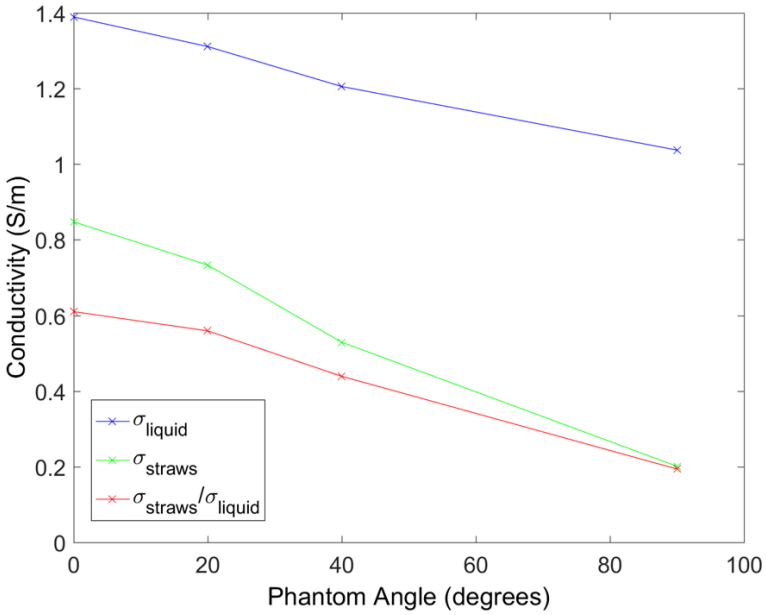

Figure 4.3: Measured conductivity for the straw and open compartments of the liquid phantom versus angle of the phantom. Zero degrees corresponds to the straws parallel to the $\mathbf{B}_0$ field in the scanner. Rotation angles are about the x-axis, which runs from left to right.

The mean conductivity tensors were calculated for both regions of the straw phantom using the mean conductivity values at each orientation. The resultant primary eigenvectors of the tensor are shown in Figure 4.2, where the arrow length corresponds to the degree of anisotropy. The full eigen-decompositions of these tensors are listed in Table 4.2. Given the optimal orientations, the primary eigenvector in the straw compartment aligns with the straws and we observe a high degree of anisotropy. The anisotropy in the open compartment is much lower, but the primary eigenvector is also aligned with the long axis of the cylinder. There is good agreement in the tensors calculated with the direct approach and the dictionary-based approach. For the practical orientations, the direct calculation yields one negative eigenvalue in the straw compartment, which is undesirable. The dictionary-based approach yields all positive eigenvalues, but the primary eigenvector appears to be a linear combination of the primary and secondary eigenvectors that were calculated using the optimal orientations. In the open compartment, the direct and dictionary-based tensors are

in agreement but there is an apparent increase in the degree of anisotropy using the practical orientations due to the underestimation of one of the eigenvalues. Based on the structure of the object, we believe the eigenvalues given the optimal orientations are accurate.

The primary eigenvector directions for tensors calculated from the optimal orientations in representative slices in each compartment are shown in Figure 4.5. The cross-sectional areas are slightly different in the two slices due to limited acquisition areas at all angles. In the open compartment, a majority of the vectors are nearly parallel to the z-direction. Those that are perpendicular to the z-direction are likely due to noise or boundary artifacts in the measurements. Due to the symmetry of the tensor, the arrows pointed up and pointed down are considered equivalent. In the straw compartment, some of the vectors are at a more oblique angle than the arrows in the open compartment. These may also be due to noise in the measurements.

When the direction of the straws was changed in the initial orientation, the direct calculation of the tensors from optimal orientations yielded primary eigenvectors that aligned with the straws, as shown in Figures 4.6 and 4.7. These images are shown with respect to the scanner coordinates to show that the direction of the straws is different. The primary eigenvector for the open compartment in the oblique angle was not aligned with the straws, but the degree of anisotropy was very low.

The conductivity tensor in the beef shoulder was calculated both pixel-wise and as a mean over the volume. Figure 4.8 shows the comparison of the conductivity tensor map with the diffusion tensor image. The images for both the diffusion tensors and conductivity tensors show the direction of the primary eigenvector of the tensor. Eigenvectors in the x-, y-, or z-direction will be red, green, or blue, respectively. Eigenvectors at an oblique angle will be a combination of those three colors. The colors are not weighted by the degree of anisotropy. There is a general agreement between the two tensors when the conductivity tensor is calculated with optimal ori-

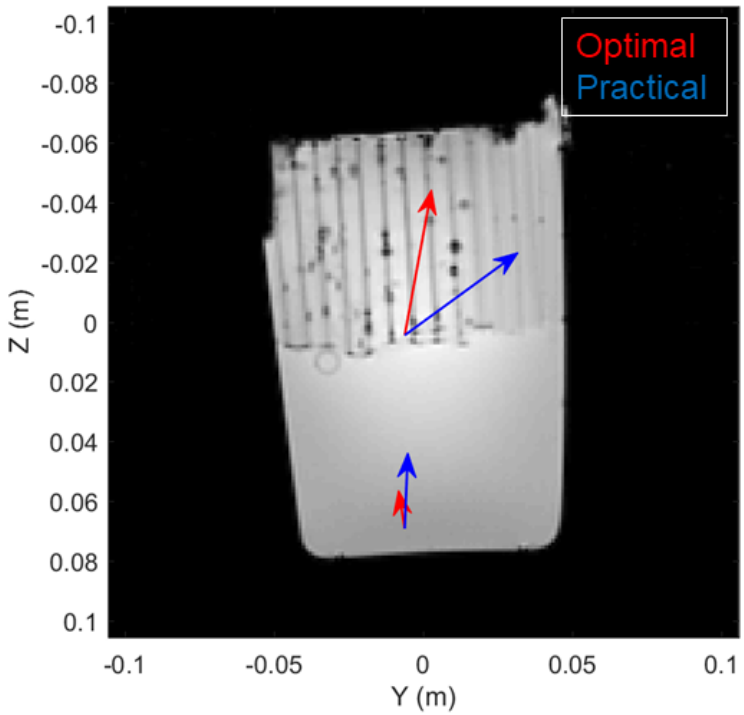

Figure 4.4: Sagittal view of the straw phantom showing the upper portion is filled with drinking straws and the lower portion is only liquid. The red arrows show the primary eigenvector of the mean conductivity tensor in each compartment calculated using the dictionary approach with optimal orientations. The blue arrows are the primary eigenvectors calculated using the dictionary approach with practical orientations. Vector length is proportional to the degree of anisotropy of the conductivity tensor.

entations. The practical orientations give a biased estimate of the primary eigenvector for a larger region of the beef shoulder, similar to the bias observed in the phantom. This is also reflected in the mean tensors given in Table 4.3.

4.5 Discussion and Conclusions

Calculating the conductivity tensor is important for studying how electromagnetic fields propagate through an object. The primary challenge in calculating the conductivity tensor based on MR-EPT is moving the object of interest to different orientations with respect to the main magnetic field. This is particularly challenging

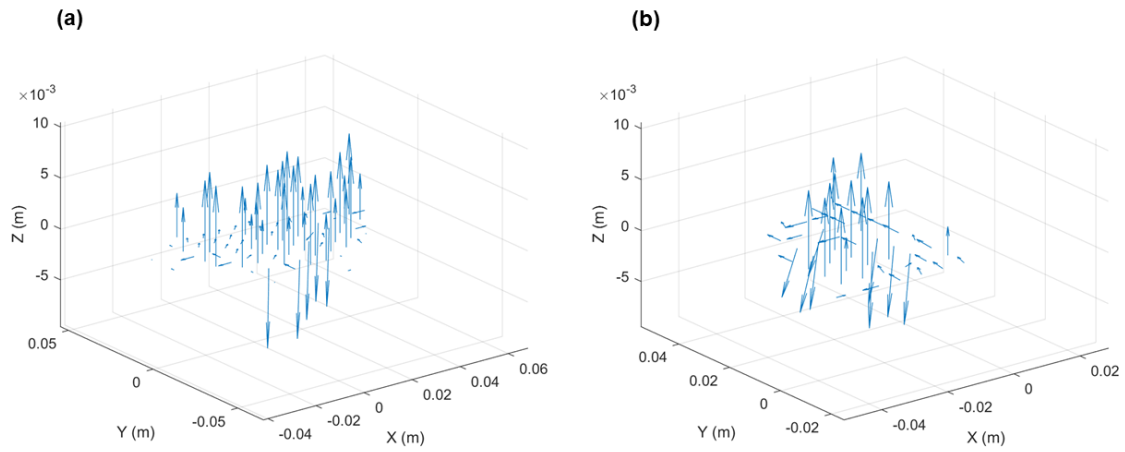

Figure 4.5: Quiver plots showing the direction of the primary eigenvector for the tensors at each pixel in representative slices from (a) the open compartment and (b) the straw compartment. The vector lengths are weighted within each plot by the degree of anisotropy, but the vector lengths in the two plots were scaled independently to aid in visualization.

in human subjects given the small bore size of the MRI scanner and limited degrees of freedom for subject movement. Calculating conductivity tensors may be possible in the human brain, as the head is relatively mobile and there exist large white matter tracts, in which conductivity is likely to be anisotropic. Previous work on conductivity tensors requires some knowledge of the eigenvectors of the tensor, commonly estimated by the diffusion tensor. We propose a mathematical framework for measuring the conductivity tensor that makes no assumption about the orientation of the tensor. We also suggest direct and dictionary methods that may be useful in estimating the tensor despite limitations on object movement.

The results of calculating the conductivity tensor the straw phantom, in three different positions, show that our proposed mathematical framework can be used to identify the tensor accurately, given the optimal orientations, with no prior knowledge about the directionality of the tensor. The arrows shown in Figures 4.4, 4.6, and 4.7 have small differences in the angle of the arrow with respect to the straws. This is

Table 4.2: Eigenvalues, λ_i, and eigenvectors, $\mathbf{v}_i$, of the mean conductivity tensor in each compartment of the phantom. Tensors were calculated using the optimal and practical orientation schemes and the direct calculation and the dictionary approach.

		λ_1	$\mathbf{v}_1$	λ_2	$\mathbf{v}_2$	λ_3	$\mathbf{v}_3$
Straws	Optimal	0.95	(-0.31, 0.13, 0.94)	0.21	(0.28, 0.96, -0.04)	0.12	(-0.91, 0.25, -0.34)
	Optimal, Dictionary	1.0	(0.32,) -0.12, 0.94)	0.2	(0.34, 0.94, 0.00)	0.1	(-0.88, 0.32, 0.34)
	Practical	0.91	(-0.38, 0.12, 0.92)	0.38	(-0.89, 0.23, -0.40)	-0.76	(0.26, 0.97, -0.02)
	Practical, Dictionary	1.5	(-0.38, 0.66, 0.64)	0.4	(0.56, -0.39, 0.73)	0.4	(-0.92, -0.28, -0.27)
Open	Optimal	1.41	(0.01, -0.12, 0.99)	1.05	(0.81, 0.58, 0.06)	0.99	(-0.58, 0.81, 0.10)
	Optimal, Dictionary	1.4	(0.09, -0.15, -0.98)	1.0	(0.99, 0.06, 0.08)	1.0	(-0.01, -0.99, 0.15)
	Practical	1.38	(-0.18, 0.02, 0.98)	1.11	(0.97, -0.17, 0.18)	0.31	(-0.17, -0.99, -0.01)
	Practical, Dictionary	1.4	(-0.17, 0.03, 0.98)	1.1	(-0.97, 0.17, -0.17)	0.3	(-0.17, -0.98, 0.00)

Table 4.3: Eigenvalues and eigenvectors of the mean conductivity tensor in the beef shoulder. Tensors were calculated using the optimal and practical orientation schemes and the dictionary approach.

	λ_1	$\mathbf{v}_1$	λ_2	$\mathbf{v}_2$	λ_3	$\mathbf{v}_3$
Optimal, Dictionary	0.5	(-0.30, -0.17, -0.94)	0.4	(0.81, -0.47, 0.34)	0.3	(0.50, -0.87, 0.00)
Practical, Dictionary	0.6	(-0.75, -0.43, -0.50)	0.5	(-0.43, -0.25, 0.87)	0.3	(-0.50, 0.87, 0.00)

likely due to inaccurate rotation angle calculations and projecting the vector into different planes. A second conclusion that can be drawn from the straw phantom results is that conductivity may be anisotropic on a larger scale than diffusion, warranting

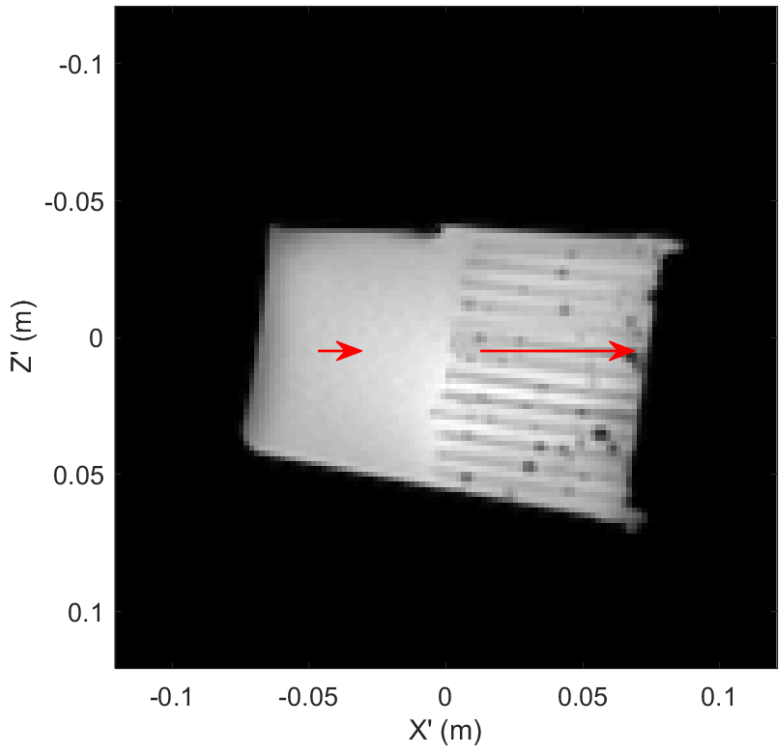

Figure 4.6: Coronal view of the phantom rotated 90 degrees about the y-axis. The red arrows show the primary eigenvector of the mean conductivity tensor in each compartment calculated using the dictionary approach with optimal orientations. Vector length is proportional to the degree of anisotropy of the conductivity tensor.

an approach that is independent of diffusion tensor measurements. The measured conductivity in the open compartment changed with orientation, indicating slight anisotropy. We would not expect anisotropic diffusion in the open compartment. We do not show diffusion tensor images for the straw phantom because the pixel size would not match that of the conductivity images due to down-sampling and because diffusion distance is much smaller than the diameter of the straw. Based on diffusion principles, we expect that the diffusion would only be anisotropic near the boundary of the straws, but not necessarily in the center of the straws.

In both the straw phantom and the beef, the conductivity tensors calculated from the practical orientations were not completely successful. When using the direct cal-

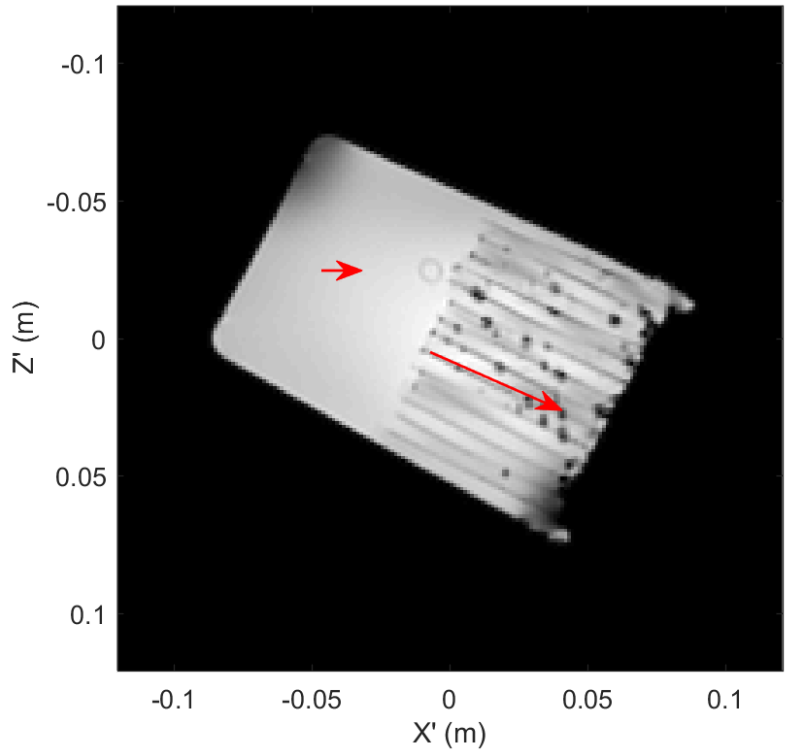

Figure 4.7: Coronal view of the phantom rotated approximately −50 degrees about the y-axis. The red arrows show the primary eigenvector of the mean conductivity tensor in each compartment calculated using the dictionary approach with optimal orientations. Vector length is proportional to the degree of anisotropy of the conductivity tensor.

culation approach, the primary eigenvector was fairly close to that calculated with the optimal orientations, but one eigenvalue was either negative of much lower than expected. We also tried restricting the eigenvalues to be non-negative, using the approach suggested in (118). However, this simply set the negative eigenvalue to zero. When using the dictionary-based approach, the primary eigenvector was biased toward the secondary eigenvector, but all eigenvalues were positive. Based on the tabular results, the dictionary-based approach seems to be similar to the direct calculation for more isotropic materials, like the open compartment. There are trade-offs for each approach and one might consider whether eigenvectors or eigenvalues are more important for describing conductivity.

Most of the results presented in this chapter are from the straw phantom. We

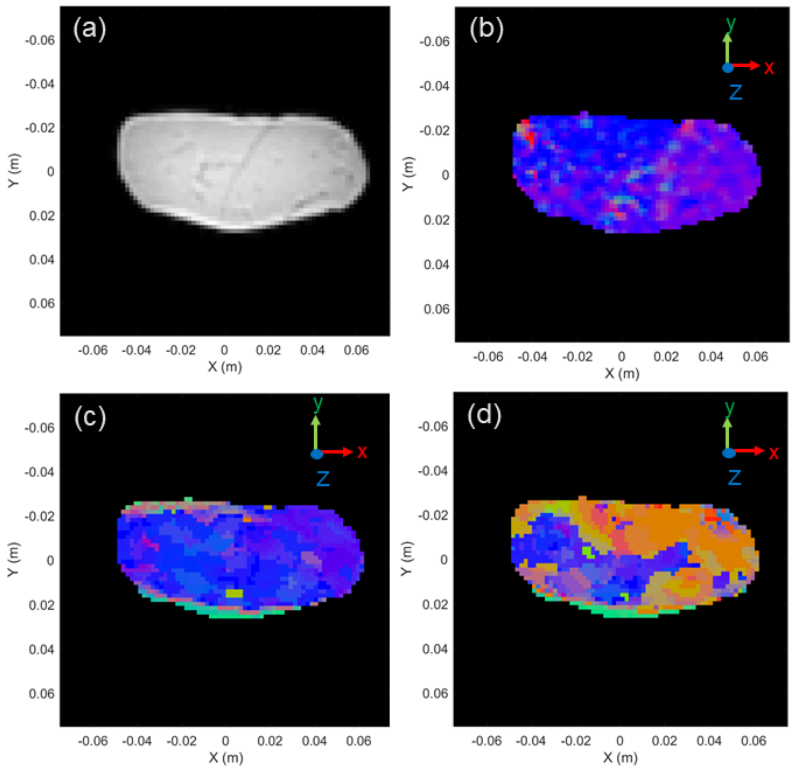

Figure 4.8: (a) Axial view of the beef shoulder. (b) Primary eigenvector direction of the diffusion tensors calculated in the beef. (c) Primary eigenvector direction of the conductivity tensor calculated using the optimal orientations. (d) Primary eigenvector direction of the conductivity tensor calculated using the practical orientations.

do not believe this is an accurate model of white matter tracts in the brain, but it allowed us to work with anisotropic conductivity. We believe plastic material of the straw was the source of two primary properties of the straw compartment. First, the straw compartment had a lower conductivity than the open compartment, as seen in Figure 4.3, despite being filled with the same saline solution. We hypothesize that the presence of the non-conductive material affects the propagation of fields and currents on a large scale, leading to lower apparent conductivity measurements. Second, the straw compartment was more anisotropic than the open compartment. We hypothesize the presence of the non-conductive straws makes for a more tortuous current path when current is applied perpendicular to the straws, and is less disruptive for current travelling parallel to the straws. A related observation about the phantom

is the small degree of anisotropy observed in the open compartment. We believe this is because all sides of that compartment are surrounded by plastic except for the boundary shared with the straw compartment. Thus, it is more conductive along that direction.

Finally, questions remain as to the meaning of the eigenvalues of the tensor. The maximum conductivity measured in the open compartment was much less than the conductivity measured with a dielectric probe. This underestimate may be due to the phase-based approximation or the 2D calculations. In the Theory section, we noted that the measured phase is proportional to the apparent conductivity. However, the scale of the positive eigenvalues are in the range of the apparent conductivity values.

In conclusion, we propose a mathematical framework for calculating the conductivity tensor based on the phase-based approximation to MR-EPT. We provide direct calculation and dictionary-based approaches to calculating the tensor, in an effort to make these calculations feasible in the brains of human subjects. Our proposed dictionary approach provides accurate tensor estimates for ideal object orientations. Given small, practical orientations, we are able to eliminate negative eigenvalues but there is a bias in the primary eigenvector. In the beef shoulder, conductivity tensors correlate well with the diffusion tensors. However, conductivity may have anisotropic behavior on a larger scale than diffusion, warranting an approach that does not depend on diffusion tensor data.

To improve on this approach we need to further investigate the impact of the object orientations on the accuracy of the conductivity tensor calculations, using either calculation method. Adding a non-negativity constraint to the eigenvalues or requiring two eigenvalues to be identical may also improve tensor estimates. Additionally, more efficient dictionary searches would be beneficial for further exploration of the dictionary-based calculations. Finally, the proposed method relies heavily on the electric fields only having a longitudinal component. A joint estimation of conductivity

and electric fields may be useful in relaxing that assumption.

CHAPTER V

Contributions and Future Work

Conductivity mapping has applications in RF safety, clinical diagnostics, and planning treatments involving electromagnetic fields. All of these applications have in common the need for high resolution, accurate conductivity maps. The primary goal of this dissertation is to present methods that improve conductivity mapping. These improvements include increasing accuracy near boundaries, improving SNR, and measuring anisotropic conductivity.

5.1 Phase-Based Conductivity Mapping

In Chapter II we presented a novel method for conductivity mapping using a regularized, model-based approach. We showed that our approach provides less noise amplification and reduced boundary artifact as compared to a conventional filtering method. While not directly compared to other inverse problems approaches, our method has several advantages over those approaches. First, the problem is formulated in three dimensions, whereas the CSI-EPT approach proposed by Balidemaj et al. (82) is not. Second, it is a manageable problem size for computation on a standard desktop computer, unlike the inverse problems approach from Borsic et al. (84). Finally, to the best of our knowledge, this is the first demonstration of an inverse problems approach in vivo. Both the boundary error reduction and SNR improve-

ments contribute to better accuracy in conductivity maps. The SNR improvement, or more specifically the reduction in noise amplification, is an important contribution towards high resolution conductivity mapping, as SNR in MRI data is proportional to voxel size.

There are some limitations to consider in using the proposed Inverse Laplacian method. The first is the mask calculations. The region of support mask is relatively straightforward, but the angiography can be time-consuming. We have also had success with thresholding a T1-weighted spoiled gradient echo image to achieve the same mask in a fraction of the time. The edge mask requires some tuning of the threshold parameter, which does not require extra acquisition time but does require user input for every reconstruction. The parameter value depends on the range of magnitude values and the contrast in the image. Another limitation is the computation time. As compared to a simple spatial filtering method, the proposed method computation time is orders of magnitude longer.

There are several opportunities for future work on the proposed Inverse Laplacian method. The simplest extension, although not trivial, involves adapting the Inverse Laplacian system model to solve for permittivity or even complex permittivity. The MR-EPT equation and magnitude-based permittivity approximation are nonlinear, unlike the phase-based conductivity approximation, making the system model more complex. Since phase-based conductivity approximations are less reliable at high field strengths, a model-based solution for complex permittivity would be applicable at all field strengths. Furthermore, RF safety is of greater concern at higher field strengths, motivating the adaptation of the method. Another extension of this work would be incorporating non-constant electrical properties into the model. We believe this would provide more accurate estimates at boundaries than a simple non-negativity constraint. This would most likely begin with quantifying the boundary error between different steps in conductivity, building off of work presented in (71).

5.2 Coil Combination

The methods described in Chapter III also aim to improve the SNR in conductivity maps, which contributes to accuracy and the feasibility of high resolution maps. We presented a referenceless method for combining complex, multi-channel MRI data for conductivity mapping. Conductivity mapping requires both the low spatial frequency contributions from background phase and the high spatial frequency contributions from local, object phase variations. Much of the phase combination literature is focused on quantitative susceptibility mapping, which only requires the high frequency component. The combination method for phase-based conductivity mapping presented in (106) requires parameter tuning. In our experience, the motivation to combine the complex data to achieve a uniform magnitude is not necessarily based on the phase behavior. Our proposed method does not require parameter tuning and is robust to coil arrangement. Additionally, it provides optimal SNR in the phase data.

The proposed combination method does not yield conductivity maps identical to those calculated from birdcage coil data. There remains some bias due to individual coil phases. Future work for this research aim should focus on making the coil combination more robust to individual coil phases. This is akin to better estimating sensitivity maps without a reference. This estimation could perhaps be built into an iterative, joint estimation of sensitivity maps and conductivity.

5.3 Conductivity Tensor Imaging

The research presented in Chapter IV provides a proof of concept for conductivity tensor mapping in vivo. We have presented a novel mathematical framework for calculating conductivity based on the phase-based approximation, accompanied by two different calculation methods. We have shown that the proposed framework does not require previous knowledge about the directionality of the conductivity tensor. The

methods proposed in (114, 115) are derived directly from the MR-EPT equations, with fewer approximations, but require knowledge of the eigenvectors of the tensor. Lee et al. (115) propose using the diffusion tensor to provide this information, but our phantom results suggest that conductivity is anisotropic on a larger scale than diffusion. To the best of our knowledge, this is the first attempt at estimating the whole conductivity tensor in an MR experiment, as opposed to the degree of anisotropy. Furthermore, our dictionary-based method may be useful in providing better tensor estimates despite low SNR in the conductivity measurements.

The major drawback of our conductivity tensor mapping approach is the time required to acquire conductivity data at six different orientations. Another limitation is the incomplete tensor estimation for acquisitions at practical orientations. While the direct calculation and dictionary-based calculation each provide partial information, we have yet to determine the best combination of practical orientations and calculation method to estimate the full tensor given the practical constraints.

There is quite a bit of future work required to make the proposed conductivity tensor mapping method feasible in the human brain. One item that would benefit the research process, but not necessarily improve the tensor estimates, is implementing more efficient dictionary searches. The search time could be reduced by creating a dictionary that is not over-complete to minimize the number of atoms and by implementing parallel processing. To further expedite the entire tensor mapping process, we will explore the minimum number of orientations required for the dictionary-based method to reduce acquisition time. Because the dictionary-based method finds the tensor that best fits the data, there is a relaxed requirement for the number of orientations and six acquisitions may be redundant. We believe we could optimize the orientations to provide the most variation in conductivity in the fewest acquisitions. Finally, the proposed mathematical framework employs assumptions about the components of the magnetic and electric fields. We may be able to reduce these as-

sumptions with a joint estimation of conductivity and electric fields. This would likely be an iterative process and involve more thorough modeling of the electromagnetic fields.

BIBLIOGRAPHY

[1] Gabriel C, Gabriel S, Corthout E. The dielectric properties of biological tissues: I. Literature survey. Phys Med and Biol 1996;41:2231–2249.

[2] Gabriel S, Lau RW, Gabriel C. The dielectric properties of biological tissues: II. Measurements in the freequency range 10Hz to 20 GHz. Phys Med Biol 1996; 41:2251–2269.

[3] Gabriel S, Lau RW, Gabriel C. The dielectric properties of biological tissues: III. Parametric models for the dielectric spectrum of tissues. Phys Med Biol 1996;41:2271–2293.

[4] Katscher U, van den Berg CA. Electric properties tomography: Biochemical, physical and technical background, evaluation and clinical applications. NMR Biomed 2017;30:e3729.

[5] Miranda PC, Hallett M, Basser PJ. The electric field induced in the brain by magnetic stimulation: a 3-D finite-element analysis of the effect of tissue heterogeneity and anisotropy. IEEE Trans Biomed Eng 2003;50:1074–1085.

[6] Wagner TA, Zahn M, Grodzinsky AJ, Pascual-Leone A. Three-dimensional head model simulation of transcranial magnetic stimulation. IEEE Trans Biomed Eng 2004;51:1586–1598.

[7] Wagner T, Fregni F, Fecteau S, Grodzinsky A, Zahn M, Pascual-Leone A. Transcranial direct current stimulation: A computer-based human model study. NeuroImage 2007;35:1113–1124.

[8] Sadleir RJ, Vannorsdall TD, Schretlen DJ, Gordon B. Transcranial direct current stimulation (tDCS) in a realistic head model. NeuroImage 2010;51:1310–1318.

[9] van Lier ALHMW, de Bruin PW, Aussenhofer SA, Luijten PR, Lagendijk JJW, van den Berg CAT, Webb AG. ^{23}Na-MRI and EPT: Are sodium concentration and electrical conductivity at 298MHz (7T) related? In Proceedings of the 21st Annual Meeting of ISMRM, Salt Lake City, UT, USA, 2013. p. 115.

[10] Sedlacik J, Katscher U, Fiehler J. Effect of ion size on conductivity measurements of MR-phase-based electric properties tomography. In Proceedings of the 23rd Annual Meeting of ISMRM, Toronto, ON, Canada, 2015. p. 3294.

[11] Liao YP, Oros-Peusquens AM, Lindemeyer J, Lechea N, Weiss C, Stoffels G, Filss C, Langen KJ, Shah NJ. Simultaneous water content, electrical conductivity and susceptibility mapping in meningiomas on a 3T MR-PET scanner. In Proceedings of the 24th Annual Meeting of ISMRM, Singapore, 2016. p. 1563.

[12] Michel E, Hernandez D, Lee SY. Electrical conductivity and permittivity maps of brain tissues derived from water content based on T1-weighted acquisition. Magn Reson Med 2017;77:1094–1103.

[13] Chaudhary SS, Mishra RK, Swarup A, Thomas JM. Dielectric properties of normal & malignant human breast tissues at radiowave & microwave frequencies. Indian Biochem Biophys 1984;21:76–79.

[14] Surowiec AJ, Stuchly SS, Barr JB, Swarup A. Dielectric properties of breast carcinoma and the surrounding tissues. IEEE Trans Biomed Eng 1988;35:257–263.

[15] Joines WT, Zhang Y, Li C, Jirtle RL. The measured electrical properties of normal and malignant human tissues from 50 to 900 MHz. Med Phys 1994; 21:547–550.

[16] Lazebnik M, Popovic D, McCartney L, Watkins CB, Lindstrom MJ, Harter J, Sewall S, Ogilvie T, Magliocco A, Breslin TM, Temple W, Mew D, Booske JH, Okoniewski M, Hagness SC. A large-scale study of the ultrawideband microwave dielectric properties of normal, benign and malignant breast tissues obtained from cancer surgeries. Phys Med Biol 2007;52:6093–6115.

[17] Katscher U, Djamshidi K, Voigt T, Ivancevic M, Abe H, Newstead G, Keupp J. Estimation of breast tumor conductivity using parabolic phase fitting. In Proceedings of the 20th Annual Meeting of ISMRM, Melbourne, VIC, Australia, 2012. p. 2335.

[18] Bulumulla S, Hancu I. Breast permittivity imaging. In Proceedings of the 20th Annual Meeting of ISMRM, Melbourne, VIC, Australia, 2012. p. 4175.

[19] Katscher U, Abe H, Ivancevic MK, Djamshidi K, Karkowski P, Newstead G. Towards the investigation of breast tumor malignancy via electric conductivity measurement. In Proceedings of the 21st Annual Meeting of ISMRM, Salt Lake City, UT, USA, 2013. p. 3372.

[20] Shin J, Kim MJ, Lee J, Nam Y, oh Kim M, Choi N, Kim S, Kim DH. Initial study on in vivo conductivity mapping of breast cancer using MRI. J Magn Reson Imag 2014;42:371–378.

[21] Katscher U, Abe H, Ivancevic MK, Keupp J. Investigating breast tumor malignancy with electric conductivity measurement. In Proceedings of the 23rd Annual Meeting of ISMRM, Toronto, ON, Canada, 2015. p. 3306.

[22] Shin JW, Kim MJ, Lee JS, Nam Y, Kim MO, Choi N, Kim S, Kim DH. Initial study on in vivo conductivity mapping of breast cancer using MRI. J Magn Reson Imaging 2015;42:371–378.

[23] Kim SY, Shin J, Kim DH, Kim MJ, Kim EK, Moon HJ, Yoon JH. Correlation between conductivity and prognostic factors in invasive breast cancer using magnetic resonance electric properties tomography (MREPT). Eur Radiol 2016; 26:2317–2326.

[24] Katscher U, Gagiyev M, Mori N, Tsuchiya K, Keupp J, Abe H. Conductivity of different malignancy grades of invasive carcinomas and fibroadenomas. In Proceedings of the 25th Annual Meeting of ISMRM, Honolulu, HI, USA, 2017. p. 0667.

[25] Voigt T, Vaterlein O, Stehning C, Katscher U, Fiehler J. In vivo glioma characterization using MR conductivity imaging. In Proceedings of the 19th Annual Meeting of ISMRM, Montreal, QC, Canada, 2011. p. 127.

[26] Huhndorf M, Stehning C, Rohr A, Helle M, Katscher U, Jansen O. Systematic brain tumor conductivity study with optimized EPT sequence and reconstruction algorithm. In Proceedings of the 21st Annual Meeting of ISMRM, Salt Lake City, UT, USA, 2013. p. 3626.

[27] Tha KK, Stehning C, Suzuki Y, Katscher U, Keupp J, Kazumata K, Terasaka S, Cauteren MV, Kudo K, Shirato H. Noninvasive evaluation of electrical conductivity of the normal brain and brain tumors. In Proceedings of the 22nd Annual Meeting of ISMRM, Milan, Italy, 2014. p. 1885.

[28] Tha KK, Katscher U, Stehning C, Yamaguchi S, Terasaka S, Sugimori H, Yamamoto T, Fujima N, Kudo K, Suzuki Y, Cauteren MV, Shirato H. Electrical conductivity characteristics of meningiomas: Noninvasive assessment using electric properties tomography. In Proceedings of the 23rd Annual Meeting of ISMRM, Toronto, ON, Canada, 2015. p. 4397.

[29] Tha KK, Katscher U, Yamaguchi S, Terasaka S, Yamamoto T, Kudo K, Shirato H. Electrical conductivity characteristics of glioma: Noninvasive assessment by MRI and its validity. In Proceedings of the 24th Annual Meeting of ISMRM, Singapore, 2016. p. 274.

[30] van Lier ALH, Kolk A, Brundel M, Hendrikse J, Luijten PR, Lagendijk J, van den Berg CAT. Electrical conductivity in ischemic stroke at 7.0 tesla. In Proceedings of the 20th Annual Meeting of ISMRM, Melbourne, Australia, 2012. p. 3484.

[31] Huhndorf M, Stehning C, Rohr A, Helle M, Stehle T, Katscher U, Jansen O. EPT-Measurement of brain conductivity for non-oncologic applications. In Proceedings of the 23rd Annual Meeting of ISMRM, Toronto, ON, Canada, 2015. p. 2194.

[32] Gurler N, Oran OM, Keklikoglu HD, Ider YZ. Application of generalized phase based electrical conductivity imaging in the subacute stage of hemorrhagic and ischemic strokes. In Proceedings of the 24th Annual Meeting of ISMRM, Singapore, 2016. p. 2994.

[33] Ouwerkerk R, Bleich KB, Gillen JS, Pomper MG, Bottomley PA. Tissue sodium concentration in human brain tumors measured with non-invasive ^{23}Na MRI. Radiology 2003;227:529–537.

[34] Ouwerkerk R, Jacobs MA, Macura KJ, Wolff AC, Stearns V, Mezban SD, Khouri NF, Bluemke DA, Bottomley PA. Elevated tissue sodium concentration in malignant breast lesions detected with non-invasive ^{23}Na MRI. Breast Cancer Res Treat 2007;106:151–160.

[35] Hussain MS, Stobbe RW, Bhagat YA, Emery D, Butcher KS, Manawadu D, Rizvi N, Maheshwari P, Scozzafava J, Shuaib A, Beaulieu C. Sodium imaging intensity increases with time after human ischemic stroke. Ann Neurol 2009; 66:55–62.

[36] Voigt T, Schuster A, Ishida M, Stehning C, Katscher U, Chiribiri A, Nagel E, Schaeffter T. Conductivity imaging of an ischemic pig heart model using electrical properties tomography. In Proceedings of the 20th Annual Meeting of ISMRM, Melbourne, VIC, Australia, 2012. p. 3483.

[37] Katscher U, Bornert P. Imaging of lung conductivity using ultrashort echo-time imaging. In Proceedings of the 22nd Annual Meeting of ISMRM, Milan, Italy, 2014. p. 2923.

[38] Balidemaj E, van Lier ALHMW, Crezee J, Nederveen AJ, Stalpers LJA, van den Berg CAT. Feasibility of electric property tomography of pelvic tumors at 3T. Magn Reson Med 2015;73:1505–1513.

[39] Balidemaj E, de Boer P, Crezee H, Remis R, Stalpers L, Nederveen AJ, van den Berg CAT. In vivo reconstructed conductivity values of cervical cancer patients based on EPT at 3T MRI. In Proceedings of the 23rd Annual Meeting of ISMRM, Toronto, ON, Canada, 2015. p. 3293.

[40] Gho SM, Shin J, Kim MO, Kim DH. Simultaneous quantitative mapping of conductivity and susceptibility using a double-echo ultrashort echo time sequence: Example using a hematoma evolution study. Magn Reson Med 2016; 76:214–221.

[41] Hancu I, Roberts JC, Bulumulla S, Lee SK. On conductivity, permittivity, apparent diffusion coefficient, and their usefulness as cancer markers at MRI frequencies. Magn Reson Med 2015;73:2025–2029.

[42] Gho SM, Shin JW, Kim MO, Kim MJ, Kim SY, Kim JH, Kim DH. Observation of the correlation between electrical conductivity and apparent diffusion coefficient values. In Proceedings of the 24th Annual Meeting of ISMRM, Singapore, 2016. p. 1566.

[43] Tha K, Katscher U, Yamaguchi S, Terasaka S, Shirato H. The relationship between diffusivity and electrical conductivity: Initial results of an in vivo assessment by MRI. In Proceedings of the 25th Annual Meeting of ISMRM, Honolulu, HI, USA, 2017. p. 4542.

[44] Graesslin I, Homann H, Biederer S, Bornert P, Nehrke K, Vernickel P, Mens G, Harvey P, Katscher U. A specific absorption rate prediction concept for parallel transmission MR. Magn Reson Med 2012;68:1664–1674.

[45] Alon L, Deniz CM, Brown R, Sodickson DK, Zhu Y. Method for in situ characterization of radiofrequency heating in parallel transmit MRI. Magn Reson Med 2013;69:1457–1465.

[46] Holder D. Electrical Impedance Tomography: Methods, History, and Applications. Bristol: IOP Publishing; 2005.

[47] Joy M, Scott G, Henkelman M. In vivo detection of applied electric currents by magnetic resonance imaging. Magn Reson Med 1989;7:89–94.

[48] Woo EJ, Seo JK, Lee SY. Electrical Impedance Tomography: Methods, History, and Applications, IOP Publishing, Bristol, 2005, chapter Magnetic resonance electrical impedance tomography (MREIT).

[49] Seo JK, Yoon JR, Woo EJ, Kwon O. Reconstruction of conductivity and current density images using only one component of magnetic field measurements. IEEE Trans Biomed Eng 2003;50:1121–1124.

[50] Birgul O, Eyuboglu BM, Ider YZ. Experimental results for 2D magnetic resonance electrical impedance tomography (MR-EIT) using magnetic flux density in one direction. Phys Med Biol 2003;48:3485–3504.

[51] Woo EJ, Seo JK. Magnetic resonance electrical impedance tomography (MREIT) for high-resolution conductivity imaging. Physiol Meas 2008;29:R1–R26.

[52] Griffiths H. Electrical Impedance Tomography: Methods, History, and Applications, IOP Publishing, Bristol, 2005, chapter Magnetic induction tomography.

[53] Rothwell EJ, Cloud MJ. Electromagnetics. Boca Raton, FL: CRC Press; 2009., 2 edition.

[54] Haacke EM, Petropoulos LS, Nilges EW, Wu DH. Extraction of conductivity and permittivity using magnetic resonance imaging. Phys Med Biol 1991; 36:723–734.

[55] Katscher U, Voigt T, Findeklee C, Vernickel P, Nehrke K, Dossel O. Determination of electric conductivity and local SAR via B1 mapping. IEEE Trans Med Imag 2009;28:1365–1374.

[56] van Lier ALH, van den Berg CAT, Katscher U. Measuring electrical conductivity at low frequency using the eddy currents induced by the imaging gradients. In Proceedings of the 20th Annual Meeting of ISMRM, Melbourne, Australia, 2012. p. 3467.

[57] Gibbs E, Liu C. Feasibility of imaging tissue electrical conductivity by switching field gradients with MRI. Tomography 2015;1:125–135.

[58] Oran OF, Ider YZ. Feasibility of Conductivity Imaging Using Subject Eddy Currents Induced by Switching of MRI Gradients. Magn Reson Med 2017; 77:1926–1937.

[59] Seo JK, Woo EJ, Katscher U, Wang Y. Electro-Magnetic Tissue Properties MRI. London: Imperial College Press; 2014. 277 p.

[60] Akoka S, Franconi F, Seguin F, LePape A. Radiofrequency map of an NMR coil by imaging. Magnetic Resonanace Imaging 1993;11:437–441.

[61] Yarnukh VL. Actual flip-angle imaging in the pulsed steady state: a method for rapid three-dimensional mapping of the transmitted radiofrequency field. Magn Reson Med 2007;57:192–200.

[62] Sacolick LI, Wiesinger F, Hancu I, Vogel MW. B1 Mapping by Bloch-Siegert Shift. Magn Reson Med 2010;63:1315–1322.

[63] Wen H. Non-invasive quantitative mapping of conductivity and dielectric distributions using the RF wave propagation effects in high field mri. In Proceedings of SPIE 5030, Medical Imaging 2003: Physics of Medical Imaging, San Diego, CA, USA, 2003. pp. 471–477.

[64] Katscher U, Kim DH, , Seo JK. Recent progress and future challenges in MR electric properties tomography. Comput Math Methods Med 2013;2013:546–562.

[65] Felmlee JP, Ehman RL. Spatial presaturation: a method for suppressing flow artifacts and improving depiction of vascular anatomy in MR imaging. Radiology 1987;164:559–564.

[66] Voigt T, Katscher U, Doessel O. Quantitative conductivity and permittivity imaging of the human brain using electric properties tomography. Magn Reson Med 2011;66:456–466.

[67] van Lier ALHMW, Raaijmakers A, Voigt T, Lagendijk JJW, Luijten PR, Katscher U, van den Berg CAT. Electrical properties tomography in the human brain at 1.5, 3, and 7T: A comparison study. Magn Reson Med 2014;71:354–363.

[68] Huang L, Schweser F, Herrmann KH, Kramer M, Deistung A, Reichenbach JR. A Monte Carlo method for overcoming the edge artifacts in MRI-based electrical conductivity mapping. In Proceedings of the 22nd Annual Meeting of ISMRM, Milan, Italy, 2014. p. 3190.

[69] Mandija S, Sbrizzi A, van Lier ALHMW, Luijten P, van den Berg CAT. Artifacts affecting derivative of B1+ maps for EPT reconstructions. In Proceedings of the 24th Annual Meeting of ISMRM, Singapore, 2016. p. 2989.

[70] Seo JK, Kim MO, Lee J, Choi N, Woo EJ, Kim HJ, Kwon OI, Kim DH. Error analysis of nonconstant admittivity for MR-based electric property imaging. IEEE Trans Med Imag 2012;31:430–437.

[71] Duan S, Xu C, Deng G, Wang J, Liu F, Xin SX. Quantitative analysis of the reconstruction errors of the currently popular algorithm of magnetic resonance electrical property tomography at the interfaces of adjacent tissues. NMR Biomed 2016;29:744–750.

[72] Lee SK, Bulumulla S, Hancu I. Theoretical Investigation of Random Noise-Limited Signal-to-Noise Ratio in MR-Based Electrical Properties Tomography. IEEE Trans Med Imag 2015;34:2220–2232.

[73] Michel E, Hernandez D, Cho MH, Lee SY. Denoising of B1+ field maps for noise-robust image reconstruction in electrical properties tomography. Med Phys 2014;41:1–9.

[74] Kim JH, Shin J, Lee HJ, Ryu KH, Kim DH. Adaptive weighted polynomial fitting in phase-based electrical property tomography. In Proceedings of the 25th Annual Meeting of ISMRM, Honolulu, HI, USA, 2017. p. 3643.

[75] Ider Y, Ariturk G, Yildiz G. Spatial and contrast resolution of phase based MREPT. In Proceedings of the 25th Annual Meeting of ISMRM, Honolulu, HI, USA, 2017. p. 3642.

[76] Ropella KM, Noll DC. Data-driven background phase correction and combination to improve the accuracy of MR-EPT with multi-channel receivers. In Proceedings of the 25th Annual Meeting of ISMRM, Honolulu, HI, USA, 2017. p. 3646.

[77] Mandija S, van Lier AL, Katscher U. A geometrical shift results in erroneous appearance of low frequency tissue eddy current induced phase maps. Magn Reson Med 2016;76:905–912.

[78] Hafalir FS, Oran OF, Gurler N, Ider YZ. Convection-reaction equation based magnetic resonance electrical properties tomography(cr-MREPT). IEEE Trans Med Imag 2014;33:777–793.

[79] Liu L, Zhang X, Schmitter S, de Moortele PFV, He B. Gradient-based electrical properties tomography (gEPT): A robust method for mapping electrical properties of biological tissues in vivo using magnetic resonance imaging. Magn Reson Med 2015;74:634–646.

[80] Gurler N, Ider YZ ;77:137–150.

[81] Shin J, Kim M, Kim J, Kim DH. Relaxation based conductivity weighted imaging(rCWI). In Proceedings of the 24th Annual Meeting of ISMRM, Singapore, 2016. p. 1110.

[82] Balidemaj E, van den Berg CA, Trinks J, van Lier AL, Nederveen AJ, Stalpers LJA, Crezee H, Remis RF. CSI-EPT: A contrast source inversion approach for improved MRI-based electric properties tomography. IEEE Trans Med Imag 2015;34:1788–1796.

[83] Ammari H, Kwon H, Lee Y, Kang K, Seo JK. Magnetic resonance-based reconstruction method of conductivity and permittivity distributions at the Larmor frequency. Inverse Problems 2015;31:105001.

[84] Borsic A, Perreard I, Mahara A, Halter RJ. An inverse problems approach to MR-EPT image reconstruction. IEEE Trans Med Imag 2016;35:244–256.

[85] Palamodov V. An analytic method for the inverse problem of MREPT. Inverse Problems 2016;32:1–5.

[86] Ropella KM, Noll DC. A regularized, model-based approach to phase-based conductivity mapping. Magn Reson Med 2017;78:2011–2021.

[87] Rahimov A, Litman A, Ferrand G. MRI-based electric properties tomography with a quasi-Newton approach. Inverse Problems 2017;33:105004.

[88] Serralles J, Georgakis I, Polimeridis A, Daniel L, White J, Sodickson D, Lattanzi R. Volumetric reconstruction of tissue electrical properties from b1+ and MR signals using Global Maxwell Tomography: Theory and simulation results. In Proceedings of the 25th Annual Meeting of ISMRM, Honolulu, HI, USA, 2017. p. 3647.

[89] Katscher U, Herrmann M, Findeklee C, Doneva M, Amthor T. Dictionary-based electric properties tomography. In Proceedings of the 25th Annual Meeting of ISMRM, Honolulu, HI, USA, 2017. p. 3641.

[90] Liu J, Zhang X, Wang Y, de Moortele PFV, He B. Local electrical properties tomography with global regularization by gradient. In Proceedings of the 23rd Annual Meeting of ISMRM, Toronto, ON, Canada, 2015. p. 3297.

[91] Sodickson DK, Alon L, Deniz CM, Brown R, Zhang B, Wiggins GC, Cho GY, Eliezer NB, Novikov DS, Lattanzi R, Duan Q, Sodickson LA, Zhu Y. Local

maxwell tomography using transmit-receive coil arrays for contact-free mapping of tissue electrical properties and determination of absolute RF phase. In Proceedings of the 20th Annual Meeting of ISMRM, Melbourne, VIC, Australia, 2012. p. 387.

[92] Sodickson DK, Alon L, Deniz CM, Ben-Eliezer N, Cloos M, Sodickson LA, Collins CM, Wiggins GC, Novikov DS. Generalized local maxwell tomography for mapping of electrical property gradients and tensors. In Proceedings of the 20th Annual Meeting of ISMRM, Melbourne, VIC, Australia, 2012. p. 2532.

[93] Serralles JE, Polimeridis A, Vaidya MV, Haemer G, White JK, Sodickson DK, Daniel L, Lattanzi R. Global maxwell tomography: a novel technique for electrical properties mapping without symmetry assumptions or edge artifacts. In Proceedings of the 24th Annual Meeting of ISMRM, Singapore, 2016. p. 2993.

[94] Charbonnier P, Blanc-Feraud L, Aubert G, Barlaud M. Two deterministic half-quadratic regularization algorithms for computed imaging. In Proceedings of IEEE International Conference on Image Processing, 1994, volume 2. pp. 168–171.

[95] Panin VY, Zeng GL, Gullberg GT. Total variation regulated EM algorithm. IEEE Trans Nucl Sci 1999;46:2202–2210.

[96] Fessler JA. Image Reconstruction Toolbox. Available: http://web.eecs.umich.edu/˜fessler/code/index.html.

[97] Kim DH, Choi N, Gho SM, Shin J, Liu C. Simultaneous imaging of in-vivo conductivity and susceptibility. Magn Reson Med 2014;71:1144–1150.

[98] Xu W, Cumming I. A region-growing algorithm for InSAR phase unwrapping. IEEE Trans Geosci Remote Sens 1999;37:124–134.

[99] Wellcome Trust Centre for Neuroimaging. Statistical Parametric Mapping. Available: http://www.fil.ion.ucl.ac.uk/spm/.

[100] Hasgall PA, Neufeld E, Gosselin MC, Klingenbock A, Kuster N. IT'IS database for thermal and electromagnetic parameters of biological tissues. Version 2.4 2013.

[101] Vegh V, O'Brien K, Barth M, Reutens DC. Selective Channel Combination of MRI Signal Phase. Magn Reson Med 2016;76:1469–1477.

[102] Roemer PB, Edelstein WA, Hayes CE, Souza SP, Mueller OM. The NMR Phased Array. Magn Reson Med 1990;16:192–225.

[103] Walsh DO, Gmitro AF, Marcellin MW. Adaptive Reconstruction of Phased Array MR Imagery. Magn Reson Med 2000;43:682–690.

[104] Zhang T, Pauly JM, Vasanawala SS, Lustig M. Coil Compression for Accelerated Imaging with Cartesian Sampling. Magn Reson Med 2013;69:571–582.

[105] Ropella KM, Noll DC. Coil compression for improved phase image signal-to-noise ratio in electrical property tomography. In Proceedings of the 24th Annual Meeting of ISMRM, Singapore, 2016. p. 1564.

[106] Lee J, Shin J, Kim DH. MR-Based conductivity imaging using multiple receiver coils. Magn Reson Med 2016;76:530–5392.

[107] Cao M, Stenger VA, Eddy W. Estimation of images and sensitivities for multi-coil MRI. In Proceedings of the 13th Annual Meeting of ISMRM, Miami, FL, USA, 2005. p. 2447.

[108] Hoyos-Idrobo A, Weiss P, Massire A, Amadon A, Boulant N. On variant strategies to solve the magnitude least squares optimization problem in parallel transmission pulse design and under strict SAR and power constraints. IEEE Trans Med Imag 2014;33:739–748.

[109] Setsompop K, Wald LL, Alagappan V, Gagoski BA, Adalsteinsson E. Magnitude least squares optimization for parallel radio frequency excitation design demonstrated at 7 Tesla with eight channels. Magn Reson Med 2008;59:908–915.

[110] Ghiglia DC, Pritt MD. Two-Dimensional Phase Unwrapping: Theory, Algorithms, and Software. New York: John Wiley & Sons; 1998. 512 p.

[111] Kim Y, Fessler JA, Noll DC. Smoothing effect of sensitivity map on fMRI data using a novel regularized self-calibrated estimation method. In Proceedings of the 16th Annual Meeting of ISMRM, Toronto, ON, Canada, 2008. p. 1267.

[112] Goerner FL, Duong T, Stafford RJ, Clarke GD. A comparison of five standard methods for evaluating image intensity uniformity in partially parallel imaging MRI. Med Phys 2013;40:082302.

[113] Tuch DS, Wedeen VJ, Dale AM, George JS, Belliveau JW. Conductivity tensor mapping of the human brain using diffusion tensor MRI. Proceedings of the National Academy of Sciences of the United States of America 2001;98:11697–11701.

[114] Katscher U, Voigt T, Findeklee C. Estimation of the Anisotropy of Electric Conductivity via B1 Mapping. In Proceedings of the 18th Annual Meeting of ISMRM, Stockholm, Sweden, 2010. p. 2866.

[115] Lee J, Song Y, Choi N, Cho S, Seo JK, Kim DH. Noninvasive Measurement of Conductivity Anisotropy at Larmor Frequency using MRI. Comput Math Methods Med 2013;2013:421619.

[116] Behrens TEJ, Woolrich MW, Jenkinson M, Johansen-Berg H, Nunes RG, Clare S, Matthews PM, Brady JM, Smith S. Characterization and propagation of uncertainty in diffusion-weighted MR imaging. Magn Res Med 2003;50:1077–1088.

[117] Jenkinson M, Beckmann CF, Behrens TE, Woolrich MW, Smith SM. FSL. NeuroImage 2012;62:782–90.

[118] Koay CG, Carew JD, Alexander AL, Basser PJ, Meyerand ME. Investigation of anomolous estimates of tensor-derived quantities in diffusion tensor imaging. Magn Reson Med 2006;55:930–936.